Nanoscale

ROYAL SOCIETY OF CHEMISTRY

REVIEW

View Article Online
View Journal | View Issue

Cite this: *Nanoscale*, 2020, **12**, 477

Progress in $BiFeO_3$-based heterostructures: materials, properties and applications

Li Yin and Wenbo Mi *

$BiFeO_3$-based heterostructures have attracted much attention for potential applications due to their room-temperature multiferroic properties, proper band gaps and ultrahigh ferroelectric polarization of $BiFeO_3$, such as data storage, optical utilization in visible light regions and synapse-like function. Here, this work aims to offer a systematic review on the progress of $BiFeO_3$-based heterostructures. In the first part, the optical, electric, magnetic, and valley properties and their interactions in $BiFeO_3$-based heterostructures are briefly reviewed. In the second part, the morphologies of $BiFeO_3$ and medium materials in the heterostructures are discussed. Particularly, in the third part, the physical properties and underlying mechanism in $BiFeO_3$-based heterostructures are discussed thoroughly, such as the photovoltaic effect, electric field control of magnetism, resistance switching, and two-dimensional electron gas and valley characteristics. The fourth part illustrates the applications of $BiFeO_3$-based heterostructures based on the materials and physical properties discussed in the second and third parts. This review also includes a future prospect, which can provide guidance for exploring novel physical properties and designing multifunctional devices.

Received 14th October 2019,
Accepted 11th December 2019

DOI: 10.1039/c9nr08800h

rsc.li/nanoscale

I. Introduction

As a room-temperature single phase multiferroic material, $BiFeO_3$ (BFO)[1–4] has attracted much attention because of its high ferroelectric Curie temperature of 1103 K and antiferromagnetic Neel temperature of 643 K.[5–7] The ferroelectric polarization in BFO is mainly induced by the ordered $6s^2$ lone pair

Tianjin Key Laboratory of Low Dimensional Materials Physics and Preparation Technology, School of Science, Tianjin University, Tianjin 300354, China.
E-mail: miwenbo@tju.edu.cn

Li Yin

Dr Li Yin received her B.S. degree from the School of Physics and Electronic Science at Shanxi Datong University, China, in 2014. She received her M.S. and Ph.D. degrees from the Department of Applied Physics from Tianjin University in 2019, under the supervision of Prof. Wenbo Mi. Now she is working as a postdoctoral research associate in Oak Ridge National Laboratory. Her research interests focus on the multiferroic properties and electronic structures of oxide heterostructures.

Wenbo Mi

Prof. Wenbo Mi received his B.S., M.S. and Ph.D. degrees from the Department of Physics from Tianjin University in 2001, 2004 and 2006, respectively. Then he became an assistant professor at the Department of Physics, Tianjin University and was promoted as a full professor in 2013. He was a visiting scholar in 2008 at the Hong Kong University of Science and Technology, and then he became a Postdoc Fellow in the King Abdullah University of Science and Technology in 2010. His research interests mainly focus on the theoretical design, fabrication and physical properties of low-dimensional spintronic and multiferroic materials.

electrons of Bi,[8,9] and its antiferromagnetism comes from the 3d electrons of Fe. Based on X-ray and neutron diffraction analyses, the ferroelectric phase of BFO can be treated as a highly distorted perovskite with the rhombohedral symmetry and space group $R3c$,[4,10,11] and shows [111]-oriented spontaneous polarization. The experimental ferroelectric polarization in BFO is different by an order of magnitude, which may be ascribed to the different switching pathways.[1] BFO has a G-type antiferromagnetic order, which comes from the super-exchange interaction between the neighboring half–full d-shell of the Fe^{3+} cation and O^{2-} anion.[4] Moreover, based on the spin current model, the magnetic phase diagram as a function of the first- and second-nearest neighbor interactions has been predicted in bulk BFO.[12]

Early research studies on BFO focused on its magnetoelectric coupling in a bulk $R3c$ perovskite structure[13] with a cycloidal G-type antiferromagnetic order at a period of $\lambda_{\langle 110\rangle}$ = 64 nm,[12,14–16] where the spin orientation can be changed by the magnetic field.[17–19] In 2003, Wang *et al.*[10] fabricated BFO films, which expands the applications of BFO in heterostructures.[20] The BFO film shows rhombohedral-like (R-), tetragonal-like (T-) and R–T mixed phases.[11,21–24] R-BFO has a small monoclinic distortion in $R3c$ and T-BFO has a cubic structure with a symmetry of $P4mm$.[24] The ultrahigh spontaneous ferroelectric polarization is 90 μC cm^{-2} in R-BFO films[25–27] and 150 μC cm^{-2} in T-BFO films.[28,29] In particular, the BFO film shows a broken spin cycloid with a weak ferromagnetic moment[30] and multidomain ferroelectric characteristics with different domain wall densities and flavors (*i.e.*, 71°, 109°, and 180°), which is different from its bulk. The heterostructure is an effective way to utilize the ferroelectric polarization and multiferroic characteristics of BFO. The interplay among charge, spin, valley, lattice and orbital degrees of freedom (DOF)[31,32] provides a fertile ground for discovering the emergent phenomena and physical properties in BFO-based heterostructures.

So far, many important characteristics (Fig. 1) have been found in BFO-based heterostructures including the optical, electrical, magnetic, and valley properties and the interactions among them. On the one hand, after the discovery of the photovoltaic effect in the BFO bulk,[33,34] the photovoltaic BFO-based heterostructures have been studied extensively. BFO films with various morphologies have been fabricated to utilize the light energy. BFO nanoparticles were used to improve the photovoltaic properties of other semiconductors by forming heterostructures[35] and heterojunctions.[36] In ferroelectric tunnel junctions (FTJs) with a doped-BFO thin layer,[37] the electroresistance can be tailored by light illumination due to the hysteretic photovoltaic effect. Polycrystalline BFO was utilized in photoelectrochemical water splitting by bringing it in contact with hydrophilic materials.[38,39] On the other hand, the electric field control of magnetism in BFO/ferromagnet heterostructures[4,40–42] has stimulated many novel properties[43–47] by the magnetoelectric coupling.[48] Both the magnetization reversal[49] and magnetic anisotropy[50,51] are tunable because of the ferroelectric/antiferromagnetic coupling in BFO and antiferromagnetic/ferromagnetic interfacial coupling.[52] Meanwhile, the large resistance switching (RS)[37,53,54] and memristive behavior[55] also have been found in BFO-based FTJs owing to their strong ferroelectric polarization in BFO and conductive filaments.[54,56] Four resistance states have been demonstrated in BFO-based multiferroic tunnel junctions (MFTJs),[57] where the ferromagnetic electrodes are used in FTJs or the ferroelectric barriers are used in magnetic tunnel junctions (MTJs). Emergent characteristics also have been observed in BFO-based heterostructures, such as the two-dimensional electron gas (2DEG) in BFO/insulator heterointerfaces[58,59] and the valley characteristics in the (111)-oriented R-BFO superlattices. In BFO/$BiIrO_3$ superlattices,[32] the ferroelectric polarization in the ultrathin BFO layer can tailor the valley height of $BiIrO_3$, where the spin polarization in valley states can be affected by the spin orientation of BFO. In particular, the ferroelectric domain and phase transition in BFO provide a fertile ground for discovering the novel properties in heterostructures, such as the domain-dependent photovoltaic effect[60] and phase-transition induced RS in junctions.[61]

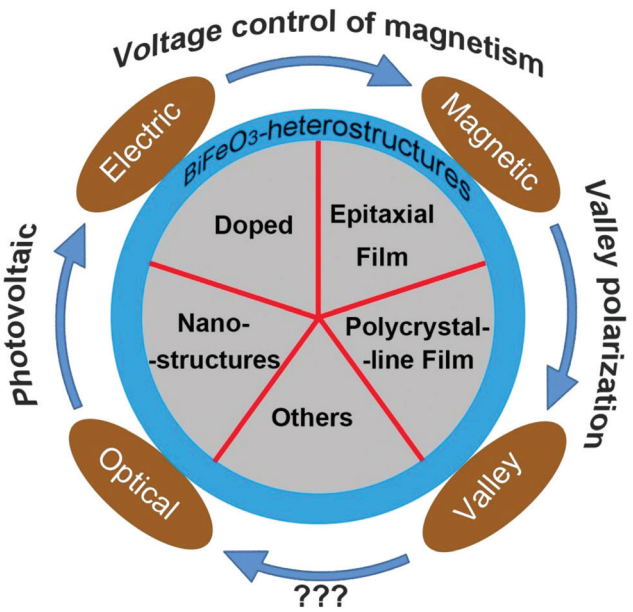

Fig. 1 The schematic diagram of interacting physical properties in the BFO-based heterostructures.

Regarding applications, BFO-based heterostructures have been used in spintronic and energy-efficient devices, such as nonvolatile ferroelectric random access memory, spin valves and spin-transfer-torque magnetic random access memory. In these devices, BFO shows different formations including thin films, nanoparticles and doped systems. In particular, the interaction among the optical, ferroelectric and magnetic characteristics of BFO is very important for the functionality of the devices. Meanwhile, owing to the interaction of properties in BFO, the induced novel properties in BFO-based heterostructures are commonly tailored by electrical, magnetic and optical methods, which is beneficial for developing multifunc-

tional and complementary devices. This article aims to offer a systematic review on the progress in BFO-based heterostructures. After the brief introduction in section I, the materials, properties and applications of BFO-based heterostructures are discussed in the next three sections, where the contributions of the domain and phase transition in BFO are analyzed. Finally, a prospect is also included in this review, which will provide guidance for exploring novel physical properties and designing multifunctional devices.

II. Materials in $BiFeO_3$-based heterostructures

In order to clearly illustrate the materials of BFO-based heterostructures, the morphologies of BFO and materials in contact with BFO in heterostructures are discussed in subsections II.A and II.B, respectively. Here, in subsection II.A, the morphology of BFO is classified into the epitaxial film, polycrystalline film, nanostructures and doped systems, where the advantages and drawbacks among them are compared. In subsection II.B, the materials in contact with BFO in the heterostructures are divided into semiconductors, metals and insulators.

A. Morphology of $BiFeO_3$ in heterostructures

1. Epitaxial film. In the heterostructures, the epitaxial BFO films have the R-, T- or R–T-mixed phases, which show different ferroelectric polarizations and related properties, such as the photovoltaic characteristics and electroresistance in FTJs. Fig. 2a shows the perovskite-type lattice structure of R-BFO, where the ferroelectric polarization shows 180°, 109° or 71° polarization switching by applying an electric field.[62] The epitaxial R-BFO and T-BFO films are commonly fabricated on $SrTiO_3$ and $LaAlO_3$ substrates,[10,63,64] which can be ascribed to the strain effect from the substrate due to the lattice mismatch. Particularly, the termination has a great influence on the electrical and magnetic properties of heterostructures.[65,66] So far, since the fabrication technology has been greatly improved, the epitaxial BFO heterostructures with an atomic scale surface morphology have been fabricated, where the interfacial terminations of BFO and the adjacent material are controllable.[67,68] For example, Yu *et al.* have fabricated $La_{0.7}Sr_{0.3}MnO_3$/BFO heterostructures with $La_{0.7}Sr_{0.3}O$–MnO_2–BiO–FeO_2 and MnO_2–$La_{0.7}Sr_{0.3}O$–FeO_2–BiO interfaces by pulsed laser deposition.[67] In order to obtain an $La_{0.7}Sr_{0.3}O$-terminated $La_{0.7}Sr_{0.3}MnO_3$ film, Yu *et al.*[67] modified the $SrTiO_3$ substrate from TiO_2 to SrO termination, which can be realized by growing a very thin layer (2.5 unit cells) of $SrRuO_3$ on $SrTiO_3$ or monolayer SrO on the TiO_2-terminated $SrTiO_3$ substrate. Kim *et al.* also have fabricated the $La_{0.7}Sr_{0.3}MnO_3$/BFO heterostructures with different terminations by a similar method.[68] Besides, the $(BFO)_2/(SrTiO_3)_4$ superlattices also have been prepared by pulsed laser deposition, where the thickness of BFO in heterostructures can be as small as two unit cells with ferroelectric domains.[69] Moreover, except pulsed laser deposition, other experimental methods have also been used to fabricate the epitaxial BFO-based heterostructures. Using the van der Waals epitaxy method, Amrillah *et al.* have successfully grown BFO-based epitaxial heterostructures on a flexible muscovite substrate,[70] which can avoid the substrate clamping effect to obtain a superior magnetoelectric coupling. Meanwhile, doped BFO superlattices also have been prepared by a chemical solution route.[71] In addition, Akbashev *et al.* have successfully prepared a single-crystalline epitaxial BFO (001) film on an $SrTiO_3$(001) substrate by an atomic layer deposition method,[72] which is favored by a low-vacuum pressure

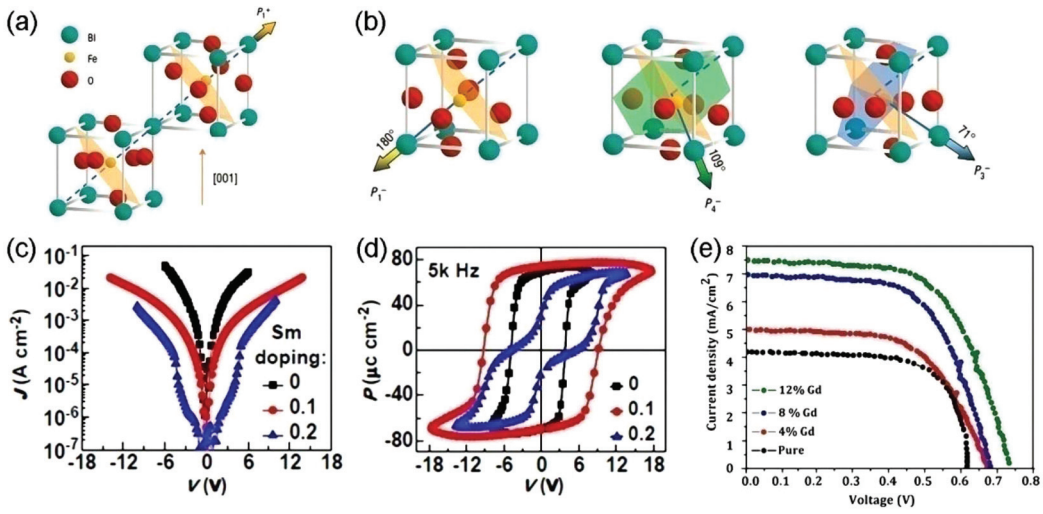

Fig. 2 Schematic diagram of the lattice structure, ferroelectric polarization (bold arrows) and antiferromagnetic order (shaded planes) of the (001)-oriented BFO (a) before and (b) after electric poling. Adapted with permission from ref. 62. Copyright 2006, Nature Publishing Group. (c) The leakage current and (d) the ferroelectric hysteresis of 200 nm $Sm_xBi_{1-x}FeO_3$ (x = 0, 0.1, 0.2) films. Adapted with permission from ref. 37. Copyright 2016, Nature Publishing Group. (e) Photo-current density as a function of applied voltages in the Gd-doped BFO nanoparticles. Adapted with permission from ref. 124. Copyright 2013, Elsevier.

process and subsequent annealing for a few minutes. It is worth noting that the BFO and other complex oxide films on perovskite substrates can be fabricated by the inexpensive and facile atomic layer deposition. These advanced fabrication methods provide the foundation for investigating the epitaxial BFO-based heterostructures with different interfaces, terminations, and thicknesses.

The most typical feature of epitaxial BFO films is the ultrahigh spontaneous ferroelectric polarization, which can reach 90 μC cm^{-2} in R-BFO[25–27] and a larger value of 150 μC cm^{-2} in T-BFO.[28,29] However, it should be noted that the tunnel electroresistance (TER) in BFO-based FTJs is not only determined by the ferroelectric polarization, but also affected by the electrodes and interfaces. In the rhombohedral BFO-based FTJs with a semiconducting Nb-doped $SrTiO_3$ electrode, Hu *et al.*[37] observed a colossal TER of 10^5, which is 10 times larger than that in the T-BFO-based FTJs.[55] Meanwhile, the writing current density in R-BFO-based FTJs [20] can be as small as 2×10^4 A cm^{-2}, which is two to three orders smaller than that in the magnetic random access memories (MRAMs),[73] spin–transfer–torque–MRAMs[74] or spin–orbit–torque–MRAMs.[75] Moreover, besides the ultrahigh ferroelectric polarization, the varied ferroelectric domain wall density and flavor can modulate the interfacial exchange couplings in the BFO-based heterostructures.[4,76] In the tetragonal BFO-based FTJs,[55] the multiple resistive states with memristive behaviors appear along with the engineered domain states. The ferroelectric domain size shows a square root dependence on the film thickness,[76] which results in the nanoscale poly-domain states in the ultrathin ferroelectric films. More domain-related effects on the photovoltaic effects and RS in the BFO-based heterostructures will be discussed specifically in subsections III.A.1 and III.C.2, respectively.

The typical application of the epitaxial BFO-based heterostructures is FTJs, which can be further applied in integrated functionalities. On the one hand, the ferromagnetic electrodes with a high spin polarization are applied in BFO-based FTJs to form MFTJs with four resistance states.[57] The reversible ferroelectric polarization in BFO and the tunable parallel–antiparallel magnetic configurations in two ferromagnetic electrodes result in four resistance states in the BFO-based MFTJs. On the other hand, owing to the photovoltaic effects in the BFO film, light illumination becomes a notably effective method to modulate the TER in epitaxial BFO-based FTJs,[37] where the electric-field control of tunnel magnetoresistance (TMR) is also effective. Kim *et al.* have utilized epitaxial BFO films as a multiferroic nanocapacitor, which can induce a nonlinear electromechanical response.[77] The electrical and optical modulations can provide a fertile ground for inducing multifunctional characteristics in BFO-based FTJs and MFTJs.

Notably, the charge screening at the heterointerfaces is always incomplete, which results in an extra depolarization field to reduce the polarization in ferroelectric materials.[21,78–81] In order to improve the polarization at interfaces, Liu *et al.* have designed $PbTiO_3$/BFO heterointerfaces with a discontinued chemical valence and ferroelectric polarization.[82] A locally enhanced ferroelectric polarization occurs in the head-to-tail $PbTiO_3$/BFO polarized interface region,[82] which can be ascribed to the negative charge accumulation in BFO and the positively charged resultant oxygen vacancies in $PbTiO_3$. Special hierarchical ferroelectric domains also have been found in $(1 - x)$BFO–$x$$PbTiO_3$ ferroelectric solid solution.[83] Obviously, since the ferroelectric polarization can modulate the interfacial coupling, the interfacial coupling can conversely affect the ferroelectric polarization, which should be intensively studied in the future. Besides, in the epitaxial BFO/$LaFeO_3$ superlattices, the changed periodicity can modulate the interlayer strain, which will induce a phase transition in BFO.[84] In lead-free BFO-based ceramics, the composition change can also induce the strain to trigger the phase transition in BFO.[85] In the BFO-based heterostructures, the phase transition can affect the ferroelectric polarization and resistance,[61] which will be discussed in subsection III.C.2.

2. **Polycrystalline film.** In the BFO-based heterostructures, the polycrystalline BFO films can come in contact with the other material without the limitation of a lattice match. Polycrystalline BFO films can be fabricated by various methods, such as radio-frequency sputtering,[86] pulse laser deposition[87] and the sol-gel method.[39] In particular, two-dimensional graphene can serve as a transparent electrode in photovoltaic devices with polycrystalline BFO films, where the chemically treated graphene can enhance the photovoltaic effects in BFO.[88] The switchable photovoltaic effect also occurs in the graphene/BFO heterostructures.[87] Besides, the polycrystalline BFO films can come in contact with the hydrophilic RGO,[39,89] where the improved photocurrent and photo-to-current efficiency can be used in photoelectrochemical water splitting. Different from the epitaxial BFO films, the polycrystalline BFO films can stimulate the novel electrical and optical properties by making contact with the two-dimensional or hydrophilic materials to form the heterostructures, which can expand the practical applications of BFO-based heterostructures.

3. **Nanoscale particles and grains.** Distinct from the epitaxial or polycrystalline films, the nanoscale BFO particles and grains have a special morphology and quantum size effects,[90,91] which can induce the novel physical and chemical properties in BFO and its related heterostructures, such as the size-induced enhancement of antiferromagnetic transition temperature,[92] a red-shift band gap of BFO[93] and a size-dependent magnetic exchange bias.[94] In particular, the BFO nanocomposites are used to enhance or improve the photovoltaic characteristics of other semiconductors by building the heterostructures.[35] In the BFO/TiO_2 nanotube arrays,[35] the photoconversion efficiency of TiO_2 nanotubes is largely improved by making contact with BFO nanoparticles which were deposited into TiO_2 nanotubes by an ultrasonic-immersion method. Meanwhile, Sarkar *et al.* fabricated the multifunctional BFO/TiO_2 nanoscale heterostructures by the wet chemical and electrochemical routes, showing the ferroelectric diode characteristic and photovoltaic effect.[91] The nonvolatile ON–OFF electronic conductions can also be switched by the external bias in

such BFO/TiO_2 nanoheterostructures,[91] which can be applied in logic circuits and nonvolatile resistance random access memory.

The BFO nanoparticles can also assemble together to form a thin film, which can interact with another film to build the heterostructures. Chatterjee *et al.* have fabricated p–i–n type BFO-based heterojunctions, where the insulating layer of BFO nanoparticles is sandwiched by the p-type NiO(MoO_3) and n-type ZnO semiconducting layers.[36] The photovoltaic properties of the p–i–n type BFO-based junctions are improved by comparing to the p–i or i–n structures because of the enlarged depletion regions.[36]

Notably, various self-assembled BFO-based nanocomposites have attracted more and more attention,[95–102] where novel physical properties are observed. In Fig. 3, the $CoFe_2O_4$/BFO nanocomposites can be fabricated by coating, patterning, ion etching and epitaxial growth. Triblock terpolymers[95] and nucleation induction[103] have also been successfully utilized to fabricate self-assembled $CoFe_2O_4$/BFO nanocomposites. The $CoFe_2O_4$/BFO heterostructures can also be synthesized into well-ordered nanodots, where the piezoelectric response and ferromagnetic properties can lead to a large magnetoelectric effect.[104] The magnetic properties of $CoFe_2O_4$/BFO nanocomposites can be tailored by the composition in the $Co_xNi_{1-x}Fe_2O_4$/BFO ($0 \le x \le 1$) heterostructures.[105] In particular, novel physical properties have been demonstrated in the nanoscale $CoFe_2O_4$/BFO systems. Budi *et al.* have reported an exchange bias in BFO:$CoFe_2O_4$ nanofibers.[106] The local conduction appears at the BFO–$CoFe_2O_4$ tubular oxide interface.[107] The epitaxial BFO–$CoFe_2O_4$ nanocomposites have also been successfully fabricated on Si substrates.[108] These results provide opportunities for designing functional BFO-based nanoscale devices.

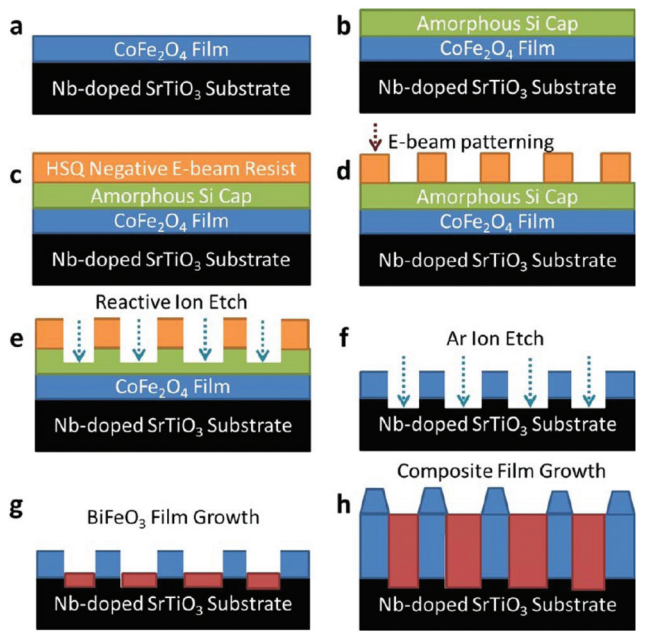

Fig. 3 Fabrication process of $CoFe_2O_4$/BFO nanocomposites. (a) Depositing a $CoFe_2O_4$ film on an Nb-doped $SrTiO_3$ substrate by pulsed electron deposition, and then (b) depositing an amorphous Si capping layer on a $CoFe_2O_4$ film by radio-frequency sputtering. (c) Performing spin coating on the fabricated sample with the hydrosilsesquioxane negative-tone e-beam resist, and then (d) patterning the coated structure into pillars by e-beam lithography. (e) Performing the reactive ion etching on an Si cap and subsequently Ar ion etching on the $CoFe_2O_4$ film. (g) Depositing a BFO film with a thickness of 1 nm, and then (h) preparing the $CoFe_2O_4$ and BFO films simultaneously by pulsed electron deposition. Adapted with permission from ref. 96. Copyright 2012, American Chemical Society.

Moreover, the BFO nanoplates can be stacked upon monolayer graphene[109] using the dry transfer method and a micromanipulator, which provides opportunities to compose BFO with the two-dimensional materials. BFO nanowires can form nanocomposites with RGO by the hydrothermal methods,[110] and are a good electrode candidate in supercapacitors due to their superior capacitance, high charge density and high cycling stability. These unique properties of BFO nanocomposites fabricated by different preparation methods offer a fertile ground for stimulating novel properties and applications in multiferroic BFO-based heterostructures.

4. Doped variants of above forms. In FTJs with epitaxial BFO films, the leakage current suppresses the switching effect of the ferroelectric polarization and leads to a small TER, which is disadvantageous for the performances of devices. However, in oxide multiferroics, the doping cation is an effective tool to modulate the electrical properties.[111] Abundant results indicate that the leakage current can effectively decrease by doping in BFO with A-site rare earth elements (such as La, Ce and Pr)[112–114] and B-site transition metal elements (such as Ti, Ni and Mn).[112,115,116] Hu *et al.* fabricated epitaxial $Sm_{0.1}Bi_{0.9}FeO_3$ films by pulsed-laser deposition.[37] As seen in Fig. 2c and d, the leakage current of the $Sm_{0.1}Bi_{0.9}FeO_3$ (200 nm) film is more than 10 times smaller than that of pure BFO, where a large remnant polarization of ~70 μC cm^{-2} is preserved by doping.[37] Besides, the interface of BFO-based heterostructures is also an effective method to decrease the leakage current.[117] The spatial distribution of the internal ferroelectric order in leaky BFO is vectorially coupled with light, where the generated spatially resolved photocurrent and photovoltage can be used to detect the leakage properties of BFO.[118] Besides, based on the oxidation state and coordination number, the site of the dopant in BFO can be estimated from the tabulated ionic radii, which are predicted by the systematic first-principles calculations.[119]

In particular, in ferroelectric materials, the open-circuit voltage (V_{OC}) depends on a large band gap, while the short-circuit photocurrent density (J_{SC}) is related to a small band gap for effectively absorbing the solar energy.[120–122] Considering that doping is an effective approach for tailoring the band gap,[123] appropriate doping in BFO becomes an appropriate way to balance V_{OC} and J_{SC}.[121] Gupta *et al.*[112] have demonstrated that the intensity of laser light and the thickness of (Ce, Mn)-codoped BFO films can further increase the J_{SC} to 0.245 mA cm^{-2}. Polycrystalline $BiFe_{0.95}Si_{0.05}O_3$ with a red shift of the band gap has been fabricated successfully, showing

improved ferroelectric switching properties.[122] Lotey *et al.* also observed a blue shift of the band gap in Gd-doped BFO nanoparticles.[124] Meanwhile, as shown in Fig. 2e, a higher J_{SC} and resultant energy conversion efficiency have been achieved in the Gd-12%-doped case.[124] So, doping in epitaxial films, polycrystalline films and nanoparticles of BFO is crucial for engineering the band gap, electrical properties and ferroelectric–photovoltaic characteristics, and provides a possible route to improve the performances in related ferroelectric and optical devices.

Besides, during the growth of BFO films, either the deposition parameters or targets can result in stoichiometry fluctuations and resultant defects in BFO.[125,126] The impurity defects in BFO will pin the domain wall and hinder the backwitching of ferroelectric polarization,[126] which will lead to the so-called retention failure in BFO-based ferroelectric storage systems. However, the storage-undesirable defects can modulate the polarization configurations and mixed-phase structures in BFO.[126]

Moreover, the molar ratio in BFO can be intentionally modulated using materials with similar lattice structures. By utilizing similar lattice structures of T-BFO and $BiCoO_3$, Gao *et al.* have prepared $BiFe_{0.5}Co_{0.5}O_3$ targets by a sol-gel method, which is further used to fabricate epitaxial $BiFe_{0.5}Co_{0.5}O_3$ films on $LaAlO_3$ substrates by pulsed laser deposition.[127] Different from the antiferromagnetic properties of multiferroic BFO or $BiCoO_3$, the $BiFe_{0.5}Co_{0.5}O_3$ film shows a ferromagnetic characteristic because of the spin-state transition of Co^{3+} ions.[127] Moreover, when a voltage is applied, the *c* axis of multiferroic $BiFe_{0.5}Co_{0.5}O_3$ can be compressed by ~20%,[127] and such a large piezoelectric response is rare in multiferroics.

B. Medium in contact with $BiFeO_3$ in heterostructures

1. Semiconductors. Semiconductors are commonly used as buffer layers to modulate the built-in electric field in the BFO/semiconductor interfaces, which can affect the separation of photo-generated carriers and the photovoltaic effect. n-Type ZnO,[86] n-type TiO_2,[128] p-type NiO[36] and p-type MoO_3 semiconductors[36] have been frequently used in photovoltaic BFO-based heterostructures. Besides, in order to improve the interactions between BFO and semiconductors, the mesoporous structure has been utilized in TiO_2/BFO/NiO heterostructures.[128] The morphology can evidently improve the photovoltaic characteristics in the TiO_2/BFO/NiO heterostructures.[128]

Typically, in BFO-based FTJs, semiconductors[37] can also serve as electrodes and light-absorbing layers. In Nb:$SrTiO_3$/$Sm_{0.1}Bi_{0.9}FeO_3$/Pt FTJs,[37] the Nb:$SrTiO_3$ electrode can induce two conduction modes of direct tunneling and Schottky thermionic emission, which is absent in BFO-FTJs with metal electrodes. Meanwhile, the semiconductors can generate abundant electron–hole pairs by light illumination, which can complement the inefficient generation of electron–hole pairs in ferroelectric materials.[86]

2. Nonmagnetic metals. In BFO-based heterostructures, nonmagnetic metals are commonly used as electrodes in photovoltaic devices and FTJs, such as Au and Pt.[55,129,130] The metal electrodes in the BFO-based FTJs can be engineered with other metal atoms.[131] You *et al.* have implanted Ti in a Pt bottom electrode in Au/BFO/Pt junctions. The implanted Ti atoms can diffuse into the BFO layer and modulate the interfacial oxide vacancies, which stabilize the RS in the Au/BFO/Ti junctions.[131] Meanwhile, nonmagnetic metals with different work functions can also serve as a buffer layer to modulate the photovoltaic characteristics in BFO-based heterostructures. For example, in Au/Ti/T-BFO/$La_{0.67}Sr_{0.33}MnO_3$(LSMO) and Au/Cr/T-BFO/LSMO,[132] different relative barrier heights appear between the Ti/Cr buffer layer and LSMO electrode, which results in the different separation of the photo-generated carriers and photovoltaic characteristics. Moreover, nonmagnetic transparent electrodes have also been utilized to investigate the optical properties in BFO-based heterostructures, such as indium-tin-oxide (ITO) and two-dimensional graphene.[122] Besides, an oxide metallic $LaNiO_3$ with paramagnetic properties can also serve as an electrode, which has good conductivity and a perovskite structure.[61,133] Hence, $LaNiO_3$ is commonly used as an electrode or buffer layer in heterostructures with perovskite BFO.

3. Ferromagnetic metals. Ferromagnetic materials, such as $Co_{0.9}Fe_{0.1}$,[49] Co,[51,134] $La_{1-x}Sr_xMnO_3$,[50,57,135–137] $LaMn_{0.5}Co_{0.5}O_3$[138] and Fe_4N,[45–47] are widely used for the electric field control of the magnetization reversal and magnetic anisotropy in BFO-based heterostructures. In BFO/ferromagnet heterostructures, the mechanism of the electric-field control of magnetism can be ascribed to magnetoelectric coupling.[43,44,139] The ferromagnetic layer can be pinned by antiferromagnetic BFO due to the interfacial exchange coupling.[140–144] Highly spin-polarized LSMO[136,137] and Fe_4N[145–147] are typical room-temperature ferromagnetic materials, which can be used to explore the spin-polarized transport properties in BFO-based MTJs and MFTJs. Moreover, hard magnetic $CoFe_2O_4$[148–151] shows strain-sensitive magnetic anisotropy. In the BFO–$CoFe_2O_4$ composites, the electric-field modulated magnetic anisotropy can be controlled by magnetoelectric coupling[150] and the strain in the piezoelectric substrate. The ferromagnetic shape memory alloy (FSMA) $Ni_{50.3}Mn_{36.9}Sb_{12.8}$[152] has a controlled magnetoelectric effect owing to the martensitic transformation,[153] which has also attracted much attention in electric-field controlled magnetism. Herewith, in BFO/ferromagnetic metal heterostructures, the ferroelectric polarization of BFO can modulate the interfacial oxygen vacancies,[154,155] which can improve the thermal stability of the heterostructures. In BFO/CoFeB heterostructures, the polarization-modulated thermal stability can be improved by ~100 °C,[154] which can be used by other BFO/ferromagnetic metal heterostructures.

4. Nonmagnetic and antiferromagnetic insulators. In BFO-based heterostructures, nonmagnetic insulators are commonly used as substrates to grow epitaxial R-BFO and T-BFO films,[10,64] such as perovskite-type $SrTiO_3$, $LaAlO_3$ and $YAlO_3$.[55] In particular, $SrTiO_3$[58,156] and antiferromagnetic Mott insulator $LaTiO_3$[59] can induce the 2DEG at the $SrTiO_3$/BFO and $LaTiO_3$/BFO interfaces due to the electronic confinement in

the nanoscale dimensions.[157] The appearance of the 2DEG in the BFO/insulator interfaces offers the opportunity of developing BFO-based nanoelectronic devices,[158] such as high mobility field-effect transistors.

In particular, non-magnetic ferroelectric materials also can modulate the electrical and magnetic properties of the BFO layer in the heterostructures. BFO/$BaTiO_3$ heterostructures show stronger ferroelectric properties than bare BFO.[159,160] The BFO/$BaTiO_3$ multilayers have shown a high energy storage efficiency of 82.3%[161] and a large magnetoelectric coupling with a magnetoelectric coefficient of 60.2 V (cm Oe)$^{-1}$.[162] The magnetic characteristics of BFO can be tailored by the composition of BFO/ferroelectric solid solution nanostructures, such as BFO_x–$(BaTiO_3)_{1-x}$ nanocubes[163] and BFO_{1-x}–$(PbTiO_3)_{1-x}$ ceramics.[164,165]

III. Properties and underlying mechanisms in $BiFeO_3$-based heterostructures

BFO exhibits ferroelectric polarization, antiferromagnetic order and an R–T phase transition. The ferroelectric characteristics stimulate a photovoltaic effect in BFO-based heterostructures, which will be discussed in subsection III.A. In particular, the ferroelectric characteristics of BFO interact with the antiferromagnetic order, domain structure and lattice structure. These various orders and couplings in BFO provide abundant factors to achieve efficient electric-field control of the magnetism and RS in the BFO-based heterostructures, which are discussed in subsections III.B and III.C, respectively. Emergent characteristics in BFO-based heterostructures are discussed in subsection III.D, such as the 2DEG and valley characteristics. These novel physical characteristics provide the foundation for developing optical, spintronic and electronic integrated multifunctional BFO-based devices.

A. Photovoltaic effect

In past decades, the photovoltaic effect has been a promising method to utilize the abundant and renewable solar energy.[166–170] Generally, the photovoltaic effect comes from the two basic processes of exciting the electron–hole (e–h) pairs and separating the e–h pairs.[34,171] In 2009, Choi *et al.* demonstrated the diode and photovoltaic effects in single-ferroelectric-domain bulk BFO,[34] where light-induced e–h pairs are separated by the depolarized field of ferroelectric BFO. Then, the diode forward direction in BFO can be reproducibly switched by the applied electric field due to the ferroelectric polarization of BFO.[34] In particular, the small optical gap (2.2–2.8 eV) of BFO[172,173] makes its photovoltaic effect lie in the visible light region,[34,174,175] which is beneficial for the practical applications of photovoltaic devices. After discovering the visible-light photovoltaic effects and ferroelectric-switchable characteristics of BFO, the optical modulation of the magnetoelectric properties was investigated in BFO-based heterostructures and ferroelectric memories.[37,176]

In photovoltaic metal/BFO/metal structures, a large V_{OC} is observed due to the depolarized field of BFO.[177–179] However, the inefficient excitation of e–h pairs in ferroelectric materials with a large band gap can lead to a small J_{SC} in the metal/BFO/metal structures.[86,169,180] In order to generate more e–h pairs, semiconductors are introduced as a buffer layer,[86] where the structure transforms into the metal/semiconductor/BFO/metal. Meanwhile, an extra built-in barrier is engineered by choosing the appropriate semiconductor[86] and metal[132] buffer layers to separate the e–h pairs. Both the barrier height and width can be tailored at the semiconductor/BFO interfaces,[37] which lays the foundation for complimentary bias- and light-controlled electrical properties in BFO-based heterostructures. Special electrodes have been used to improve the J_{SC}, V_{OC} and energy-conversion efficiency in BFO-based heterostructures, such as semiconducting Nb:$SrTiO_3$,[37] transparent graphene,[87,122] hydrophilic RGO[39] and TiO_2.[35,91,128] Obviously, appropriate metal/BFO/metal structures are very crucial for improving the photovoltaic characteristics, and can be applied in nonvolatile ferroelectric memories, photocatalysis and photoelectrochemical water splitting in BFO-based materials. Next, the physical mechanisms of photovoltaic effects in modified metal/BFO/metal heterostructures will be discussed in detail, where the ferroelectric domain effects on the photovoltaic characteristics will also be reviewed.

1. Ferroelectric modulation in metal/$BiFeO_3$/metal. The photovoltaic characteristics of the metal/BFO/metal structures are commonly studied, where the ferroelectric polarization direction of BFO layers can tailor the photovoltaic effects. Naturally, it is an approach to manipulate the photovoltaic effects by engineering the ferroelectric BFO layers. Sharma *et al.* have used a BFO/$BaTiO_3$ multilayer as a ferroelectric layer to enhance the ferroelectric properties of the interlayer, as shown in Fig. 4a and b.[159,160] Moreover, under the illumination of violet laser light (λ = 405 nm) with an intensity of 160 mW cm^{-2}, the multilayered BFO/$BaTiO_3$ structure shows a better photovoltaic response than a BFO single layer, which can enhance the V_{OC} from 0.33 to 1.25 V, as shown in Fig. 4c. Since the band gap of $BaTiO_3$ is 3.27 eV, the photovoltaic effect in BFO/$BaTiO_3$ based structures at a wavelength of 405 nm is not contributed by $BaTiO_3$. In the metal/ferroelectric/metal structures, the net built-in electric field can be defined as[181,182]

$$E_{bi} = E_{in} + E_{dp} = E_{in} + \frac{-P}{\varepsilon_0 \varepsilon_F}\left(\frac{2\varepsilon_F/d}{2\varepsilon_F/d + \varepsilon_e/\lambda}\right), \quad (1)$$

where E_{in} is the internal electric field in the ferroelectric/metal interface, E_{dp} is the depolarization field of the ferroelectric layer, ε_F is the relative dielectric constant of the ferroelectric layer, ε_e is the relative dielectric constant of the electrode layer, λ is the screening length, P is the polarization and d is the thickness of the ferroelectric layer.[181,182] In eqn (1), the enhanced ferroelectric polarization of the BFO/$BaTiO_3$ multi-

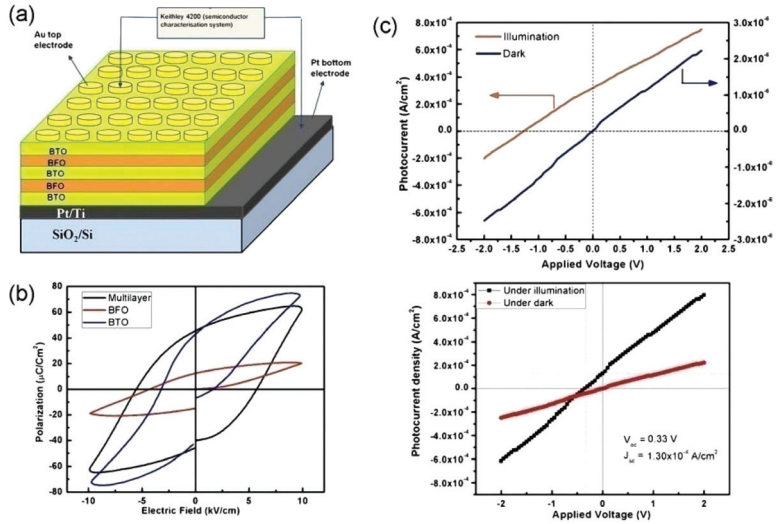

Fig. 4 (a) Schematic of the metal/ferroelectric/metal capacitor configuration with a BFO/$BaTiO_3$ multilayer. (b) Room-temperature ferroelectric hysteresis curves of bare BFO, bare $BaTiO_3$ and multilayered BFO/$BaTiO_3$. (c) *J*–*V* curves of the multilayered BFO/$BaTiO_3$ (in the upper panel) and BFO single layer (in the lower panel) under both dark conditions and illumination of violet laser light (λ = 405 nm) with an intensity of 160 mW cm^{-2}. Adapted with permission from ref. 160. Copyright 2015, AIP Publishing.

layers can enhance the net built-in field, which accelerates the separation of light-induced charge carriers and the resultant larger V_{OC}, than that of the BFO single layer. These results demonstrate that it is a practicable way to modulate the photovoltaic effects in the metal/BFO/metal structures by engineering the ferroelectric BFO layer.

Moreover, the photocurrent density can be increased and the energy conversion efficiency along with a broader applicable solar spectrum is improved by reducing the band gap in ferroelectric materials with the remaining ferroelectric polarization.[169,180,183] So, several heterostructures or superlattices will be illustrated to reduce the band gap of BFO. By fabricating an alloyed $BiCrO_3$/BFO film, Qiao *et al.* realized a band gap reduction of nearly 0.8 eV.[184] Nie *et al.* have fabricated a $BiCrO_3$/BFO bilayer by the sol-gel method[185] and epitaxial $BiCrO_3$/BFO heterostructures by pulse laser deposition, where the photocurrent density can reach ~0.013 mA cm^{-2}.[180] Significantly, Nechache *et al.* have grown the double perovskite Bi_2CrFeO_3 and successfully tailored the band gap, which realizes a considerably large energy conversion efficiency of 8.1%.[123] Zhang *et al.* also predicted a remarkable reduction of the band gap in the $BiCrO_3$/BFO superlattices by first-principles calculations.[183]

The physical characteristics of the metal/BFO/metal structures can also be modified by selecting the electrode materials. Transparent graphene[87,122] and hydrophilic RGO[39] show a high carrier mobility, electric conductivity and transparency in the visible light spectral region. Gupta *et al.* have grown graphene/$BiFe_{0.95}Si_{0.05}O_3$(BFSiO)/ITO/glass and reverse glass/ITO/BFSiO/graphene configurations by the bottom-up spin coating technique (Fig. 5a and b),[122] where switchable photovoltaic effects with repeatable and stable instantaneous responses appear in both the configurations (Fig. 5c–e). The bilayered-graphene/BFO heterostructures[87] with a switchable photovoltaic effect were also fabricated by pulsed laser deposition. Meanwhile, the J_{SC} and V_{OC} responses in either the graphene/BFSiO/ITO[122] or graphene/BFO/Pt[87] structure are less than 100 ms. The photovoltaic effects in the graphene/BFO-based heterostructures pave the way for exploring the optical modulation of two-dimensional materials and BFO, which offers opportunities to develop multifunctional devices.

BFO with photovoltaic effects can also serve as a photoelectrode in photoelectrochemical water splitting. However, the recombination of photo-generated e–h pairs in a pure BFO photoelectrode is rapid, which results in a low photoelectrochemical performance. In order to improve the photoelectrochemical performance, BFO-based composite photoelectrodes are considered. RGO has a better hydrophilic character than graphene and a higher conductivity than the normal graphene oxide, which is a suitable candidate to improve the photoelectrochemical performance of the BFO photoelectrode. Ren *et al.* fabricated RGO/BFO composite photoelectrodes with switchable photovoltaic effects, where polycrystalline BFO films were prepared by the sol-gel method and RGO nanosheets were decorated on BFO films by the dip-coating method.[39] In particular, the photoelectrochemical performances are evidently enhanced in the optimized RGO3/BFO sample (Fig. 6),[39] where J_{SC} has a 600% improvement and the incident photo-to-current conversion efficiency (IPCE) shows a threefold enhancement. In Fig. 6d, IPCE in the range of 400–550 nm can be ascribed to the optical absorption of BFO (Fig. 6c), where the IPCE response at 400 nm increases from 0.15% in pure BFO to 0.43% in RGO3/BFO films.[39] The generated photocurrent at 520 nm is consistent with the band gap of BFO (Fig. 6d), which excludes the possibility of a photocurrent induced in RGO. The improved photoelectrochemical perform-

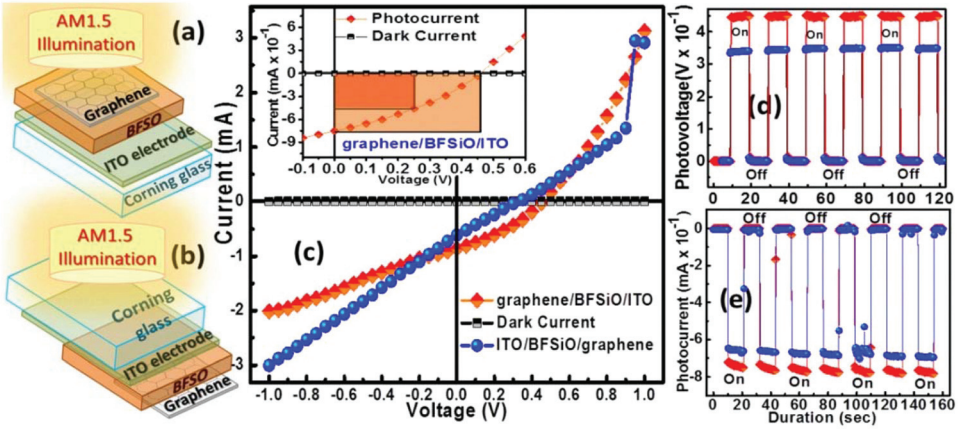

Fig. 5 Schematic of the (a) graphene/BFSiO/ITO/glass and (b) glass/ITO/BFSiO/graphene configurations. (c) *I*–*V* characteristics of the graphene/BFSiO/ITO structure under dark conditions and illumination with standard AM 1.5 with a power density of 100 mW cm^{-2} in a Keithley model 2401 electrometer. (d) Transient open-circuit voltage and (e) short-circuit current response for consecutive light ON and OFF cycles of ~10 s. Adapted with permission from ref. 122. Copyright 2015, AIP Publishing.

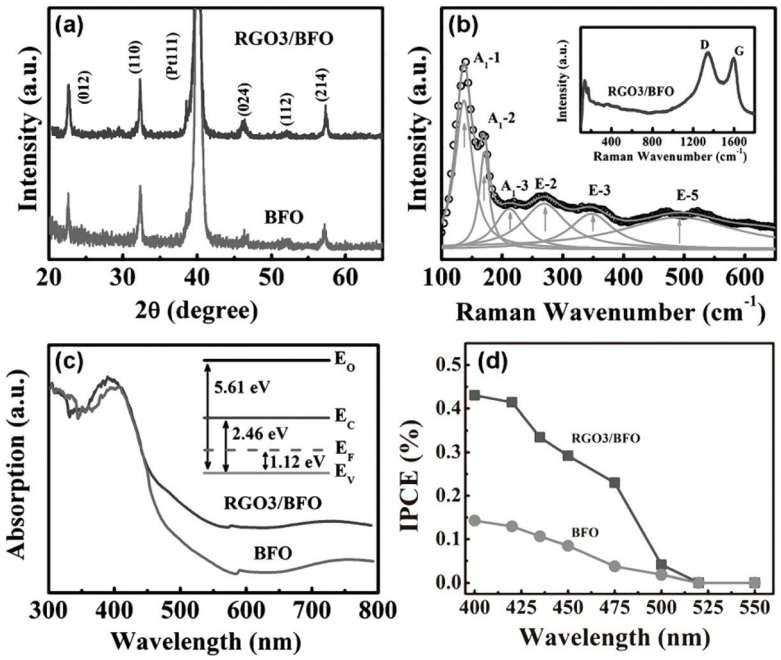

Fig. 6 (a) X-ray diffraction patterns of the pristine BFO and RGO3/BFO films. (b) Raman scattering spectra of the RGO3/BFO films (measured spectra: open circles and fitted spectra: thick solid lines) and the decomposed active modes (thin solid lines and arrows). The inset shows the Raman scattering spectra of RGO3/BFO films. (c) UV-vis absorption of pristine BFO and RGO3/BFO films. The inset shows the schematic energy band alignment of BFO. E_O, E_F, E_V, and E_C represent the vacuum level, Fermi level, valence band and conduction band of BFO, respectively. (d) IPCE as a function of the wavelength for pristine BFO and RGO3/BFO films at 0 V *versus* Ag/AgCl. Adapted with permission from ref. 39. Copyright 2017, Wiley.

ances in the optimized RGO3/BFO sample provide the foundation for developing efficient and multifunctional BFO-based ferroelectric photoelectrodes, while the switchable photovoltaic effect is absent in the conventional semiconducting photoelectrodes. Meanwhile, the feasible and low-cost fabrication methods of RGO3/BFO composite electrodes are beneficial for extending the multifunctional ferroelectric photoelectrodes.

The light-induced V_{OC} in ferroelectric or ferroelastic materials can exceed its band gap.[60,179,186] In 2010, Yang *et al.* demonstrated the electrostatic potentials of a ferroelectric domain wall in BFO films,[187] which can separate the photogenerated charge carriers and result in an above-bandgap voltage.[60] Lee *et al.* also demonstrated domain-dependent photovoltaic effects in Pt/BFO/$SrRuO_3$ heterostructures.[188] As shown in Fig. 7, the diode polarity and light-induced J_{SC} and V_{OC} in pure polarization-up or polarization-down domains disappear in polarization-mixed domains.[188] Moreover, the disappeared photovoltaic effects in the mixed domains indicate

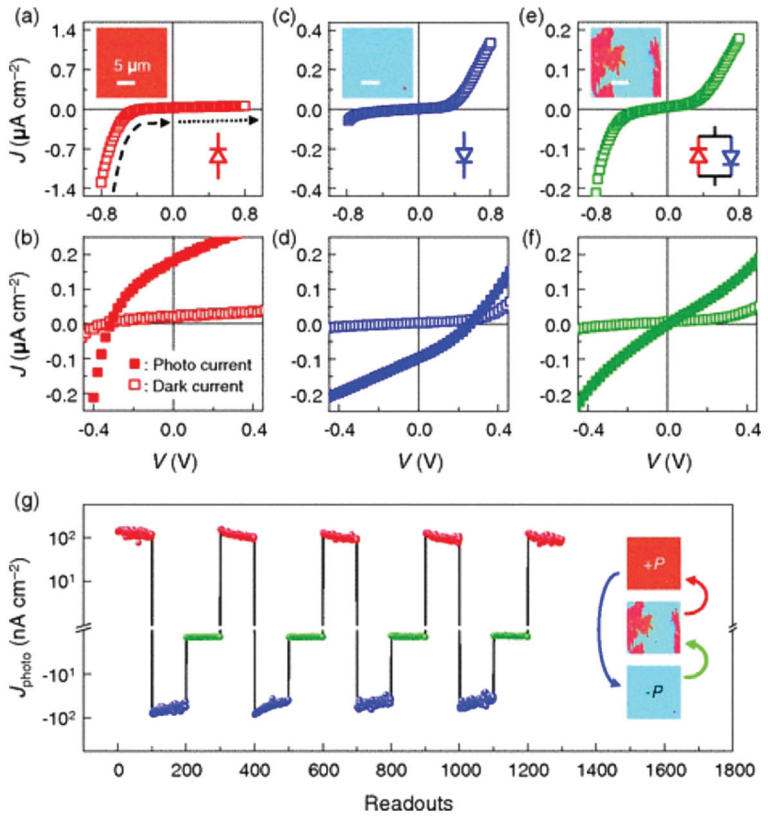

Fig. 7 (a–f) *J–V* curves of dark (open squares) and illuminated (closed squares) Pt/BFO/$SrRuO_3$ thin film capacitors. The insets show the (a and b) upward, (c and d) downward and (e and f) upward/downward mixed-polarization domains, respectively. (g) Cycling test for the nonvolatile photovoltaic effects in the Pt/BFO/$SrRuO_3$ capacitors with three states. Adapted with permission from ref. 188. Copyright 2011, American Physical Society.

the third state, rather than the customer polarization-up and polarization-down states, as shown in Fig. 7g. Such three-state photovoltaic characteristics also show no signs of fatigue (Fig. 7g).

The domain wall dependent photovoltaic effects have been proved in many subsequent results of BFO films, which are mainly connected with 71° and 109° domains.[189–191] Owing to the controllable ferroelectric polarization, the domain-dependent above-band-gap photovoltaic responses in BFO are tunable by an electric field. The previously reported V_{OC} reached 50 V by tuning the conductivity of domain walls.[191] It is obvious that the variable ferroelectric domains offer a new way to modulate the photovoltaic effects in pristine BFO films. Such domain effects on the photovoltaic characteristics will be taken seriously in doped BFO and other ferroelectric materials with multidomain structures.

Additionally, Maksymovych *et al.* reported that the ferroelectric domain walls in BFO exhibit inherently dynamic conductivity,[192] mimicking the memristive behavior. By applying an electric field, the domain walls in BFO show a transition from localized insulation to conductance by an order of magnitude because of the metastable conductance states.[192] Bhatnagar *et al.* demonstrated that the above-band-gap light can induce an evident change of conductivity in strained BFO films, which can be ascribed to the trapping characters of the sub-band levels.[193,194] However, by considering the domain-dependent above-band-gap photovoltaic characteristics in BFO,[121,187] the special conductivity in BFO under above-band-gap light should be related to the domain structures and its dynamic conductivity, which should be taken into account in the future.

Moreover, since the anisotropic domain walls in $REMnO_3$ (RE = Sc, Y, Ho, *etc.*) crystals are discovered,[195,196] Jin *et al.* studied the conductivity of head-to-head, tail-to-tail and head-to-tail domain walls in BFO films,[197] where the tail-to-tail domain walls are more conductive than the other two domain walls. These results demonstrate the anisotropic ferroelectric domain walls in BFO. However, the electron transport in the domain walls of BFO can be tailored with an external magnetic field, such as the anisotropic magnetoresistance,[198] which indicates the possible magnetic characteristics of domain walls. In the BFO films and heterostructures, the anisotropic conductivity and magnetoresistance in the ferroelectric domain walls of BFO show the possible magnetoelectric coupling in domain scales. It can be noted that the domain walls can be another degree of freedom to induce and stimulate the electrical, magnetic and optical properties in BFO-related heterostructures.

On the basis of the photovoltaic effects, Yang *et al.* have successfully observed the fully optical control of the ferroelec-

tric polarization in $(001)_{pc}$-BFO/(110)-$TbScO_3$ heterostructures,[199] which gives new insight into the interacted light and ferroic orders in the BFO-based heterostructures. The photovoltaic effects in the BFO-based heterostructures are attributed to the photo-generated e–h pairs separated by the ferroelectric polarization, interfacial barriers or domain wall induced electrostatic potentials.[37,187] However, Li *et al.* have studied the electrode-free photovoltaic effects in phase-pure BFO films,[200] where the diffusion of charge-neutral excitons in BFO and their subsequent separation at interfaces result in photovoltaic effects. The new results are in contrast to the conventional separation of photo-generated e–h pairs in BFO; so more efforts should be made to study the charge dynamics of photovoltaic effects in BFO-based heterostructures.

2. Barrier modulation in metal/metal-buffer-layer/$BiFeO_3$/metal. As discussed in subsection III.A.1, the photovoltaic effects in the metal/BFO/metal structures can be modulated by engineering the ferroelectric layers and choosing special electrodes. In this section, a metal buffer layer is introduced in the basic metal/BFO/metal structures to tailor the photovoltaic characteristics. Lu *et al.* have prepared Au/Ti(Cr)/T-BFO/LSMO structures by pulsed laser deposition (Fig. 8a and b), where the ferroelectric polarization in the epitaxial T-BFO is switched, as shown in Fig. 8c and e.[132] The work function of Ti and Cr metals is close to that of BFO, which has a small barrier height at the Ti(Cr)/BFO interfaces, which can benefit the separation of photo-induced e–h pairs. In particular, in Fig. 8d and f, the photovoltaic response is different in the Ti- and Cr-buffered systems. In the Au/Ti/T-BFO/LSMO structure (Fig. 8d), the negative V_{OC} and positive J_{SC} appear in either polarized-up or polarized-down states. However, in the Cr-buffered case (Fig. 8f), the cell with a polarized-up state shows a negative V_{OC} and a positive J_{SC}. However, the cell with a polarized-down state shows a positive V_{OC} and a negative J_{SC}. These different photovoltaic responses in the Ti- and Cr-buffered systems can be attributed to the different net built-in electric fields E_{bi} [132]

$$E_{bi} = E_{in} \pm |E_{dp}| = \frac{W_{Ti/Cr} - W_{LSMO}}{qd} \pm |E_{dp}|, \quad (2)$$

where the work function of Ti, Cr and LSMO is W_{Ti} = 4.33 eV, W_{Cr} = 4.50 eV and W_{LSMO} = 4.96 eV, respectively.

In both the Ti- and Cr-buffered systems with a polarized-up state (Fig. 9a and c), both the E_{in} and E_{dp} point towards the LSMO, which obeys the formula $E_{bi} = E_{in} + E_{dp}$. Hence, the built-in electric field in two systems produces a positive J_{SC}. Secondly, in the polarized-down state (Fig. 9b and d), E_{dp} is antiparallel to E_{in}, which obeys the formula $E_{bi} = E_{in} - E_{dp}$. So, if $|E_{in}| > |E_{dp}|$, the net E_{bi} has the same direction as E_{in} (*i.e.*, pointing towards LSMO), which can induce a positive J_{SC}. Such a case is consistent with the Ti-buffered system. Meanwhile, if $|E_{in}| < |E_{dp}|$, the net E_{bi} is opposite to E_{in} (*i.e.*, pointing towards the metal buffer layers), which can produce a negative J_{SC}. This formula can exactly describe the Cr-buffered system. These results demonstrate that the photovoltaic characteristics in the metal/BFO/metal structures can be manipulated by selecting a suitable metal buffer layer and switching the ferroelectric polarization in T-BFO layers.

3. Barrier modulation in metal/semiconductor–buffer–layer/BFO/metal. In order to improve the photovoltaic responses in the metal/BFO/metal structures, a semiconductor buffer layer is introduced,[86] which can generate many more e–h pairs by light illumination and form a barrier at the semiconductor/BFO interfaces, which can enhance the separation of the photo-generated e–h pairs. In Fig. 10a, the ITO/BFO/Pt structure[86] shows a large V_{OC} and a small J_{SC}, while the ITO/ZnO/Pt structure has a large J_{SC} and a small V_{OC} of nearly 0 eV. However, the ITO/ZnO/BFO/Pt structure[86] shows an evidently enhanced J_{SC} on comparing with the ITO/BFO/Pt system

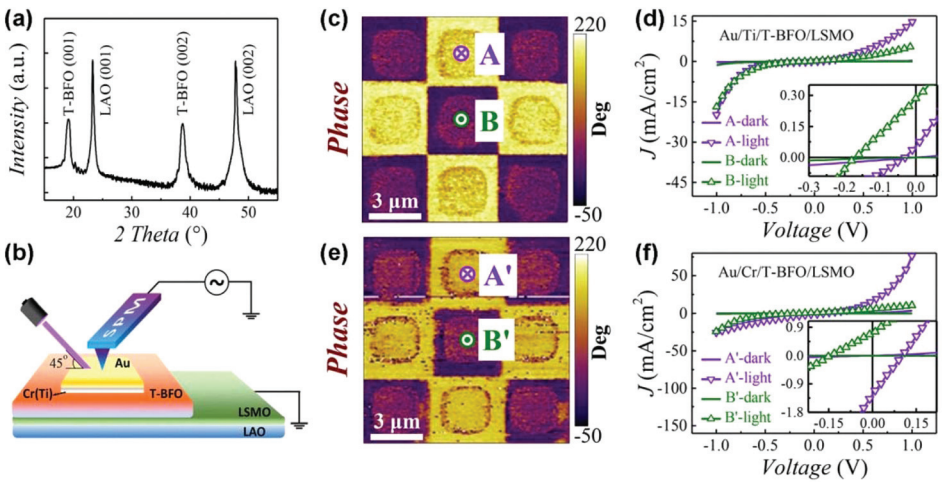

Fig. 8 (a) X-ray diffraction pattern of the T-BFO/LSMO sample on a (001)-$LaAlO_3$ single crystal wafer. (b) Setup for the measurement of the local photovoltaic effects. Local ferroelectric switching and the *J*–*V* curves of the (c and d) Au/Ti/T-BFO/LSMO and (e and f) Au/Cr/T-BFO/LSMO heterostructures. Circle-fork A(A') represents the polarized-down state, and circle-dot B(B') represents the polarized-up state. Adapted with permission from ref. 132. Copyright 2017, American Chemical Society.

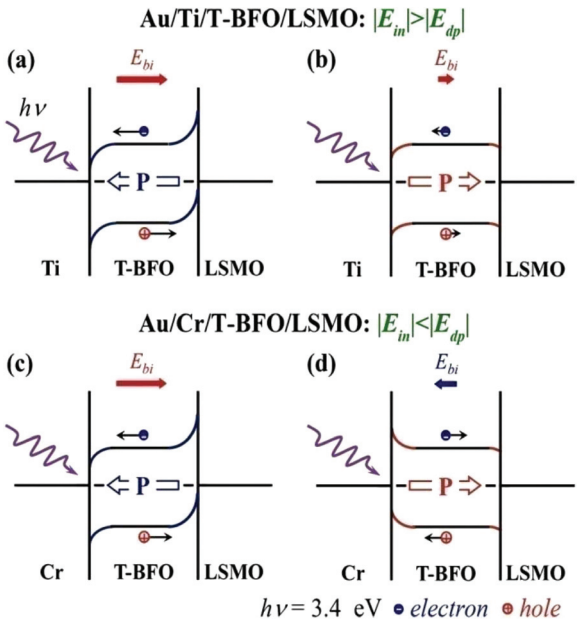

Fig. 9 Schematic diagram of the energy levels and photo-generated carrier transfer process of the Au/Ti(Cr)/T-BFO/LSMO structures with the (a and c) polarized-up and (b and d) polarized-down states. Adapted with permission from ref. 132. Copyright 2017, American Chemical Society.

(Fig. 10a), which can be attributed to the abundant e–h pairs induced in the semiconducting ZnO. In particular, the band alignments in the ITO/ZnO/BFO/Pt structure[86] result in the Schottky barrier and n^+–n junction at the BFO/Pt and ZnO/BFO interfaces (Fig. 10b), where two built-in fields accelerate the separation and transport of the photo-generated e–h pairs. Meanwhile, as seen in Fig. 10c, the energy conversion efficiency η of the ITO/ZnO/BFO/Pt structure is also significantly improved by introducing the semiconducting ZnO buffer layer, where the largest η is ~0.33%. These results demonstrate that the barriers at the semiconductor–buffer–layer/BFO interfaces have a prominent modulation of the photovoltaic effects in the BFO-based heterostructures. Similar barrier modulation of the photovoltaic characteristics also appears in the p–i–n type NiO/BFO/ZnO and MoO_3/BFO/ZnO heterojunctions,[36] where the type-II band alignment at the NiO/BFO(p–i) and BFO/ZnO(i–n) interfaces favors the separation of carriers.

Notably, the ferroelectric BFO with the visible-light-responsive photovoltaic effects is one of the third-generation photocatalysts due to its narrow band gap.[201] Stable, nontoxic and low-cost TiO_2 is the most studied material for solar-energy utilization, which can be further modified by ferroelectric BFO.[35] Zhu *et al.* deposited BFO nanoparticles on TiO_2 nanotube arrays by an ultrasonic-immersion strategy, where the BFO/TiO_2 composites on Ti sheets are used as a composite elec-

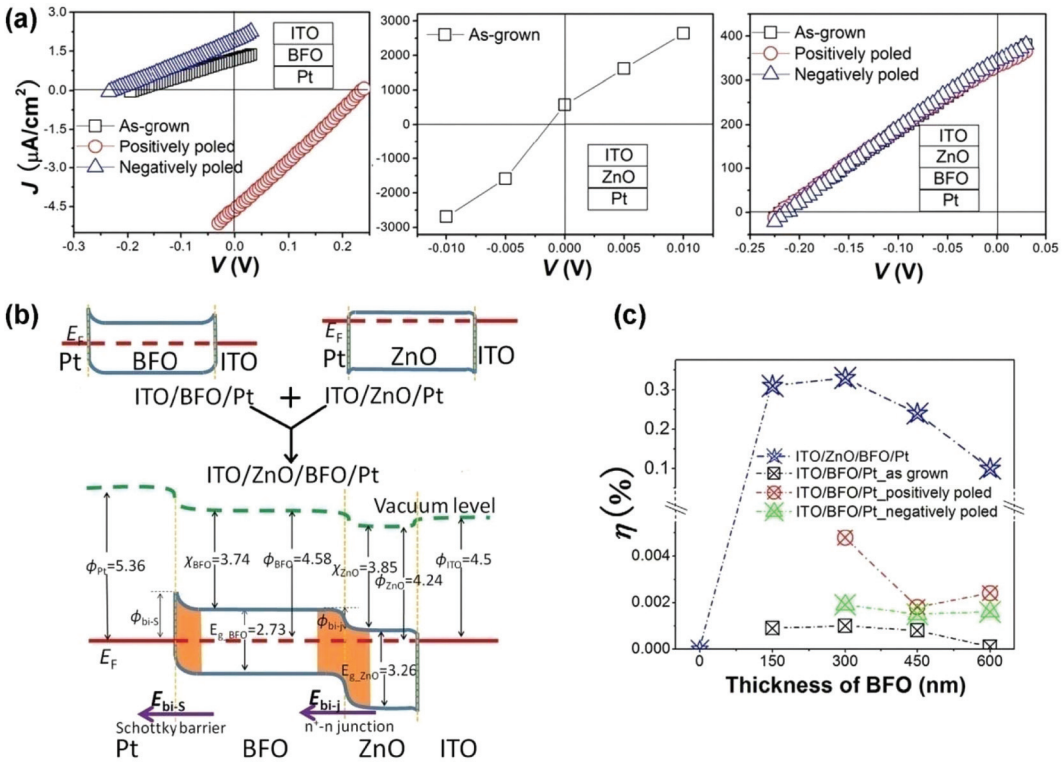

Fig. 10 (a) Photovoltaic J–V characteristics and (b) energy band diagrams of the ITO/BFO/Pt, ITO/ZnO/Pt and ITO/ZnO/BFO/Pt heterostructures. (c) Energy conversion efficiency η as a function of the BFO layer thickness in the ITO/BFO/Pt and ITO/ZnO/BFO/Pt heterostructures. A xenon light source (Hamamatsu LC8 with L8253 super-quiet xenon lamp) giving 22.3 mW cm^{-2} blue monochromatic light was used for the photovoltaic measurements. Adapted with permission from ref. 86. Copyright 2014, AIP Publishing.

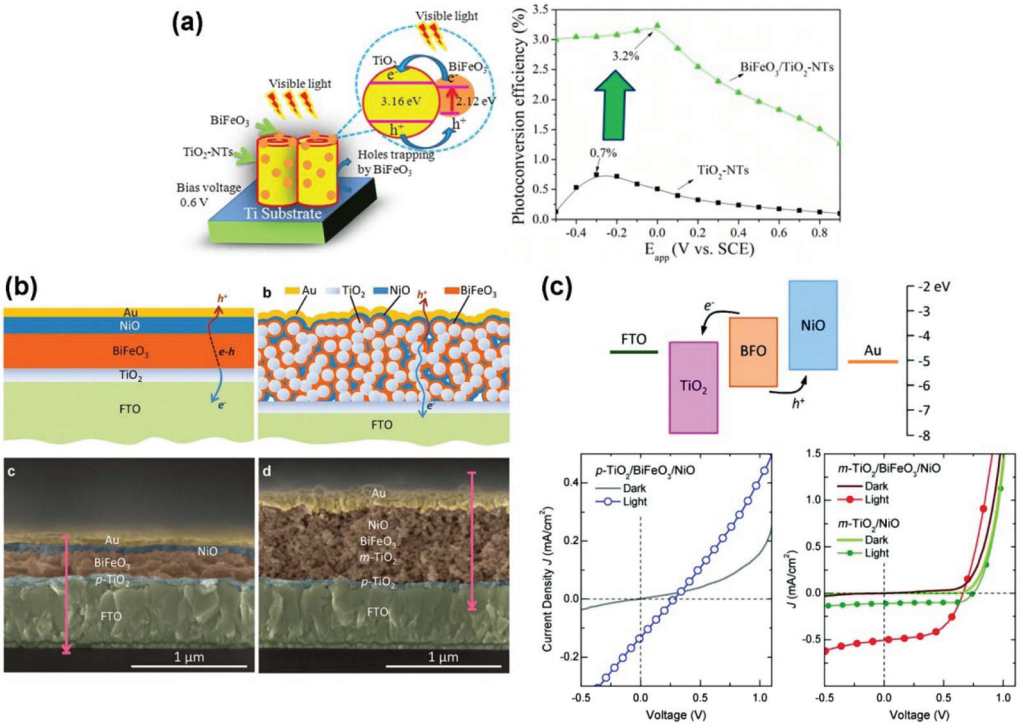

Fig. 11 (a) Diagram of the photo-induced electron generation, separation and transfer pathway in the BFO/TiO_2-nanotube arrays by visible-light excitation. The photoconversion efficiency as a function of the applied potential in the BFO/TiO_2-nanotube arrays and bare TiO_2-nanotube arrays at a visible-light irradiation of 140 mW cm^{-2}. Adapted with permission from ref. 35. Copyright 2014, American Chemical Society. (b) Schematic of device architectures and cross-sectional scanning electron microscopy images of planar and mesostructured heterojunctions, respectively. (c) Energy levels of the TiO_2/BFO/NiO heterojunctions and *J*–*V* curves of planar and mesostructured TiO_2/BFO/NiO heterojunctions. Adapted with permission from ref. 128. Copyright 2017, Wiley.

trode.[35] In Fig. 11a, the photoconversion efficiency in the BFO/TiO_2/Ti composite electrode is much higher than that of the TiO_2/Ti electrode because of the enhanced visible-light utilization in BFO and the barrier formed between BFO and TiO_2.[35] Here, the photoconversion efficiency η from light energy to chemical energy under a bias potential can be described as

$$\eta(\%) = \frac{P_{\text{output}} - P_{\text{electrical-input}}}{P_{\text{optical-input}}} \times 100\% = \frac{j_p\left(E^0_{\text{rev}} - |E_{\text{app}}|\right)}{I_0} \times 100\%, \quad (3)$$

where P_{output} is the total power output, $P_{\text{electrical-input}}$ is the electrical power input, $P_{\text{optical-input}}$ is the optical power input, j_p is the photocurrent density, E^0_{rev} is the standard reversible potential, E_{app} is the applied bias and I_0 is the power density of the incident light.[35] The BFO/TiO_2/Ti composite electrode also shows a high efficiency in the photoelectrocatalytic degradation of rhodamine B under visible light. Besides, Wang *et al.* demonstrated that the morphology of BFO in heterostructures can greatly affect the photovoltaic characteristics,[128] especially the mesoporous structures. In Fig. 11c, the band alignment of the TiO_2/BFO/NiO structure makes the electrons move toward TiO_2 and the holes toward NiO, which benefits the separation of e–h pairs generated in BFO. However, as seen in Fig. 11b and c, the mesoporous m-TiO_2/BFO/NiO heterojunctions have much more m-TiO_2/BFO and BFO/NiO interfaces than the planar p-TiO_2/BFO/NiO structure, resulting in a more efficient separation of e–h pairs generated in BFO grains and a larger $V_{OC}(J_{SC})$. These photovoltaic effects in the BFO/TiO_2-related systems provide the foundation for developing the BFO-related photoelectrocatalysts and solar cells.

Additionally, visible-light absorbing ferroelectric semiconductors have been discovered,[202] such as the Sn chalcogenide ferroelectrics $Sn_2P_2S_6$ and $Sn_2P_2Se_6$ with indirect band gaps of 2.20 eV and 1.55 eV. However, the photovoltaic performances in these ferroelectric semiconductors are inferior to those of the oxides. It should be noted that BFO can be used to modulate the photovoltaic effect in the ferroelectric semiconductor materials. Dong *et al.* incorporated an ultrathin BFO layer into the semiconducting $BiVO_4$,[203] which can increase the J_{SC} by 2 fold to 0.14 mA cm^{-2} and increase the V_{OC} by 5 fold to 1 V compared to pristine $BiVO_4$. Since BFO can influence the asymmetric $BiVO_4$, the photovoltaic effect in the asymmetric chalcogenide ferroelectrics might be tunable with BFO.

4. Switchable conduction modes in semiconductor-electrode/$BiFeO_3$/metal. As discussed in subsection III.A.3, the semiconductors can serve as a buffer layer to modulate the photovoltaic effects in BFO-based heterostructures. However, the semiconductors can also be used as electrodes to engineer the photovoltaic responses. Hu *et al.* have used the semicon-

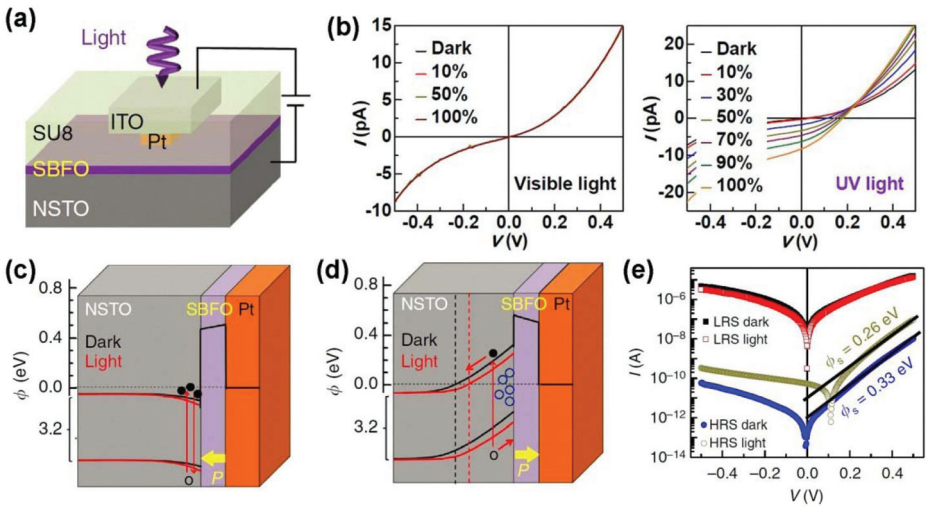

Fig. 12 (a) Schematic structure of the Nb:$SrTiO_3$/$Sm_{0.1}Bi_{0.9}FeO_3$/Pt FTJs. (b) *I*–*V* curves of the Nb:$SrTiO_3$/$Sm_{0.1}Bi_{0.9}FeO_3$(3 nm)/Pt FTJs under visible light illumination (max-302, 385–740 nm, maximum intensity of 1.5 W cm^{-2}) and ultraviolet light illumination (max-303, 250–385 nm, maximum intensity of 60 mW cm^{-2}). (c and d) The band alignments of the FTJs at different polarization directions (yellow arrow) under darkness and light illumination, respectively. The black filled and empty circles in (c and d) represent the photon-excited electrons and holes, respectively. (e) Typical *I*–*V* data of the LRS and HRS in the low bias region after writing with voltages of +3 and −16 V, both in the dark and under ultraviolet light illumination. Adapted with permission from ref. 37. Copyright 2016, Nature Publishing Group.

ducting Nb-doped $SrTiO_3$ as the bottom electrode to explore the optically controlled electroresistance in BFO-based FTJs (Fig. 12a), where Sm-doped BFO can decrease the leakage current.[37] In the Nb:$SrTiO_3$/$Sm_{0.1}Bi_{0.9}FeO_3$/Pt FTJs,[37] the photovoltaic effects (Fig. 12b) can be increased by ultraviolet light (max-303, 250–385 nm), but not visible light (max-302, 385–740 nm). Here, the band gap of 2.7 eV (460 nm) in $Sm_{0.1}Bi_{0.9}FeO_3$ lies in the visible light range, while the band gap of 3.2 eV (388 nm) in Nb:$SrTiO_3$ is on the edge of the ultraviolet light. So, the light adsorption in the Nb:$SrTiO_3$/$Sm_{0.1}Bi_{0.9}FeO_3$/Pt FTJs can be mainly ascribed to semiconducting Nb:$SrTiO_3$, instead of $Sm_{0.1}Bi_{0.9}FeO_3$.

Particularly, the photovoltaic responses in the Nb:$SrTiO_3$/$Sm_{0.1}Bi_{0.9}FeO_3$/Pt FTJs are highly dependent on the electroresistance states (Fig. 12e), where ultraviolet illumination has almost no effect on the low resistance state (LRS) but an evident influence on the high resistance state (HRS). Such a phenomenon can be attributed to the different band-bending-induced conduction modes in the LRS and HRS. As the polarization in $Sm_{0.1}Bi_{0.9}FeO_3$ points towards the bottom Nb:$SrTiO_3$ electrode (Fig. 12c), the carrier accumulates at the Nb:$SrTiO_3$/$Sm_{0.1}Bi_{0.9}FeO_3$ interface, which results in a direct tunneling and the corresponding LRS with a parabolic *I*–*V* curve in FTJs.[37] The direct tunneling in LRS is well explained by the WKB approximation[204]

$$J(V) = \frac{-4em^*}{9\pi^2\hbar^3} \times \frac{\exp\left\{\alpha(V)\left[(\phi_2 - eV/2)^{3/2} - (\phi_1 + eV/2)^{3/2}\right]\right\}}{\alpha^2(V)\left[(\phi_2 - eV/2)^{1/2} - (\phi_1 + eV/2)^{1/2}\right]^2} \times \sin h\left\{\frac{3}{2}\alpha(V)\left[(\phi_2 - eV/2)^{1/2} - (\phi_1 + eV/2)^{1/2}\right]\frac{eV}{2}\right\}, \quad (4)$$

$$\alpha(V) = \frac{4d(2m^*)^{1/2}}{3\hbar(\phi_1 - \phi_2 + eV)}, \quad (5)$$

where $\varphi_{1,2}$ is the tunneling barrier height at two interfaces and m^* is the effective mass of electrons in the $Sm_{0.1}Bi_{0.9}FeO_3$ tunnel barrier.[204] By using the $\phi_{1,2}$ = 0.48(0.47) eV parameters at the Nb:$SrTiO_3$/$Sm_{0.1}Bi_{0.9}FeO_3$ (Pt/$Sm_{0.1}Bi_{0.9}FeO_3$) interface and $m^* = 0.69m_0$, Hu *et al.* achieved a good fitting between the theoretical and experimental *I*–*V* curves.[37] However, at the opposite polarization (Fig. 12d), the carrier at the Nb:$SrTiO_3$/$Sm_{0.1}Bi_{0.9}FeO_3$ interface is depleted due to the charge screening effect, which leads to the depletion layer and the resultant HRS.[37] The direct tunneling mechanism cannot satisfy the experimental *I*–*V* curve in the HRS, which is described by the Schottky thermionic emission[37]

$$J(V) = A^*AT^2 \exp(-\phi_s/k_BT)\exp(-\alpha_T d\sqrt{\phi_T})\exp(qV/nk_BT - 1) = A^{**}AT^2\exp(-\phi_s/k_BT)\exp(qV/nk_BT - 1). \quad (6)$$

In eqn (6), A is the junction area, A^* is the standard Richardson constant, ϕ_s is the Schottky barrier height, ϕ_T is the average tunneling barrier height, T is the temperature and n is the ideality factor.[37] The different conduction modes in the LRS and HRS lead to a colossal TER of 10^5 in the Nb:$SrTiO_3$/$Sm_{0.1}Bi_{0.9}FeO_3$/Pt FTJs.

The HRS and LRS in the Nb:$SrTiO_3$/$Sm_{0.1}Bi_{0.9}FeO_3$/Pt FTJs show the different conduction modes and photovoltaic responses, which offers a new optical route to the memory state of FTJ-based devices. Besides, the Nb doping content in $SrTiO_3$ will affect the semiconducting characteristics of Nb:$SrTiO_3$ and the interfacial depletion region, which can modulate the HRS and related photovoltaic responses. These results

indicate the various control approaches on the photovoltaic effects in the BFO-based heterostructures with a semiconductor electrode.

Besides, except for the photovoltaic effects, other optoelectronic phenomena have also been explored in the BFO-based heterostructures. In the current-perpendicular-to-plane Nb:$SrTiO_3$/$Sm_{0.1}Bi_{0.9}FeO_3$/Pt junctions,[205] a colossal X-ray-induced persistent photoconductivity is achieved by enhancing six orders of magnitude, which can be attributed to the X-ray-modulated formation and ionization of oxygen vacancies and the reduced interfacial Schottky barriers. The photostriction phenomenon has been demonstrated in BFO crystals, where the size of BFO can be tailored by light illumination.[120,206] Particularly, the optical control of the ferroelectric polarization switching has been demonstrated in $BaTiO_3$/MoS_2 heterostructures, and is attributed to the redistributed photo-generated carriers and charge screening at the $BaTiO_3$/MoS_2 interface.[207] Such a photo-controlled polarization reversal will be addressed in other ferroelectric/semiconducting heterostructures.

B. Electric field control of magnetism

In the BFO/ferromagnet heterostructures,[43,44] the electric-field control of magnetism is based on two types of coupling: (i) the internal magnetoelectric coupling in antiferromagnetic and ferroelectric BFO; and (ii) the magnetic coupling between antiferromagnetic BFO and other ferromagnetic materials. The first coupling enables the electric field control of the antiferromagnetic order in BFO, and the controlled antiferromagnetic order of BFO can modulate the ferromagnetism by the second coupling. In the multiferroic BFO/ferromagnet heterostructures, such an indirect magnetoelectric coupling enables the effective electric-field control of magnetization, which will be discussed with the aspects of magnetization reversal and magnetic anisotropy in following subsections III.B.1 and III.B.2. Piezoelectric materials have also been utilized to tailor the magnetic anisotropy in the BFO/ferromagnet heterostructures, which is based on the electric-field-induced strain (see subsection III.B.3). In particular, the ferroelectric domain and antiferromagnetic domain in multiferroic BFO highly interact with the ferromagnetic domains in the BFO/ferromagnet heterostructures, which are theoretically and experimentally analyzed in the whole III.B part.

1. Electric field control of magnetization reversal by magnetoelectric coupling. Magnetoelectric coupling includes two types:[208] one is the direct magnetoelectric effect that describes the coupling between polarization and the magnetic field

$$\Delta P = \alpha_H \Delta H. \quad (7)$$

The other is the converse magnetoelectric effect that illustrates the coupling between magnetization and the electric field

$$\mu_0 \Delta M = \alpha_E \Delta E. \quad (8)$$

In this section, the converse magnetoelectric effect will be focused on to explore the electric-field control of magnetization. In the BFO/ferromagnet multiferroic heterostructures, the electric-field control of magnetism can be ascribed to the ferroelectric and antiferromagnetic coupling in multiferroic BFO,[62,209] as shown in Fig. 13. In BFO films, the antiferromagnetic vector and ferroelectric polarization before and after electric poling can be reflected by the photoemission electron microscopy and in-plane piezoelectric force microscopy images, respectively. In Fig. 13c and d, the ferroelectric polarization in regions 1 and 2 are reversed by the electric poling. In particular, the antiferromagnetic vectors in regions 1 and 2 can also be inversed by the electric poling (Fig. 13a and b). Hence, the antiferromagnetic domain switching is induced by switching the ferroelectric polarization, indicating the magnetoelectric coupling in the BFO film.

Furthermore, by considering the magnetic coupling between the antiferromagnetic and ferromagnetic properties, the electric-field modulated ferroelectric properties can tailor the ferromagnetic characteristics, as illustrated in Fig. 14a and e. In the $Co_{0.9}Fe_{0.1}$/BFO/$SrRuO_3$/$SrTiO_3$ structure,[43] Chu *et al.* observed the electric-field controlled magnetization of the $Co_{0.9}Fe_{0.1}$ layer, where the ferroelectric and ferromagnetic domains are evidently matched after either the first upward electric poling or the second downward poling (Fig. 14b and c). Such a phenomenon can be attributed to the collinear coupling between the direction of magnetization in $Co_{0.9}Fe_{0.1}$ and the projection of the ferroelectric-tunable antiferromagnetic plane in BFO, as illustrated in Fig. 14d. Finally, in Fig. 15a–c, the average magnetization direction of $Co_{0.9}Fe_{0.1}$ is reversibly rotated by 90° in an electric field. Heron *et al.* realized a magnetization reversal of 180° in $Co_{0.9}Fe_{0.1}$ in the $Co_{0.9}Fe_{0.1}$/BFO/$DyScO_3$ heterostructures (Fig. 15d and e).[49] This advantage can provide opportunities to write the magnetic state in data storage and spin valves. Besides, the reversible electric-field control of the exchange bias has also been experimentally observed in BFO/$La_{0.7}Sr_{0.3}MnO_3$ heterostructures,[210] which is attributed to the magnetic coupling between BFO and $La_{0.7}Sr_{0.3}MnO_3$, as shown in Fig. 14a. The electric-field control of the exchange bias is also tunable by the relative proportion of 109° domain walls in the BFO-based heterostructures.[211,212] The exchange bias in the BFO/$La_{0.7}Sr_{0.3}MnO_3$ heterostructures appears above the critical BFO layer thickness of 2 nm,[213] which indicates the film thickness effects on the exchange bias in other BFO/ferromagnet heterostructures.

The indirect coupling among the ferroelectricity, antiferromagnetism and ferromagnetism is practicable for the electric-field control of magnetism in the BFO-based heterostructures because of the interacting ferroelectric, antiferromagnetic and ferromagnetic domains. Besides, De Luca *et al.* observed the evolution of the voltage-tailored domain-pattern transfer across the BFO/$Co_{0.9}Fe_{0.1}$ interfaces by combining the optical second-harmonic generation and magnetic force microscopy,[214] where the varied orientation of the magnetic domains in the ferromagnetic $Co_{0.9}Fe_{0.1}$ layer is highly consistent with the in-plane direction of ferroelectric domains in BFO. These results directly present the domain-related magnetoelectric coupling in the BFO/ferromagnetic heterostructures. Additionally, the exchange bias occurs in not only the antiferromagnetic/ferro-

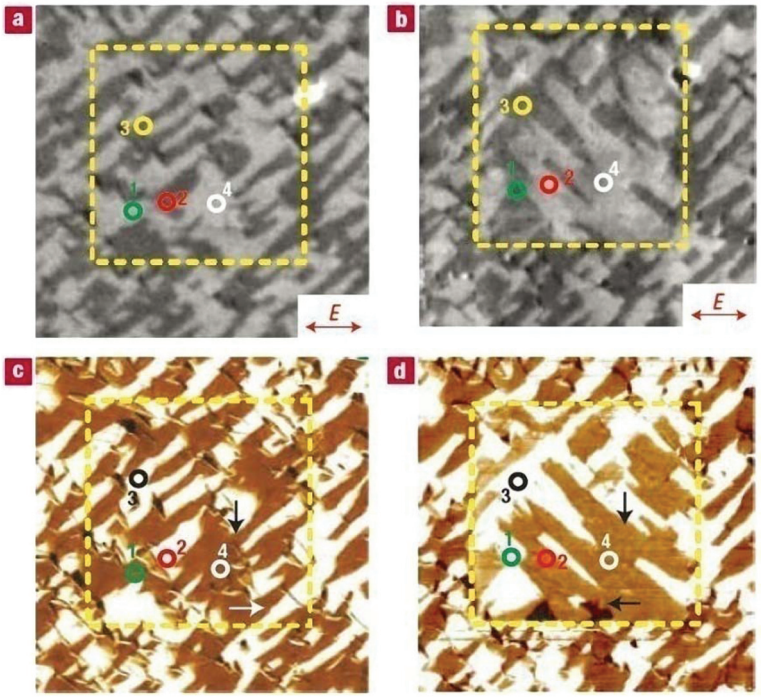

Fig. 13 (a and b) Photoemission electron microscopy and (c and d) in-plane piezoelectric force microscopy images of the same area of the BFO film (a and c) before and (b and d) after electric poling. Arrows in (a and b) indicate the X-ray polarization direction during the measurements. Arrows in (c and d) show the direction of the in-plane component of ferroelectric polarization. Regions 1 and 2 (marked with green and red circles, respectively) refer to 109° ferroelectric domain switching, whereas Regions 3 (black and yellow circles) and 4 (white circles) correspond to 71° and 180° domain switching, respectively. Adapted with permission from ref. 62. Copyright 2006, Nature Publishing Group.

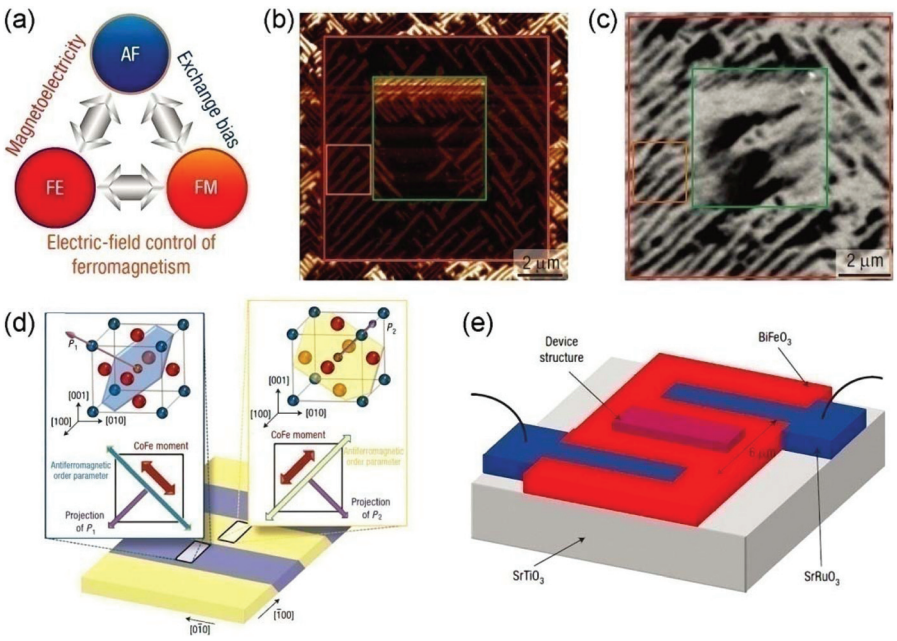

Fig. 14 (a) Schematic diagram of the electrical control of magnetism. (b) In-plane piezoelectric force microscopy image of the BFO film with large (10 μm, red square) and small (5 μm, green square) electrically switched regions in the $Co_{0.9}Fe_{0.1}$/BFO heterostructures. (c) X-ray magnetic circular dichroism–photoemission electron microscopy image taken at the Co L-edge of the CoFe film grown on the written pattern of $Co_{0.9}Fe_{0.1}$/BFO heterostructures. (d) Coupling mechanism among ferroelectricity, antiferromagnetism and ferromagnetism of the $Co_{0.9}Fe_{0.1}$/BFO heterostructures. (e) Schematic diagram of the coplanar epitaxial electrode device. Adapted with permission from ref. 43. Copyright 2008, Nature Publishing Group.

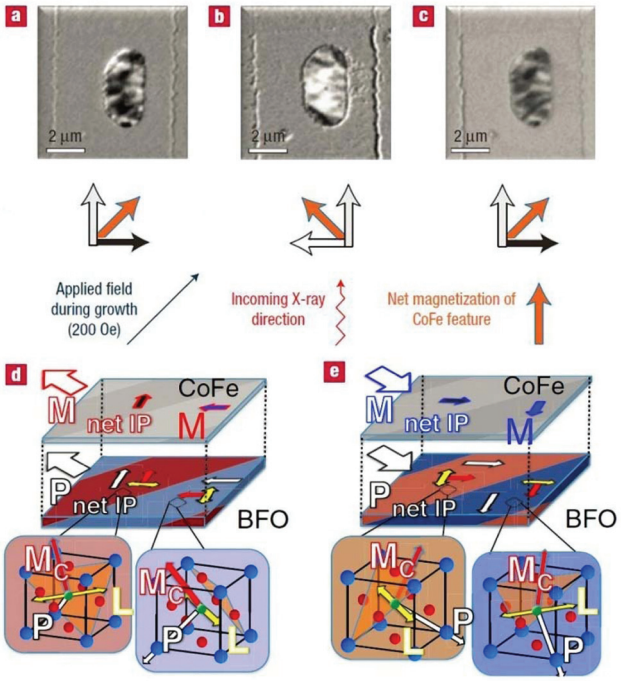

Fig. 15 X-ray magnetic circular dichroism–photoemission electron microscopy image taken at the Co L-edge of (a) the as-grown $Co_{0.9}Fe_{0.1}$/BFO/$SrRuO_3$/$SrTiO_3$ heterostructure, (b) after the first electrical switching and (c) after the second electrical switching. Adapted with permission from ref. 43. Copyright 2008, Nature Publishing Group. Schematic diagram of the electric field induced magnetization reversal of (d) the as-grown state $Co_{0.9}Fe_{0.1}$/BFO/$DyScO_3$ heterostructures and (e) after the first electric pulse. Adapted with permission from ref. 49. Copyright 2011, American Physical Society.

magnetic heterostructures but also the single-phase multiferroic materials, such as the long-period Aurivillius oxides.[215] However, on the basis of exchange bias, the further electric-field control of the exchange bias is the key part in the BFO/ferromagnet systems, which enables the exchange bias in heterostructures to be applied in data storage or sensors.

Particularly, BFO can also modulate the magnetization of shaped nanodots. Yao *et al.* fabricated special Co/BFO/(La,Sr)MnO_3/$SrTiO_3$ multiferroic heterostructures by pulsed laser deposition and nanosphere lithography techniques,[216] where (La,Sr)MnO_3 bottom electrodes were predeposited on $SrTiO_3$ substrates, then T-BFO films were sequentially deposited, and finally Co nanodot arrays were fabricated on the T-BFO films using a packed nanosphere template. In the Co/BFO/(La,Sr)MnO_3/$SrTiO_3$ heterostructures, the reversible and robust magnetic domain rotation of 180° appears in Co nanodots by applying an electric field at room temperature (see Fig. 16), which is consistent with the results of the micromagnetic simulations based on the Landau–Lifshitz–Gilbert ordinary differential equation and Green function method.[216,217] Moreover, in Fig. 17a and b, the magnetic order in Co nanodots can be rotated in a short time of ~10 ns by a small electric field within 10 V, where the magnetic rotation also shows a superior retention of nine months (Fig. 17b). Notably, besides the interfacial exchange coupling in the Co/BFO heterostructures, both the electric-field-induced piezostrain of BFO and the shape anisotropy of Co nanodots favor the electric-field driven magnetic rotation. The fast electric-field driven magnetic rotation in the shaped nanodots/BFO paves a new way to explore energy-consumption memories.

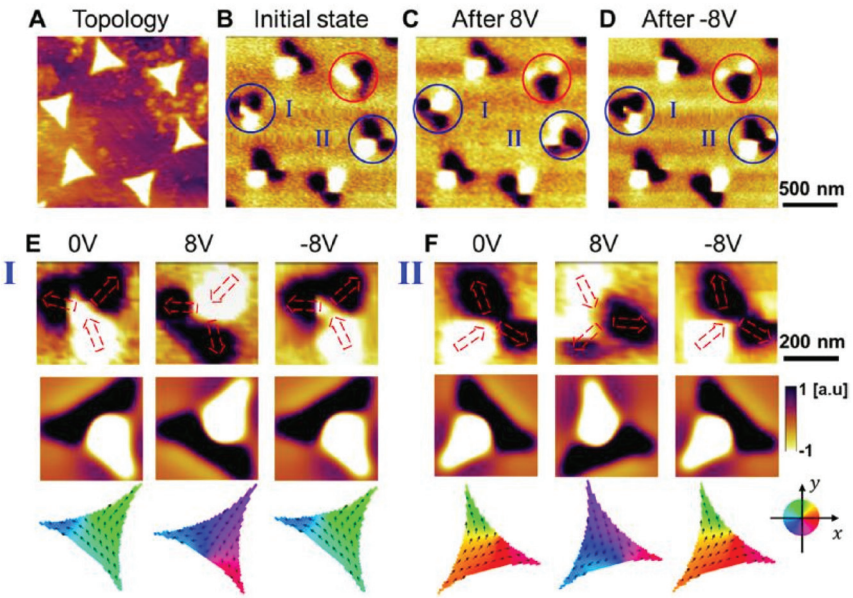

Fig. 16 (A) Atomic force microscopy topology of six Co nanodots on the epitaxial BFO film. (B–D) Magnetic force microscopy images of the six Co nanodots in the initial magnetic state without pretreatment, then upon an electric pulse of +8 V, and then upon a −8 V pulse, respectively. The top rows in (E) and (F) indicate the enlarged magnetic force microscopy images of the blue-marked I and II nanodots, respectively. The red dashed arrows show the average magnetization vectors of the three triangle wings in magnetic force microscopy images. Corresponding to the top row in (E) and (F), the simulated magnetic force microscopy contours and magnetic moment configurations are displayed in the middle and bottom rows, respectively. Adapted with permission from ref. 216. Copyright 2018, American Chemical Society.

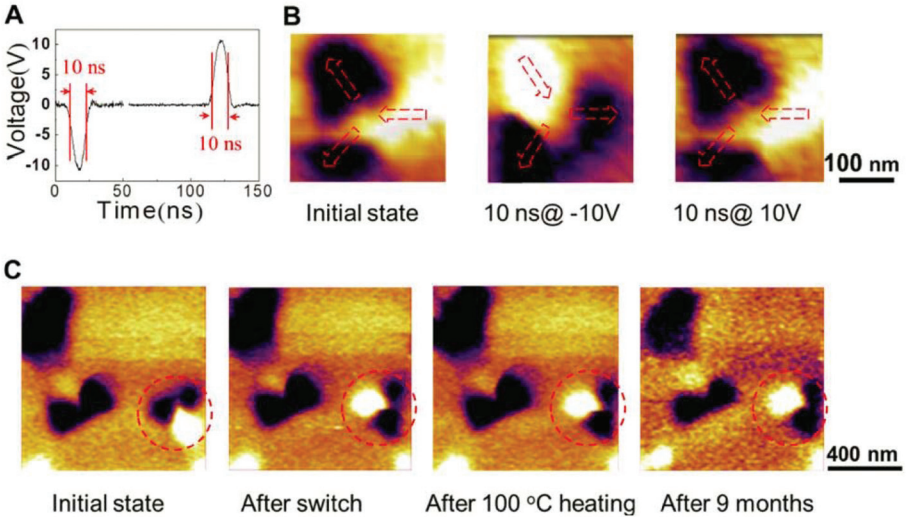

Fig. 17 (A) Wave distribution at the ultrashort electric pulses of 10 ns at ±10 V, which is applied on one chosen Co nanodot on the epitaxial BFO film. (B) Magnetic force microscopy images of the Co nanodot in the initial magnetic state without pretreatment, then upon an electric pulse of +10 V, and then upon a −10 V pulse, respectively. The top row in (B) indicates the simulated magnetic force microscopy images of the blue-marked I and II nanodots, respectively. The dashed red arrows show the average magnetization vectors of the three triangle wings. (C) Serious reads of "written" Co nanodots marked by dashed red cycles: the initial state, switched state after an electric pulse of 8 V at 1.0 ms, switched state after heating at 100 °C in 1 h, and then the switched state after the retention of nine months. Adapted with permission from ref. 216. Copyright 2018, American Chemical Society.

In particular, the phase-field theory provides a way to simulate the phase transition and domain structures in a ferroelectric film.[218] In homogeneous crystals, the thermodynamic potentials can be described by the specific mechanical boundary conditions. However, the ferroelectric film is an inhomogeneous system with a polarization-distinguished domain structure. During the ferroelectric polarization switching in BFO films, the temporal evolution of the polarization vector field can be simulated by the phase-field theory based on the time-dependent Ginzburg–Landau equation[219,220]

$$\frac{\partial \mathrm{P}_i(\mathrm{r},t)}{\partial t} = -L\frac{\delta F}{\delta \mathrm{P}_i(\mathrm{r},t)}, i = 1,2,3, \quad (9)$$

where $\mathbf{P}_i(\mathbf{r},t)$ is the polarization, L is a kinetic coefficient associated with the domain wall mobility. F is the total free energy including Landau energy, elastic energy, electrical energy and gradient energy,[218,221] which can be defined as

$$F = \iiint (f_{\mathrm{Landau}} + f_{\mathrm{elastic}} + f_{\mathrm{electric}} + f_{\mathrm{gradient}})\mathrm{d}V. \quad (10)$$

The time-dependent Ginzburg–Landau equation is solved by a semi-implicit Fourier spectral method at a discreet grid, where the periodic boundary conditions are considered in the film plane. Assuming that the bottom of the BFO film comes in contact with the conductive substrate or buffer layer, the electric potential at the bottom of the BFO film is assumed to be zero, and the electric potential at the top of the BFO film is assumed to be continuous,[222,223] which can be written as

$$\Phi|_{z=0} = 0, \Phi|_{z=h-0} - \Phi|_{z=h+0} = 0, \quad (11)$$

$$\left(\mathrm{P}_z - \varepsilon_0\varepsilon_b\frac{\partial\varphi}{\partial z}\right)\Big|_{z=h-0} + \left(\varepsilon_0\varepsilon_b\frac{\partial\varphi}{\partial z}\right)\Big|_{z=h-0} + \sigma_{\mathrm{surface}} = 0. \quad (12)$$

$\sigma_{\mathrm{surface}}$ indicates the surface charge density at the top of the BFO film, which can be used to describe the electrostatic potential $\phi(r)$

$$-\nabla^2\varphi = \frac{\sigma_{\mathrm{surface}} - \nabla\cdot\mathrm{P}}{\varepsilon_0\varepsilon_r}, \quad (13)$$

where ε_0 and ε_r are the permittivity of vacuum and the BFO film, respectively. The boundary conditions used in the phase-field theory can be gained from the measured thermodynamic parameters in the bulk crystal. By using the determined boundary conditions, the time-dependent ferroelectric polarization in the BFO film at the given strain and temperature will be predicted by the phase-field theory, which can be used to determine the phase transition temperature and domain structure in the BFO film. Moreover, the magnetic free energy of the BFO/ferromagnet heterostructures is composed of several energy contributions,[208] which can be defined as

$$\begin{aligned} F_{\mathrm{tot}} &= E_{\mathrm{exchange}} + E_{\mathrm{magnetocrystalline}} + E_{\mathrm{elastic}} + E_{\mathrm{surface\ and\ interface}} \\ &\quad + E_{\mathrm{exchange\ anisotropy}} + E_{\mathrm{stray\ field}} + E_{\mathrm{external\ field}} \\ &= \int \{A|\nabla m|^2 + f_{\mathrm{ani}}(m) + 0.5(\varepsilon - \varepsilon^0(m))c(\varepsilon - \varepsilon^0(m)) \\ &\quad + K_\mathrm{s}\frac{1-(mn)^2}{d} - \mu_0 M_\mathrm{s}(H_\mathrm{E}m) - 0.5\mu_0 M_\mathrm{s}(H_\mathrm{d}m) \\ &\quad - \mu_0 M_\mathrm{s}(H_{\mathrm{ext}}m)\}\mathrm{d}V, \end{aligned} \quad (14)$$

where A is the exchange stiffness constant, m is the normalized magnetization vector, $f_{ani}(m)$ is the magnetocrystalline anisotropy energy density, ε is the total strain that represents the distortion in a ferromagnetic material, c is the elastic stiffness tensor, and H_E is the exchange anisotropy field induced by the ferromagnetic/antiferromagnetic and ferromagnetic/ferroelectric exchange couplings. In eqn (14), the surface/interfacial anisotropy energy density $K_s\frac{1-(mn)^2}{d}$ is inversely proportional to the film thickness of the ferromagnet. Hence, the surface/interfacial anisotropy will play a key role in a relatively thin film. In order to clarify the changing mechanism of magnetization in the BFO/ferromagnet heterostrucutres, the finite-element multiphysics model, phase-field theory within the microelasticity theory and micromagnetic simulations have been used. The motion of local magnetization $M(r)$ is calculated using the Landau–Lifshitz–Gilbert equation

$$\frac{\partial M}{\partial t} = -\gamma_0(M\times H_{eff}) + \frac{\alpha}{M_S}\left(M\times\frac{\partial M}{\partial t}\right),\quad H_{eff} = (-1/\mu_0)\frac{\delta F_{tot}}{\delta M}, \tag{15}$$

where the effective magnetic field H_{eff} is related to the total magnetic free energy in eqn (14). In eqn (9) and (15), the changing processes of ferroelectric polarization and magnetization in the BFO/ferromagnetic heterostructures can be described theoretically, which has been confirmed by the experimental results. The cooperation between the theoretical simulations and experimental results plays a key role in studying the electrical and magnetic properties of multiferroic heterostructures, which can be reflected by the abovementioned magnetic moment configuration in the Co/BFO/(La,Sr)MnO_3/$SrTiO_3$ heterostructures (Fig. 16).[216] The developed phase-field theory can also be used to investigate the ferroelectric domain structure,[224] charged domain walls[225] and flexoelectric field distribution[226] in BFO film, which are discussed in subsections III. D.1, III.C.2 and III.B.3, respectively.

The antiferromagnetic structure of BFO is canted by the antisymmetric Dzyaloshinskii–Moriya interactions ($-\boldsymbol{D}\cdot\boldsymbol{M}_1\times\boldsymbol{M}_2$) between the nearest magnetic moments $\boldsymbol{M}_1$ and $\boldsymbol{M}_2$, where $\boldsymbol{D}$ is the symmetry-constrained Dzyaloshinskii–Moriya vector.[52] However, antiferromagnetic BFO shows a ferromagnetic characteristic in the heterointerfaces.[30,227] In the $La_{0.7}Sr_{0.3}MnO_3$/BFO heterostructures, the interfacial ferromagnetic states with a moment of $0.6\mu_B$/Fe appear in BFO, which is attributed to the interfacial orbital reconstruction.[30] Guo *et al.* also observed a large net moment of $\sim 2.8\mu_B$/Fe in the (100)-BFO/$La_{0.8}Sr_{0.2}MnO_3$ superlattices.[228] However, no net moment is induced in the (111)-BFO/$La_{0.8}Sr_{0.2}MnO_3$ superlattices.[228] So, the spin canting triggered by the interfacial exchange coupling results in a large net moment in the (100)-oriented case.[228] Moreover, Yin *et al.* demonstrated two interfacial couplings for achieving the net Fe moment at the BFO/LSMO interfaces, where the direct Fe_-–Mn (indirect Fe_+–O_B–MnO) exchange coupling induces a net Fe moment of $0.55\mu_B$ ($-1.07\mu_B$) in the MnO_2/Fe–O_2 (MnO_2/O_2–Fe) model.[227] The interfacial net Fe moment in the MnO_2/Fe–O_2 model with a spin polarization of 100% can also be reversed by applying an electric field, which provides the foundation for developing the BFO/LSMO-based spintronic devices.

The interfacial magnetoelectric coupling (IMEC) is demonstrated in the BFO/LSMO heterostructures by first-principles calculations, where the ferroelectric polarization reversal of BFO can increase or decrease the magnetic moments of LSMO.[136,137] Here, IMEC is proposed in the ferromagnetic/ferroelectric heterostructures,[208,229] where the ferroelectric polarization directions are opposite at two interfaces. The IMEC coefficient is defined as $\alpha \approx \mu_0\Delta M/E_c$,[229] where E_c is the coercive fields of ferroelectric materials, μ_0 is the permeability under vacuum and ΔM is the difference of the magnetic moments at two interfaces. Yin *et al.* found that the tetragonal BFO/LSMO heterostructures show an IMEC of $\alpha \approx 0.221$ G cm kV^{-1} in the *xy*-plane lattice constants ranging from 3.62 to 3.92 Å,[137] which is larger than $\alpha \approx 0.174$ G cm kV^{-1} of the BFO/LSMO superlattices.[136] A stronger IMEC in the BFO/LSMO heterostructures than in its superlattices can be ascribed to the different interfacial Fe–O_{LSMO} covalent and O_{BFO}–La electrovalent bonds in two LaO-type BFO/LSMO heterostructures.

2. Electric field control of magnetic anisotropy by magnetoelectric coupling. Since the electric field can tailor the magnetization reversal in the BFO/ferromagnet heterostructures, the magnetic anisotropy of ferromagnetic materials should be controlled by antiferromagnetic BFO and an electric field.[230,231] You *et al.* demonstrated the [100] easy axis of the $La_{0.7}Sr_{0.3}MnO_3$ layer in $La_{0.7}Sr_{0.3}MnO_3$/BFO bilayers (Fig. 18a), which is different from the [010] easy axis in a pure $La_{0.7}Sr_{0.3}MnO_3$ layer.[50] Here, H_C, M_R and M_S are the coercive field, remnant magnetization and saturation magnetization, respectively. You *et al.* further studied the in-plane angle dependent H_C and M_R/M_S of the $La_{0.7}Sr_{0.3}MnO_3$/BFO heterostructures.[50] The uniaxial magnetic anisotropy is observed in the $La_{0.7}Sr_{0.3}MnO_3$ layer, which is related to the striped ferroelectric domains in BFO (Fig. 18b).[50] The anisotropic striped ferroelectric domains in BFO couple to their antiferromagnetic domains; so they can couple to the subsequent ferromagnetic domains in $La_{0.7}Sr_{0.3}MnO_3$. Consequently, the uniaxial magnetic anisotropy of $La_{0.7}Sr_{0.3}MnO_3$ is tunable by multiferroic BFO with the striped ferroelectric domains.[50]

Since the magnetic anisotropy of BFO/ferromagnet heterostructures can be modulated by the ferroelectric property of BFO, the electric field should modulate the magnetic anisotropy through the electric-field controlled ferroelectric property.[16] In the Co/BFO heterostructures (Fig. 18c), the magnetic easy axis of the Co layer switches from 0° to 45° after +400 kV cm^{-1} poling, which transforms from 45° back to 0° after the −400 kV cm^{-1} poling.[51] Moreover, the magnetic easy axis in the Co layer switches again from 0° to 45° after further +400 kV cm^{-1} poling. Hence, in the Co/BFO heterostructures, the electric field can reversibly switch the magnetic easy axis by 45°.[51]

The tetragonal distortion is demonstrated to induce a perpendicular magnetic anisotropy (PMA) in a cubic

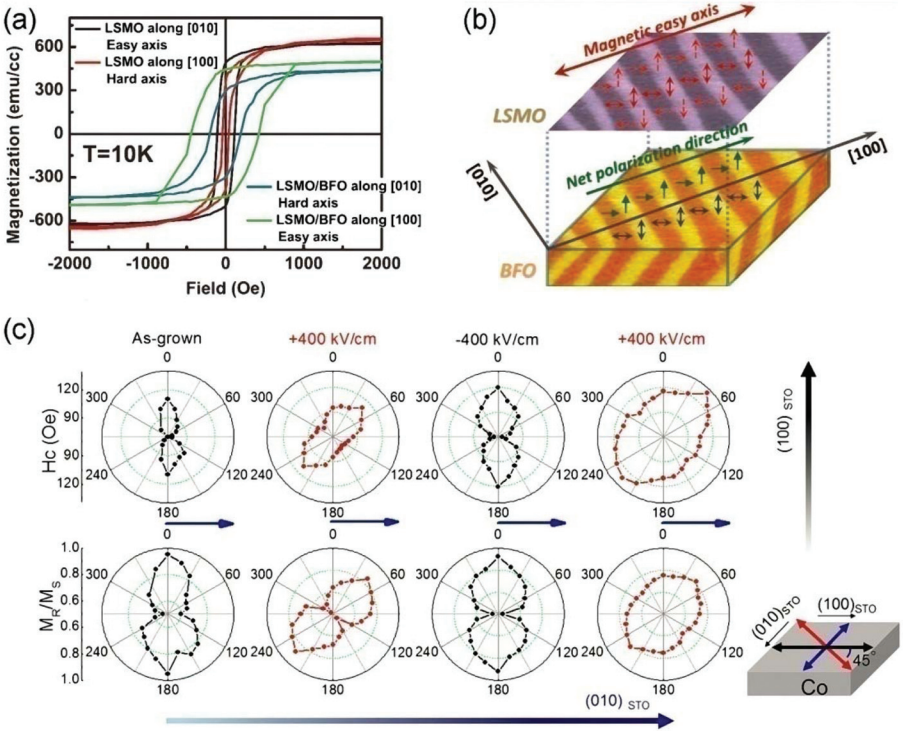

Fig. 18 (a) In-plane M–H curves along the [100] and [010] directions of the $La_{0.7}Sr_{0.3}MnO_3$ single layer and $La_{0.7}Sr_{0.3}MnO_3$/BFO bilayers. (b) Scheme of the ferroelectric polarization induced uniaxial magnetic anisotropy of $La_{0.7}Sr_{0.3}MnO_3$/BFO bilayers. Adapted with permission from ref. 50. Copyright 2010, Wiley. (c) Angle-dependent magnetic coercivity H_C and M_R/M_S of the Co layer in the as-grown Co/BFO heterostructures, after the first +400 kV cm^{-1} poling, after the subsequent −400 kV cm^{-1} poling, and after the second +400 kV cm^{-1} poling. 0° and 90° indicate the (100) and (010) directions of the $SrTiO_3$ substrate (long blue and black arrows), respectively. Adapted with permission from ref. 51. Copyright 2017, American Chemical Society.

ferromagnet.[232,233] Yin *et al.* found that the PMA appears in the entire Fe_4N layer of the tetragonal Fe_4N/BFO heterostructures (Fig. 19a), and is attributed to the interfacial hybridization and tetragonal distortion with different terminations, interfacial atomic positions and ferroelectric polarizations.[45] The influence of ferroelectric polarization on the PMA of Fe_4N mainly lies in the first interfacial atomic layer (Fig. 19b), where PMA turns into the in-plane magnetic anisotropy. The modulation of ferroelectric polarizations on PMA has also been experimentally realized in the BFO/Al_2O_3/Pt/Co/Pt heterostructures.[234] By considering the spin–orbit coupling (SOC),[45,235–237] the total magnetic anisotropy energy (MAE) in the multiferroic heterostructures is defined over different orbital λ values of atom i with the so-called canonical formulation[235,236]

$$\mathrm{MAE}_{i\lambda} = \left[\int^{E_F^{out}} (E - E_F^{in}) n_{i\lambda}^{out}(E)\mathrm{d}E - \int^{E_F^{in}} (E - E_F^{in}) n_{i\lambda}^{in}(E)\mathrm{d}E\right]/a^2, \quad (16)$$

where $n_{i\lambda}^{out}(E)$ and $n_{i\lambda}^{in}(E)$ are the density of states on orbital λ of atom i in the out-of-plane and in-plane magnetization orientations, and a is the in-plane lattice constant. The MAE of atom i can be calculated with λ for each of the orbitals[45,236]

$$\mathrm{MAE}_i = \sum_\lambda \mathrm{MAE}_{i\lambda}, \quad (17)$$

and then the sum of MAE_i over all the atoms produces the total MAE.[236] Based on the atomic layer- and orbital-distinguished MAE results, Yin *et al.* found that the PMA of Fe_4N is preserved by $d_1 = d_{xy} + d_{x^2-y^2}$ and $d_2 = d_{xz} + d_{yz} + d_{z^2}$ orbital oscillations in the unstrained and strained Fe_4N/BFO heterostructures.[46] Moreover, in the tetragonal Fe_4N/BFO heterostructures, the PMA in each Fe_4N atomic layer can be modulated by an electric field, not only the interfacial layers.[47] Such an effective electric-field control of PMA can be attributed to the broken spin screening of the electric field[47,238] in highly spin-polarized Fe_4N.[47,145,239] These results reveal that T-BFO films can be used to stimulate the PMA in ferromagnets. Additionally, another important theory is necessary to calculate the MAE. Based on the second-order perturbation theory, the MAE also can be described by the occupied and unoccupied states, which can be defined as[240,241]

$$\mathrm{MAE} \propto \xi^2 \sum_{o,u} \frac{|\langle\psi_o|L_z|\psi_u\rangle|^2 - |\langle\psi_o|L_x|\psi_u\rangle|^2}{E_u - E_o}, \quad (18)$$

where ξ is the SOC constant, and $E_o(E_u)$ and $\psi_o(\psi_u)$ are the eigenstates and eigenvalues of the occupied (unoccupied) states. In the $Fe_{1-x}Co_x$/MgO structures,[242] the second-order

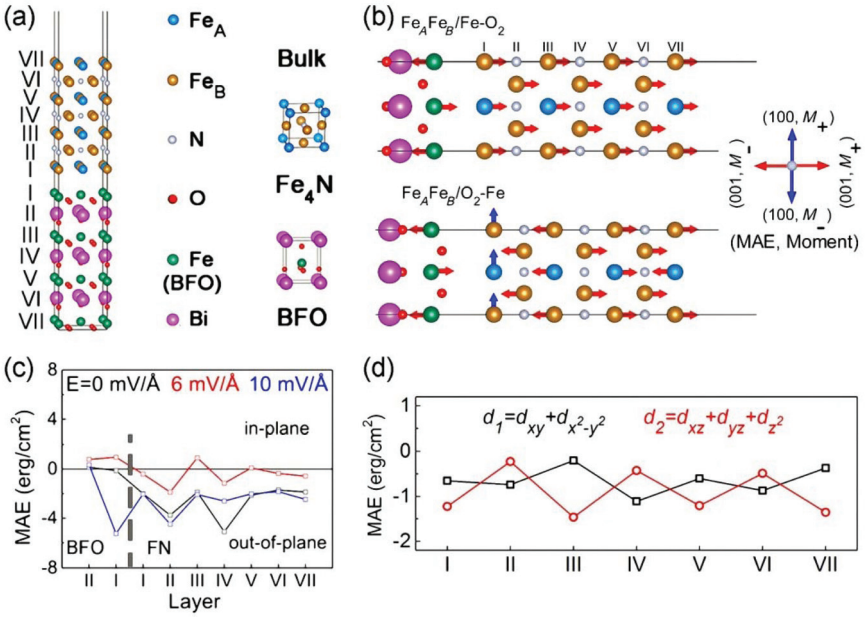

Fig. 19 (a) Structures of the Fe_4N/BFO heterostructures, bulk Fe_4N and BFO. Adapted with permission from ref. 47. Copyright 2017, AIP Publishing. (b) Magnetic order of the Fe_4N/BFO heterostructures with the opposite polarization directions of ferroelectric BFO. M_+(M_-) indicates the magnetic moment with a positive (negative) value. Adapted with permission from ref. 45. Copyright 2016, American Physical Society. (c) Layer-resolved magnetic anisotropy energy of the Fe_4N/BFO heterostructures at different electric fields by GGA+*U*+SOC calculations. The FN label indicates Fe_4N. Adapted with permission from ref. 47. Copyright 2017, AIP Publishing. (d) Orbital-resolved magnetic anisotropy energy oscillation of the Fe_4N layer in the Fe_4N/BFO heterostructures. Adapted with permission from ref. 46. Copyright 2017, American Chemical Society.

perturbation theory qualitatively demonstrates that the MAE of $Fe_{1-x}Co_x$ is highly dependent on the d orbital occupation. The second-order perturbation theory can be used to calculate the MAE of the BFO-based multiferroic heterostructures with the localized d orbitals.

Moreover, the ferroelectric and antiferromagnetic domains of BFO have aroused plenty of fascinating phenomena, such as the domain-dependent photovoltaic effects[188] and domain-interacted electric-field control of magnetism.[216] So, the domain-based research studies should be paid much attention by precisely engineering the domain structures in BFO. Winkler *et al.* clarified that the misfit dislocations at the BFO/substrate interfaces can serve as nucleation sites, which can slow down the domain motion.[243] In 2011, Nelson *et al.* observed the special vortex domain arrays at BFO/$TbScO_3$ interfaces.[244] These phenomena reveal the interfacial effects on the domain structures in the BFO-based heterostructures. Particularly, Chen *et al.* have successfully engineered the domain structure of BFO *via* introducing a dielectric layer to form new interfaces by pulsed laser deposition.[245] Fig. 20 shows the pure 71° domains of BFO transferred into the mixed 71° and 109° ones by inserting a $La_{0.25}Bi_{0.75}FeO_3$ layer.[245] Moreover, the proportion of 109° domains in the BFO/$La_{0.25}Bi_{0.75}FeO_3$/$SrRuO_3$/$DyScO_3$ heterostructures increases with the increase in the $La_{0.25}Bi_{0.75}FeO_3$ layer thickness, which finally turns into pure 109° domains at a thickness of 10 nm. The precise control of 71° and 109° domains also unambiguously confirms that the exchange bias in the BFO/ferromagnet heterostructures comes from 109° domains, but not 71° domains, as shown in Fig. 21.[245] The 180° domains of BFO also favor the exchange bias in the BFO/ferromagnet heterostructures, which has been observed in the $Co_{0.9}Fe_{0.1}$/BFO structures.[246] The realized interfacial modulation of the domain structures of BFO provides a good platform for developing novel domain-based optical, electrical and spintronic devices. Besides, the domain structure of BFO can also be controlled by changing the growth pressure during pulsed laser deposition, where the high background pressure can produce a *z*-directional film and long range ordering of 71° domains.[247] The ferroelectric domains of BFO can also be oriented by temperature in the optical second harmonic generation technique.[248]

Here, we underline a special BFO/electrode interface. Zou *et al.* demonstrated that the charged domain walls by electrical cycling will not lead to polarization fatigue.[249] However, after prolonged cycling, the injected charges move into the BFO/electrode interface, which can pin the domains and cause polarization fatigue.[249] Such a domain-pinned BFO/electrode interface should be avoided in the future. Besides, Chu *et al.* have successfully obtained 1D periodically ferroelectric domain structures in BFO films,[250] which can be ascribed to the in-plane lattice constants of $SrRuO_3$ films constricted by $DyScO_3$ substrates. Jang *et al.* have successfully selected the 109° and 71° ferroelectric domains in BFO by miscutting cubic $SrTiO_3$ substrates, which stimulates the step-flow growth of BFO films with two-variant stripe domains.[251] It can be noted that, except the interfacial effects, strain is another effective tool to control the domain structure in BFO.

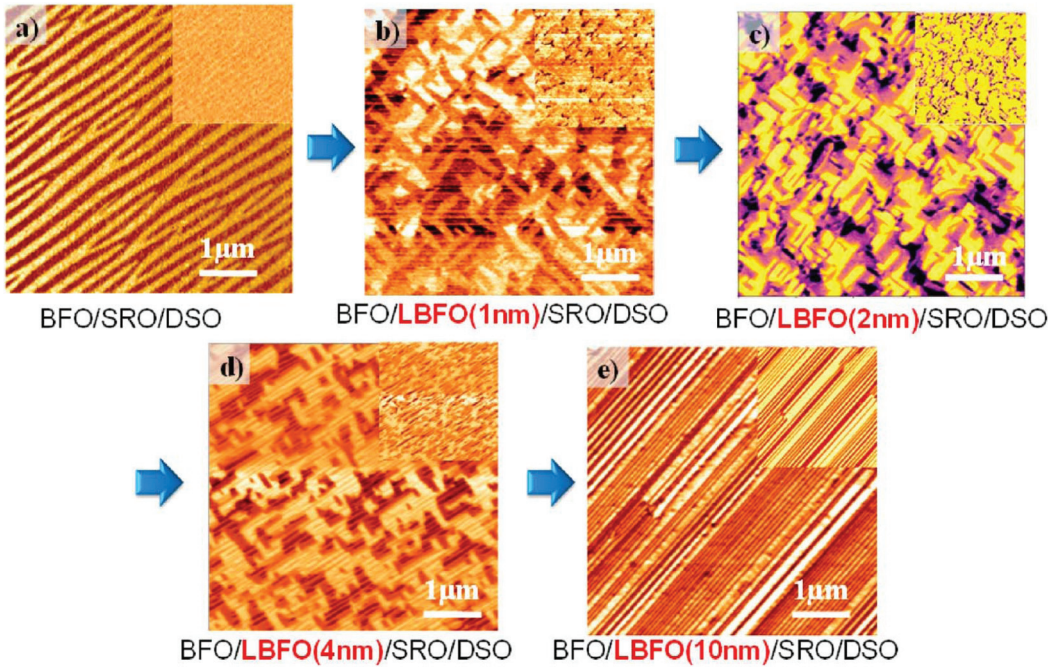

Fig. 20 In-plane and out-of-plane (insets in the top right corner) piezoresponse force microscopy images of (a) BFO/$SrRuO_3$/$DyScO_3$ with pure 71° domains, (b–d) thickness-varied BFO/$La_{0.25}Bi_{0.75}FeO_3$/$SrRuO_3$/$DyScO_3$ heterostructures with mixed 71° and 109° domains, and (e) BFO/$La_{0.25}Bi_{0.75}FeO_3$/$SrRuO_3$/$DyScO_3$ heterostructures with 10 nm thick $La_{0.25}Bi_{0.75}FeO_3$ and pure 109° domains. Adapted with permission from ref. 245. Copyright 2017, American Chemical Society.

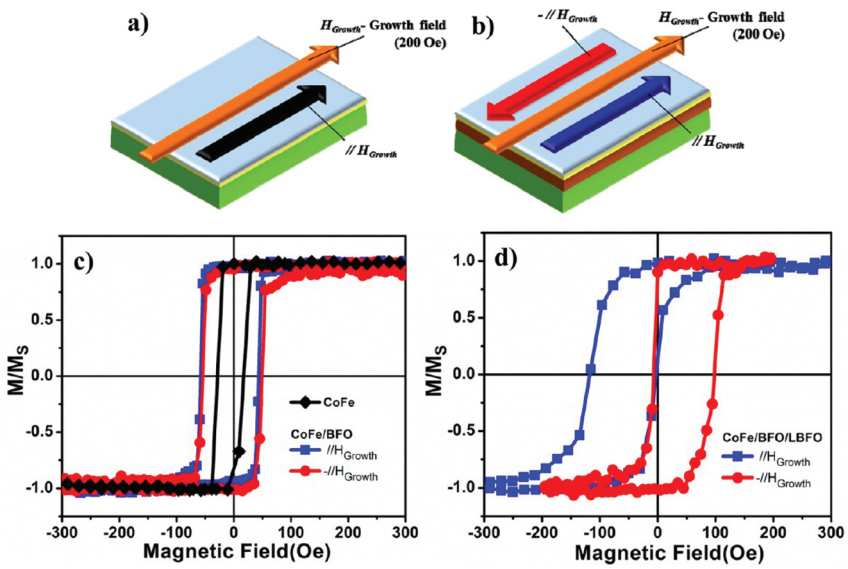

Fig. 21 Diagrams of the applied magnetic field orientation and the used magnetic field in superconducting quantum interference device measurements for (a) Pt/CoFe/$DyScO_3$ and (b) Pt/CoFe/BFO/$DyScO_3$ and Pt/CoFe/BFO/$La_{0.25}Bi_{0.75}FeO_3$/$DyScO_3$. Magnetic properties of (c) Pt/CoFe heterostructures (black loop), CoFe/BFO heterostructures (red and blue loops) with pure 71° domains and (d) CoFe/BFO/$La_{0.25}Bi_{0.75}FeO_3$ with pure 109° domains. Adapted with permission from ref. 245. Copyright 2017, American Chemical Society.

3. Electric field control of magnetic anisotropy by induced strain. Epitaxial BFO films have the ferroelastic property[252] and strain-tunable domain structures,[253] which will contribute to the strain modulation on the electric-field controlled magnetic anisotropy. Here, hard magnetic $CoFe_2O_4$ is taken as an example because of its strain-sensitive magnetic anisotropy. More importantly, $CoFe_2O_4$ can epitaxially grow on perovskite BFO, where $CoFe_2O_4$ nanopillars are embedded in the BFO matrix (*i.e.*, the BFO–$CoFe_2O_4$ nanocomposites). The self-assembled nanostructures can provide a larger interfacial area

between $CoFe_2O_4$ and BFO, which is beneficial for the interfacial magnetoelectric coupling. Zavaliche *et al.* observed two electric-switchable perpendicular magnetic states in the BFO–$CoFe_2O_4$ composites on $SrTiO_3$ substrates due to the magnetoelectric coupling.[150]

In particular, the strain effect on the magnetic anisotropy in the BFO–$CoFe_2O_4$ composites was investigated by depositing the composite films on piezoelectric $Pb(Mg_{1/3}Nb_{2/3})_{0.7}Ti_{0.3}O_3$ (PMN-PT) substrates. Wang *et al.* have fabricated 65BFO-35$CoFe_2O_4$/PMN-PT heterostructures (Fig. 22a and b) by pulsed laser deposition, where the magnetic anisotropy of $CoFe_2O_4$ can be tailored by the electric-field induced strain.[151] As seen in Fig. 22c, the M_R and H_C of $CoFe_2O_4$ decrease (increase) in the out-of-plane (in-plane) direction after electric poling, where the magnetic easy axis turns from the out-of-plane to in-plane directions on applying an electric field.[151] In Fig. 22c, the modulated magnetic anisotropy can be attributed to the electric-field-induced strain in the PMN-PT substrate, where the strain can transfer into the 65BFO-35$CoFe_2O_4$ layer. Therefore, the electric-field induced strain provides a new tool to tailor the magnetic anisotropy of ferromagnets, which can be integrated with the magnetoelectric-coupling-tunable magnetic anisotropy in the BFO/ferromagnet heterostructures. The two kinds of electric-field control of magnetic anisotropy provide a fertile ground for developing BFO-based data storage and multifunctional devices.

The antiferromagnetic vector of BFO epitaxial films is not always perpendicular to its ferroelectric polarizations, which can also be tailored by the substrate strain. Although the epitaxial strain has no obvious impact on the ferroelectric polarization direction of the BFO(110)/$GdScO_3(010)_O$ heterostructures, the antiferromagnetic spin axis of BFO is continuously reoriented from the in-plane direction to the out-of-plane direction by a large epitaxial strain,[254] which is different from the previously reported perpendicular relationship between the polarization direction and antiferromagnetic axis of BFO. The special strain effect on the ferroelectricity and antiferromagnetism of BFO is theoretically clarified by considering the Dzyaloshinskii–Moriya interaction and single-ion anisotropy. The Hamiltonian can be written as

$$H = -\sum_{ij} J_{ij} \mathrm{S}_i \cdot \mathrm{S}_j - \sum_{ij} \mathrm{D}_{ij} \cdot S_i \times S_j - K \sum_i |\mathrm{S}_i \cdot \mathrm{n}_i|^2 + H_0, \quad (19)$$

where $\boldsymbol{S}_i$ is the ith spin vector, J_{ij} is the exchange parameter, $\boldsymbol{D}_{ij}$ is the Dzyaloshinskii–Moriya interaction vector, K is the single-ion anisotropy constant and H_0 represents all other interactions. Chen *et al.* performed the density functional theory calculations on BFO cubic perovskite units with three axes of [110], [001] and [1$\bar{1}$0] by revising the Hamiltonian.[254] It is found that the antiferromagnetic spin axis in BFO is dominated by the Dzyaloshinskii–Moriya interaction at small strains, which agrees well with the previously reported perpendicular relationship between the polarization direction and antiferromagnetic vector in BFO. However, at a large strain, the single-ion anisotropy of BFO increases dramatically until it is comparable to the Dzyaloshinskii–Moriya interaction, which results in the antiferromagnetic vector reorientation in BFO without changing the ferroelectric polarization. Moreover, the

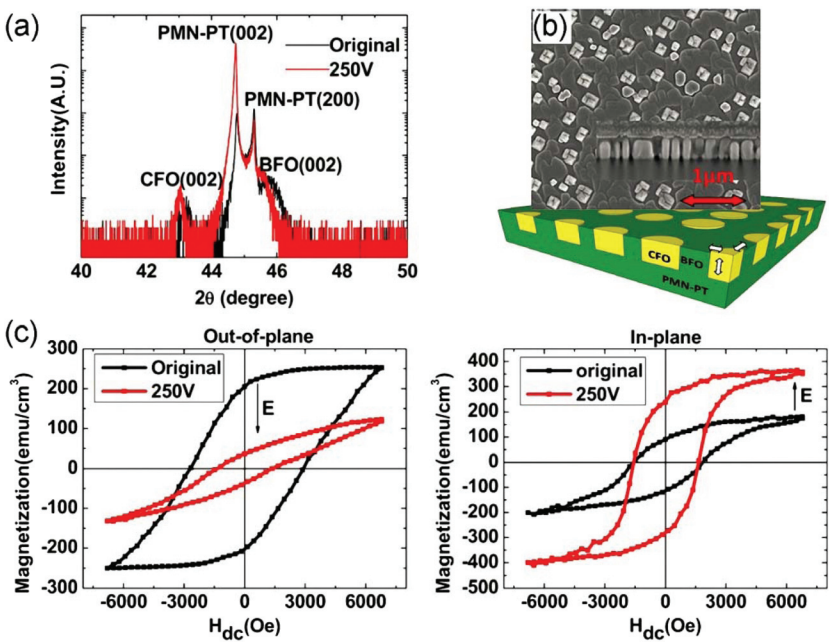

Fig. 22 (a) X-ray diffraction line scan of 65BFO-35$CoFe_2O_4$ on PMN-PT before and after poling. (b) Scanning electron microscopy image of the 65BFO-35$CoFe_2O_4$ layer and the scheme of the strain conditions during the poling process in the 65BFO-35$CoFe_2O_4$/PMN-PT structure. (c) Magnetic hysteresis loops of the 65BFO-35$CoFe_2O_4$/PMN-PT structure before and after electric poling in the out-of-plane and in-plane directions, respectively. Adapted with permission from ref. 151. Copyright 2011, AIP Publishing.

strain-induced antiferromagnetic vector reorientation of BFO can further tailor the magnetic anisotropy of the ferromagnetic $Co_{0.9}Fe_{0.1}$ layer.[254]

Moreover, Bordacs *et al.* observed that the cycloidal spin structure of a bulk BFO crystal with a ferroelectric monodomain can be rearranged under a magnetic field by small-angle neutron scattering.[255] The cycloid propagation vectors are rotatable when the applied magnetic field with a pinning threshold value above 5 T is perpendicular to the rhombohedral polar axis, which reveals a new coupling between the magnetic anisotropy and ferroelectric polarization of BFO.[255] Fishman used the so-called "canonical" model to explain the magnetic field induced rearrangement of cycloidal domains in BFO, where the Hamiltonian is written as

$$\begin{aligned} H = & -\boldsymbol{J}_1 \sum_{\langle i,j \rangle} \mathrm{S}_i \cdot \mathrm{S}_j - \boldsymbol{J}_2 \sum_{\langle i,j \rangle'} \mathrm{S}_i \cdot \mathrm{S}_j \\ & + \boldsymbol{D}_1 \sum_{\langle i,j \rangle} (\mathrm{z}' \times \mathrm{e}_{i,j}/a) \cdot (\mathrm{S}_i \times \mathrm{S}_j) \\ & + \boldsymbol{D}_2 \sum_{\langle i,j \rangle} (-1)^{h_i} \mathrm{z}' \cdot (\mathrm{S}_i \times \mathrm{S}_j) \\ & - \boldsymbol{K}_1 \sum_i (\mathrm{z}' \cdot \mathrm{S}_i)^2 - 2\mu_B \boldsymbol{B} \sum_i \mathrm{m} \cdot \mathrm{S}_i, \end{aligned} \tag{20}$$

where the first Dzyaloshinskii–Moriya interaction $\boldsymbol{D}_1$ indicates the cycloidal wavelength and the second Dzyaloshinskii–Moriya interaction $\boldsymbol{D}_2$ generates a small tilt of the spins out of the $\boldsymbol{x}'$–$\boldsymbol{z}'$ plane.[256] The "canonical" model was further augmented by the threefold anisotropy and magnetoelastic energy, which successfully deduced the critical magnetic field to rotate the cycloidal domains of BFO.[256]

The piezoelectric materials with transformable electrical and mechanical energy are essential for the strain tunable magnetic anisotropy in BFO-based heterostructures. Meanwhile, the BFO-based composites can also efficiently switch the ferroelectric and ferroelastic domains by an electric field. Narayan *et al.* found a large electric field induced strain of 1.3% in BFO–$PbTiO_3$–$LaFeO_3$ ferroelectric composites, which is larger than that in polycrystalline piezoelectric ceramics.[257] Moreover, Narayan *et al.* have also revealed that the electric field induced strain can be affected by four factors, including a large spontaneous lattice strain in the piezoelectric phase, a domain miniaturization, a low-symmetric ferroelectric phase and a high reverse switching of non-180° domains.[257] The design strategy can be utilized in future ferroelectric piezoelectrics for obtaining a large electric field induced strain.

Additionally, BFO can tailor not only the magnetic anisotropy, but also the electronic anisotropy of the ferromagnets in the BFO/ferromagnet heterostructures. In the $La_{0.7}Sr_{0.3}MnO_3$/BFO heterostructures,[258] a transition from a metal to an insulator appears in $[001]_o$ oriented LSMO at 301.3 K. However, the $[1{-}10]_o$ directional transport shows an insulator-like characteristic at low temperatures. So, the in-plane anisotropic resistance appears in LSMO, which can reach 800% at low temperatures. In the BFO/ferromagnet heterostructures, the large anisotropic resistivity can be ascribed to the different strains in LSMO at different lattice orientations, which is tunable by the ferroelastic domain walls of BFO. Based on the ferroelectric, antiferromagnetic and ferroelastic characteristics of BFO, both the magnetic and electronic anisotropy of the ferromagnets can be tailored in the BFO-based heterostructures, which provides a platform for designing multifunctional devices.

However, the electromechanical coupling between the electric polarization and strain gradient in the BFO-based heterostructures is limited to utilizing not only the electric field induced strain due to the piezoelectric effects, but also the flexoelectricity,[259,260] which enables the mechanical control of ferroelectric polarization without an electric bias. In particular, Park *et al.* have successfully induced a flexoelectric field by moving a scanning probe microscope tip, which can selectively switch the polarization of multidomain structures of BFO, as shown in Fig. 23.[226] Moreover, based on the induced flexoelectric field, the motion of the scanning probe microscope tip can not only stimulate the 180° ferroelectric domain switching (Fig. 23) but also the 71° ferroelastic domain switching, where the ferroelectric or ferroelastic switching is dependent on the tip scanning direction. The novel flexoelectricity effects of multidomain BFO provides new insight for developing electromechanical devices. Besides, the disclinations of BFO can be used to generate a strain gradient. Tang *et al.* have stimulated the inhomogeneous strain with a linear gradient of 10^6 per meter in $LaAlO_3$/BFO/$LaAlO_3$ nanostructures,[261] which resulted in a large built-in electric field and improved solar absorption. Such strain engineering in the BFO-based heterostructures can be utilized to design photoelectric devices.

C. Resistance switching

The RS characteristics in BFO-based heterostructures have been widely investigated due to their potential applications in data storage and memory. In BFO-based FTJs, the RS properties can be generated by conductive filaments, which will be discussed in subsection III.C.1 including the contribution of oxygen vacancies and memristive switching. In subsection III.C.2, the RS triggered by the ferroelectric polarization reversal and charged domain walls is reviewed, such as the memristive behavior and phase transition in the BFO-based FTJs. Moreover, the four resistance states and photoresponse in BFO-based MFTJs are theoretically[262] and experimentally[57,152] illustrated in subsection III.C.3. Besides, the resistance switching in the semiconductor/BFO/metal junctions has been illustrated in subsection III.A.4, along with different photovoltaic responses and conduction modes in the junctions at low and high resistance states.

1. Conductive filament-related resistance switching in metal/$BiFeO_3$/metal sandwiches. In the metal/BFO/metal sandwich structures, RS can be modulated by the conductive filaments, which are commonly associated with the oxygen vacancies in the insulating BFO region.[54,129] In Ag/$Bi_{0.95}La_{0.05}FeO_3$/Pt sandwich structures,[129] the temperature-dependent resistances show a metallic (semiconducting) characteristic in the LRS (HRS). Moreover, the LRS is weakly

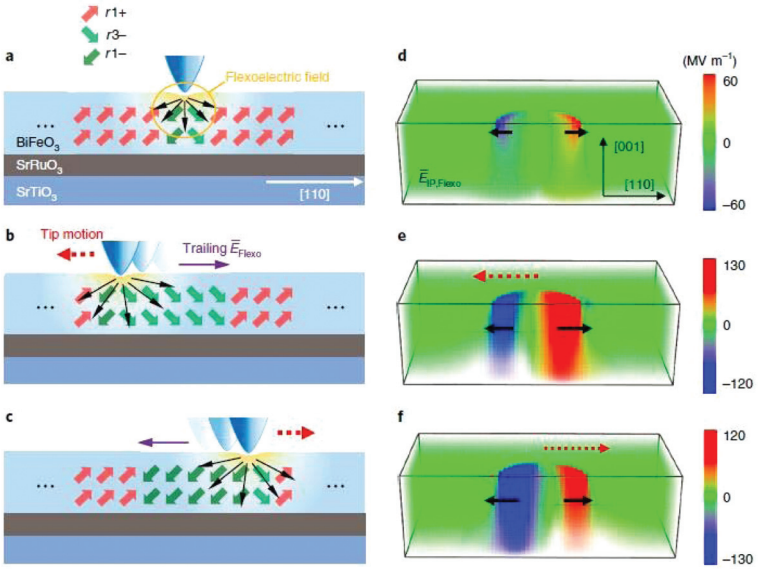

Fig. 23 Schematics of the flexoelectric field and related polarization switching in the BFO film under the scanning probe (a) in static contact, and (b and c) tracing the moved tip in [$\bar{1}\bar{1}$0] and [110] directions, respectively. Phase-field simulations of the in-plane flexoelectric field distribution of the BFO film under the scanning probe (d) in static contact, and (e and f) tracing the moved tip in [$\bar{1}\bar{1}$0] and [110] directions. Adapted with permission from ref. 226. Copyright 2018, Nature Publishing Group.

dependent on the device area, which reveals the conductive filament dominated RS in the Ag/$Bi_{0.95}La_{0.05}FeO_3$/Pt structures. In particular, the nonpolar RS in the Pt/$BiFe_{1-x}Mn_xO_3$/Pt structures[54] was ascribed to the oxygen vacancy induced conductive filaments, followed by the changed valence states of Fe cations. In Fig. 24a, the ionized oxygen vacancies move towards the cathode and capture the injected electrons in the cathode. Then, the conducting state of the cathode extends to the anode (Fig. 24b), where the conductive path forms.[54] In particular, in Fig. 24c, a negative voltage benefits the release of the electrons from the neutral oxygen vacancies with the changed valence states of Fe ions, which can damage the conductive filaments and result in the bipolar RS.[54] The unipolar RS is attributed to the thermally assisted ionization of oxygen vacancies (Fig. 24d), which randomly appears in the $BiFe_{1-x}Mn$ films.[54] Overall, the conductive filaments in the insulating BFO region can switch the structure of the LRS, while the conductive filaments damaged by the reversal voltages make the structure return to the HRS. The conductive filaments will remarkably decrease the effective areas in the top and bottom electrodes, which can damage the ferroelectric hysteresis loops. Meanwhile, the conductive filament related RS in the BFO-based heterostrutures can be ascribed to the local redox reaction and valence changes of cations, and much attention should be paid to the reliability of such a device, including the retention and endurance.

The conductive filaments formed by the oxygen vacancies can also be related to the grain boundaries in undoped polycrystalline BFO. Based on the density functional theory and Monte Carlo simulations, the uniformly distributed oxygen vacancies in polycrystalline BFO can be pushed into the grain boundaries by the voltage.[263] The hopping conduction barriers

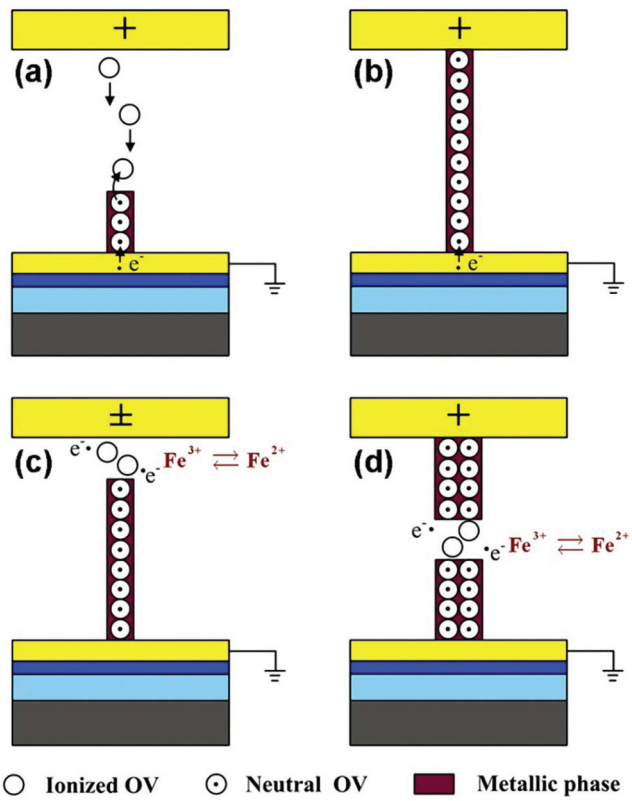

Fig. 24 Diagram of the nonpolar RS mechanism of the Pt/$BiFe_{1-x}Mn_xO_3$/Pt devices at the (a and b) forming process, (c) bipolar RS and (d) unique RS. Adapted with permission from ref. 54. Copyright 2012, AIP Publishing.

formed by the oxygen vacancies at the grain boundaries can be eliminated by a critical SET voltage. Moreover, in the reversal part of the cycle, the grain boundaries also have nonzero conductivity because of the RESET voltage induced oxygen vacancy redistribution.[263] So, the grain boundaries can serve as 2D nanovaristors in polycrystalline BFO under an electric field, which has been confirmed by experimental results.[263] The nanovaristor induced by grain boundaries opens a new way to investigate the memristive switching of the polycrystalline oxide materials. Based on the Miller–Abrahams theory, the rate ν of carrier hopping from one localized oxygen vacancy A to another localized oxygen vacancy B can be written as[263]

$$\nu_{A\to B} = \begin{cases} \nu_0 \exp(-2r/r_0) \exp\left(-\dfrac{E_B - E_A}{kT}\right), \Delta E > 0 \\ \nu_0 \exp(-2r/r_0), \Delta E \le 0 \end{cases}, \quad (21)$$

where ν_0 is the attempt hopping frequency, r is the distance between the vacancies, r_0 is the spatial extent of the localized oxygen vacancies, and E_A (E_B) is the energy level at the localized oxygen vacancies. It is found that the hopping conduction is modulated by the oxygen vacancy position and its energy level. Besides, Du *et al.* have observed that the electric field can drive the hopping transport of charged oxygen vacancies in BFO, which results in the RS.[264]

Here, three typical conduction mechanisms are considered in the BFO film.[188] The first one is the interfacial Schottky emission, where the current density J can be written as

$$J \propto T^2 \exp\left[\frac{1}{k_B T}\left(\frac{q^3}{4\pi\varepsilon_0 K}E\right)^{0.5}\right], \quad (22)$$

where q, K, T and E are the charge of carriers, dielectric constant, temperature and external electric field, respectively. So, the Schottky emission can be determined from a linear relationship between $\ln(J)$ and $E^{0.5}$. The second mechanism is the space-charge-limited conduction of bulk BFO, which can be divided into three cases by the relationship between the current density J and voltage V,[188] including (1) the partially filled shallow traps with a linear Ohmic behavior $J \propto V$, (2) the completely filled shallow traps but partially filled deep traps with $J \propto V^n$, $n > 2$, and (3) the nearly filled deep traps with $J \propto V^2$. The third mechanism is the bulk-limited Poole–Frenkel emission, which can be examined using the linear relationship between $\ln(J/E)$ and $E^{0.5}$ as

$$\frac{J}{E} \propto \exp\left[\frac{1}{k_B T}\left(\frac{q^3}{\pi\varepsilon_0 K}E\right)^{0.5}\right]. \quad (23)$$

The three conduction mechanisms can be used in the conduction analyses of the BFO-based heterostructures.

2. Polarization-modulated RS and memristive behavior in $BiFeO_3$-based ferroelectric tunnel junctions. Compared with the conductive filament related RS with chemical alternation, the reversal of ferroelectric polarization is much stable, which can effectively tailor the RS in the BFO-based FTJs. In Fig. 25b, the bipolar RS appears in both downward and upward polarization states of the Au/BFO/$SrRuO_3$ FTJs, where the voltage sign for the HRS (LRS) in the downward polarization state is opposite to that in the upward polarization state.[130] Such a polarization regulated RS can be attributed to the polarization induced barrier change by the interfacial band bending. In Fig. 25a, the depolarization field towards $SrRuO_3$ accumulates the electrons at the BFO/$SrRuO_3$ interface, which can reduce the depletion width and barrier height. Meanwhile, the negative polarization field widens the depletion region and enlarges the barrier height/width at the Au/BFO interface. In the Au/BFO/$SrRuO_3$ junctions, the asymmetric barrier height/width can result in a positive diode performance, showing a positive-bias-read LRS (Fig. 25b). Similarly, as the depolarization field points towards the Au layer, a reversed diode behavior appears, showing a negative-bias-read LRS (Fig. 25b). Moreover, since the oxygen vacancies exist, the BFO film is always treated as an n-type semiconductor. In the metal/n-type semiconductor/metal junctions, the net built-in potential ϕ'_{bi} is defined as

$$\phi'_{bi} = \phi_{bi} + \Delta\phi^P_{bi} = \phi_{bi} \pm \frac{P\delta}{\varepsilon_0\varepsilon_s}, \quad (24)$$

where ϕ_{bi} is the built-in potential without the polarization charges, $\Delta\phi^P_{bi}$ is the polarization induced change of the built-in potential, P is the ferroelectric polarization, ε_0 is the permittivity of free space, ε_s is the low-frequency dielectric constant, and δ is the width between the polarization surface charge and physical interface with electrodes.[130] It is obvious that the built-in potential can be increased or decreased by switching the ferroelectric polarization, which stimulates the distinct LRS and HRS of the junctions. Meanwhile, the magnitude of ferroelectric polarization can also affect the built-in potential and resistances of the junctions. Therefore, it is an effective tool to tailor the RS by tailoring the ferroelectric polarization in the junctions. Besides, the RS of the multidomain BFO-based heterostructures can be modulated by not only the ferroelectric polarization inside the domains, but also the accumulated oxygen vacancies at the domain walls.[265] The oxygen vacancy effects on the RS of the BFO-based heterostructures should be seriously investigated in the future.

In particular, the semiconductors can also be used to modulate the barrier and RS characteristics of FTJs. In Fig. 25c and d, the Nb:$SrTiO_3$/$Sm_{0.1}Bi_{0.9}FeO_3$/Pt FTJs show the HRS and LRS at the downward and upward polarization states, respectively.[37] In the inset of Fig. 25d, the *I–V* curve in the LRS shows a parabolic shape, which is in good agreement with the direct tunneling theory by the WKB approximation in eqn (4).[204] However, the *I–V* curve in the HRS can be described by Schottky thermionic emission, as illustrated by eqn (6). Therefore, the RS in the Nb:$SrTiO_3$/$Sm_{0.1}Bi_{0.9}FeO_3$/Pt FTJs can be attributed to different conduction modes at the opposite ferroelectric polarizations.[37] Besides, the polarization-induced RS can be further tuned by the illumination owing to the photovoltaic effect of BFO (Fig. 12e),[37,266,267] which can produce multiple resistance states.[268] Meanwhile, the photo-

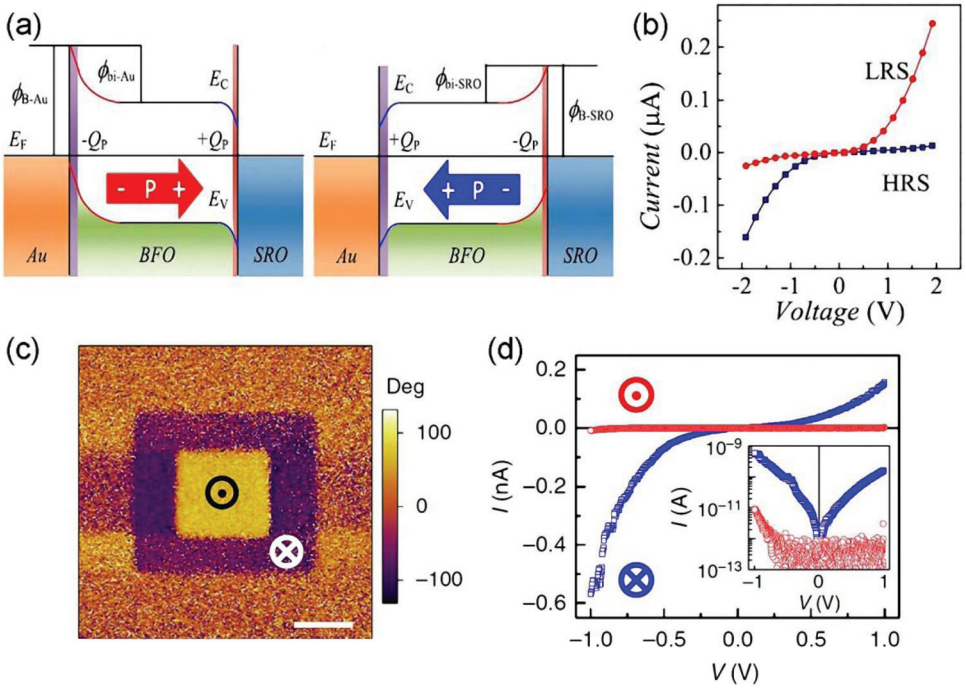

Fig. 25 (a) Schematic energy band structure and (b) rectifying *I*–*V* curves of the Au/BFO/$SrRuO_3$ FTJs in the downward and upward polarization states, respectively. Adapted with permission from ref. 130. Copyright 2014, AIP Publishing. (c) Phase image of square domains and (d) local *I*–*V* curves with the downward (purple in (c) and blue in (d)) and upward (yellow in (c) and red in (d)) polarization states of Nb:$SrTiO_3$/$Sm_{0.1}Bi_{0.9}FeO_3$/Pt FTJs, which correspond to the structure in Fig. 12(a). Adapted with permission from ref. 37. Copyright 2016, Nature Publishing Group.

voltaic effect can also be improved by RS effects in the BFO-based heterostructures.[269] Additionally, Rana *et al.* have found that the ferroelectric polarization tunable RS is dependent on the thickness and lateral length in the BFO/$La_{0.67}Sr_{0.33}MnO_3$ heterostructures.[270] Besides, Cao *et al.* have utilized a radially symmetric electric field to modulate the resistive switching in the BFO/$La_{0.7}Sr_{0.3}MnO_3$ heterostructures, where the polarization reorientation along the radially symmetric electric field results in the polar discontinuity and resultant RS.[271]

Moreover, RS can be induced by not only reversing the ferroelectric polarization in the BFO-based heterostructures, but also the charged ferroelectric domain wall. Generally, the domain walls are always charge-neutral to minimize the electrostatic energy, where a small variation of conductivity can also be induced by the trapped electrons in domain walls[272] and thermal activation,[192,273–276] while, the strongly charged domain walls can be electrically stimulated by gathering the free charges, which provides a new way to induce the large conductance[277] and RS.[225] In the BFO/$La_{2/3}Sr_{1/3}MnO_3$ heterostructures, the applied voltage can write and erase the strongly charged 71° domain walls (Fig. 26), which is identified by the experimental measurements and theoretical calculations. Moreover, the bias-tunable charged domain walls in the BFO/$La_{2/3}Sr_{1/3}MnO_3$ heterostructures can induce the "on" and "off" conductivity states (Fig. 27), which is different from the bias-induced polarization reversal.[225] Besides, in topologically confined BFO nanoislands, the conductivity of charged domain walls in BFO is changed by three orders of magnitude by switching the ferroelectric polarization, as observed by Ma *et al.*[277]

Particularly, the initial R-phase BFO in the BFO/$La_{2/3}Sr_{1/3}MnO_3$ heterostructures can turn into the T phase (Fig. 26h) at the locally charged domain wall boundaries,[225] which provides the possible phase transition effects on the RS of the BFO-based heterostructures.[225,278] Afterwards, the relationship between the phase transition and RS is clearly demonstrated in the Pt/BFO/$LaNiO_3$/$LaAlO_3$ heterostructures.[61] In Fig. 28a and b, the saturation ferroelectric polarization of the epitaxial BFO films is accompanied by the transition from the R–T mixed phase to pure T-phase. In particular, an intermediate resistance state at a voltage of 4.5 V appears during the phase transition (Fig. 28c), where the polarized R–T-mixed phase of BFO at 4.5 V (Fig. 28d) is different from the original R–T-mixed phase (*i.e.*, 0 V) and the polarized pure T-phase (*i.e.*, 5 V).[61] Consequently, multiple resistance states are observed in the Pt/BFO/$LaNiO_3$ FTJs because of the phase transition,[61] which suggests the possibility of phase transition induced RS in other BFO-based FTJs.

This indicates that both ferroelectric polarization and phase transition are crucial for RS in the BFO-based heterostructures; so it is necessary to modulate these two aspects in experiments. Chen *et al.* proposed a systematic method to engineer the ferroelectric ordered T–R phase boundaries in BFO by writing the trajectories of a biased atomic force microscope tip.[279] The fast-scanning axis causes the polarization change of the mixed-phase stripes, and the slow-scanning axis

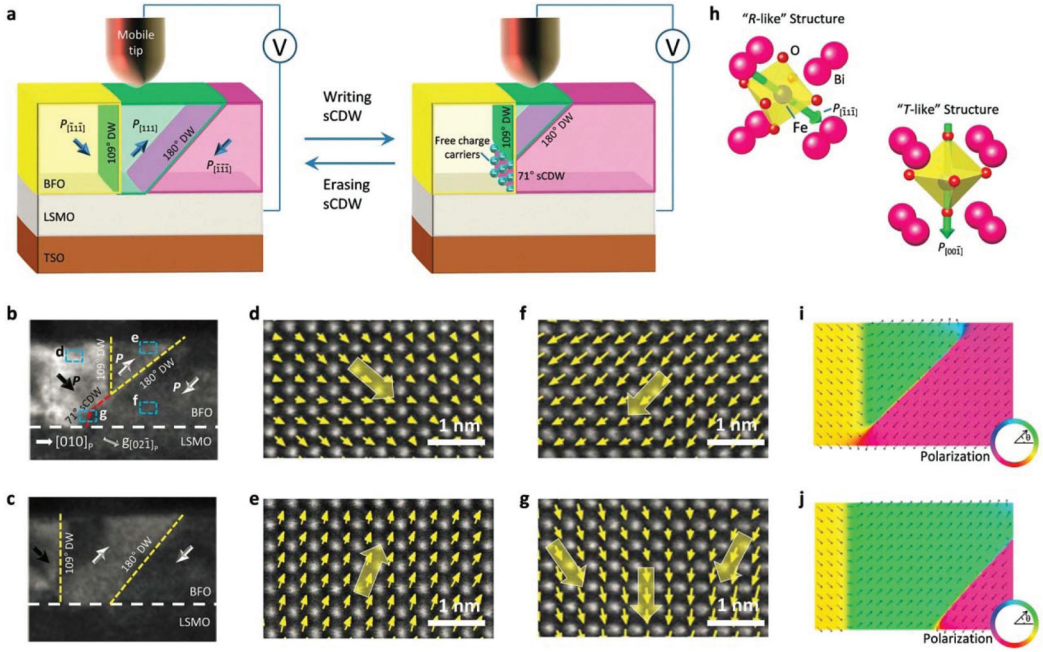

Fig. 26 (a) Experimental setup diagrams for writing and erasing the strongly charged domain walls of the BFO/$La_{2/3}Sr_{1/3}MnO_3$/$TbScO_3$ structures. (b and c) Cross-sectional dark-field transmission electron microscopy image of the BFO/$La_{2/3}Sr_{1/3}MnO_3$/$TbScO_3$ structures with and without 71° strongly charged domain walls, respectively. (d–g) High-angle annular dark-field scanning transmission electron microscopy images of the four rectangle-marked regions in (b). The yellow arrows represent the ferroelectric polarization direction. (h) Models of the R-phase domains and the strongly charged T-phase domain walls. The green arrows indicate the ferroelectric polarization direction. (i and j) Phase-field simulation of the polarization distribution in the BFO film with and without the strongly charged domain walls. The BFO layer thickness is 20 nm in (b) and (c), and then the thickness of simulated BFO in (i) and (j) is 19 nm. Adapted with permission from ref. 225. Copyright 2016, Wiley.

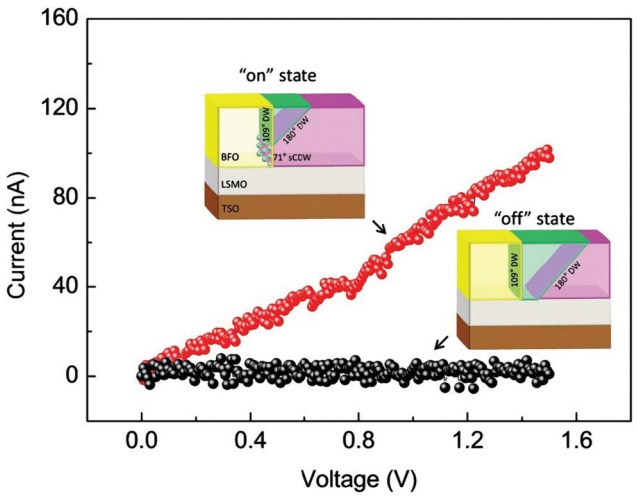

Fig. 27 *I–V* curves of the BFO/$La_{2/3}Sr_{1/3}MnO_3$/$TbScO_3$ structures by considering the "on" state with the strongly charged domain walls and the "off" state without the strongly charged domain walls. During the measurements, there is no sign of domain wall motion. Adapted with permission from ref. 225. Copyright 2016, Wiley.

modulates the ordered domains of T-phase BFO.[279] Moreover, the morphotropic phase boundary has been detected in $BiMnO_3$–BFO–$PbTiO_3$ composites, where the ferromagnetic and ferroelectric orders can be tailored by the polymorphs.[280] These results suggest that the phase boundary has an obvious influence on the magnetic and electrical properties of the BFO-based heterostructures, which may be emphasized in the future.

Particularly, BFO shows the ultrafast polarization dynamics.[281] The ferroelectric polarization tunable RS of the BFO-based heterojunctions can be implanted into the interfacial barrier, which provides the opportunity for continuously tunable RS behaviors, *i.e.*, memristive behaviors.[282] In the Pt/Co/BFO/$Ca_{0.96}Ce_{0.04}MnO_3$ FTJs, the typical resistance hysteresis as a function of writing voltage pulses is shown in Fig. 29a, where the RS OFF/ON ratio reaches 10 000.[55] In particular, in Fig. 29a, the multiple hysteresis loops show an evident dependence on the maximum writing voltage pulse, where different intermediate states can be stabilized in cycles 2–5. Meanwhile, the Pt/Co/BFO/$Ca_{0.96}Ce_{0.04}MnO_3$ FTJs show a good retention property between the ON, OFF and intermediate resistance states (Fig. 29c) and anti-fatigue characteristics (Fig. 29d).[55] The memristive behavior, excellent retention and anti-fatigue properties of the BFO-based FTJs can be used in nonvolatile ferroelectric memristors,[282] compact sequential logics[283] and synapse-like networks,[284] laying a fertile ground for designing multifunctional devices (please see section IV).

3. Four resistance states in $BiFeO_3$-based multiferroic tunnel junctions. MFTJs (*i.e.*, FTJs with two ferromagnetic electrodes) have been widely investigated theoretically[262,285] and experimentally[57,152,286,287] due to their four resistance states,

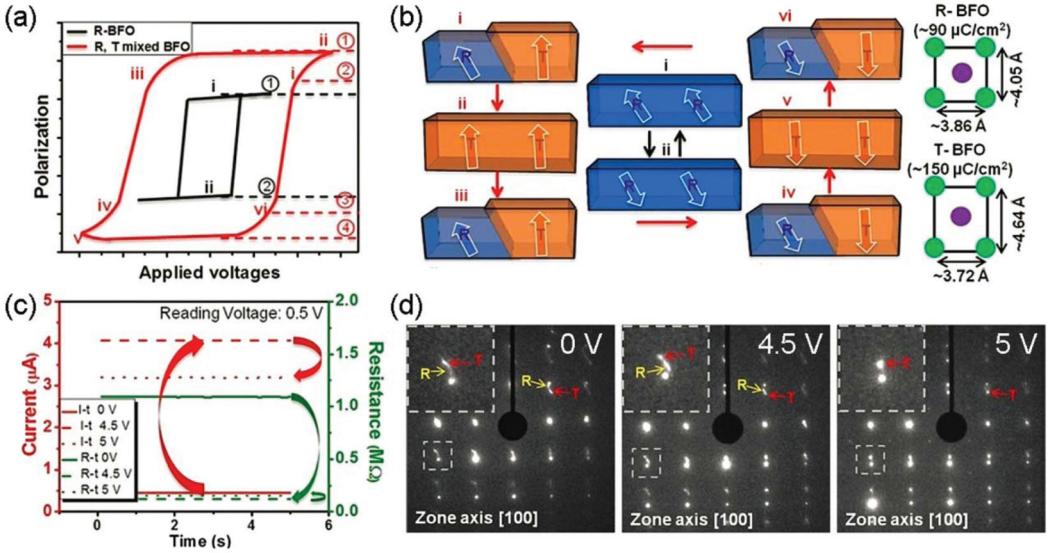

Fig. 28 (a) Schematic hysteresis loop and (b) phase transition between R-BFO and mixed phases with possible multiple states. (c) Current and resistive switching and (d) selected area electron diffraction patterns of the mixed BFO phases under different voltage pulses. Adapted with permission from ref. 61. Copyright 2017, Elsevier.

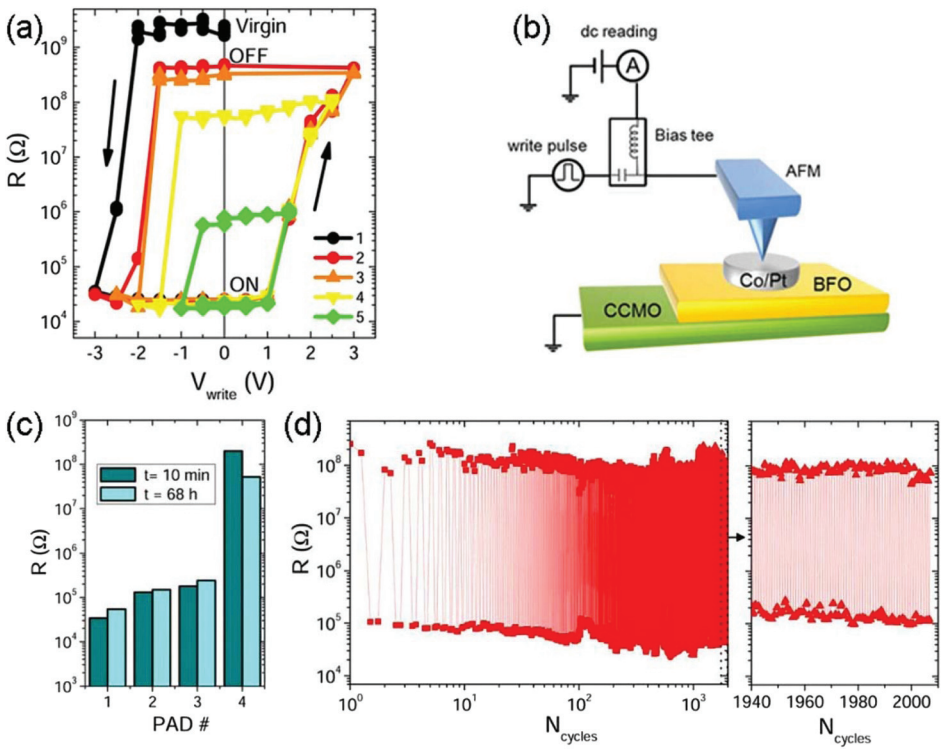

Fig. 29 (a) Resistances as a function of write voltage pulses and (b) the measurement setup of the Pt/Co/BFO/$Ca_{0.96}Ce_{0.04}MnO_3$ FTJs. Cycles 1 and 2(3) correspond to ON and OFF states, respectively. Cycles 4 and 5 indicate minor loops with the intermediate resistance states. (c and d) The retention and fatigue tests of the Pt/Co/BFO/$Ca_{0.96}Ce_{0.04}MnO_3$ FTJs. Adapted with permission from ref. 55. Copyright 2013, American Chemical Society.

which can be attributed to the reversal of ferroelectric polarization of the ferroelectric interlayer and the relatively (anti)parallel magnetization configurations of two ferromagnetic electrodes. Ju *et al.* theoretically investigated the TMR and TER of the BFO-based junctions,[262] which stimulates the following experiments. By using the transfer matrix method, Ju *et al.*

obtained the parallel conductance $G^{(0)}$ and antiparallel conductance $G^{(0)}$ as

$$G^{(0)} = G_{\mathrm{I}}^{(0)} + G_{\mathrm{II}}^{(0)} = \frac{2e^2}{\pi^2\hbar d}\left\{\frac{16k_{\uparrow}^{\mathrm{L}}k_{\uparrow}^{\mathrm{R}}k_{\uparrow}^2e^{-2k_{\uparrow}d}}{[k_{\uparrow}^2+(k_{\uparrow}^{\mathrm{L}})^2][k_{\uparrow}^2+(k_{\uparrow}^{\mathrm{R}})^2]}+\frac{16k_{\downarrow}^{\mathrm{L}}k_{\downarrow}^{\mathrm{R}}k_{\downarrow}^2e^{-2k_{\uparrow}d}}{[k_{\downarrow}^2+(k_{\downarrow}^{\mathrm{L}})^2][k_{\downarrow}^2+(k_{\downarrow}^{\mathrm{R}})^2]}\right\}, \tag{25}$$

$$G^{(\pi)} = G_{\mathrm{I}}^{(\pi)} + G_{\mathrm{II}}^{(\pi)} = \frac{2e^2}{\pi^2\hbar d}\left\{\frac{16k_{\downarrow}^{\mathrm{L}}k_{\uparrow}^{\mathrm{R}}k_{\uparrow}^2e^{-2k_{\uparrow}d}}{[k_{\uparrow}^2+(k_{\downarrow}^{\mathrm{L}})^2][k_{\uparrow}^2+(k_{\uparrow}^{\mathrm{R}})^2]}+\frac{16k_{\downarrow}^{\mathrm{L}}k_{\downarrow}^{\mathrm{R}}k_{\downarrow}^2e^{-2k_{\uparrow}d}}{[k_{\downarrow}^2+(k_{\downarrow}^{\mathrm{L}})^2][k_{\downarrow}^2+(k_{\downarrow}^{\mathrm{R}})^2]}\right\}. \tag{26}$$

Based on eqn (25) and (26), TMR can be written as

$$\mathrm{TMR} = \frac{G^{(0)}-G^{(\pi)}}{G^{(0)}} = \frac{2P_{\mathrm{L}}P_R}{1+P_{\mathrm{L}}P_R},\ P_{\mathrm{L}} = \frac{[k_{\uparrow}^2+(k_{\downarrow}^{\mathrm{L}})^2]k_{\uparrow}^{\mathrm{L}}-[k_{\downarrow}^2+(k_{\uparrow}^{\mathrm{L}})^2]k_{\downarrow}^{\mathrm{L}}}{[k_{\uparrow}^2+(k_{\downarrow}^{\mathrm{L}})^2]k_{\uparrow}^{\mathrm{L}}+[k_{\downarrow}^2+(k_{\uparrow}^{\mathrm{L}})^2]k_{\downarrow}^{\mathrm{L}}}$$
$$P_R = \frac{k_{\uparrow}^3[k_{\downarrow}^2+(k_{\uparrow}^{\mathrm{L}})^2][k_{\downarrow}^2+(k_{\downarrow}^{\mathrm{R}})^2]e^{-2k_{\uparrow}d}k_{\uparrow}^{\mathrm{R}}-k_{\downarrow}^3[k_{\uparrow}^2+(k_{\uparrow}^{\mathrm{L}})^2][k_{\uparrow}^2+(k_{\uparrow}^{\mathrm{R}})^2]e^{-2k_{\downarrow}d}k_{\downarrow}^{\mathrm{R}}}{k_{\uparrow}^3[k_{\downarrow}^2+(k_{\uparrow}^{\mathrm{L}})^2][k_{\downarrow}^2+(k_{\downarrow}^{\mathrm{R}})^2]e^{-2k_{\uparrow}d}k_{\uparrow}^{\mathrm{R}}+k_{\downarrow}^3[k_{\uparrow}^2+(k_{\uparrow}^{\mathrm{L}})^2][k_{\uparrow}^2+(k_{\uparrow}^{\mathrm{R}})^2]e^{-2k_{\downarrow}d}k_{\downarrow}^{\mathrm{R}}}, \tag{27}$$

where P_{L} and P_{R} are the effective spin polarization of the left and right ferromagnetic electrodes, respectively.[262,288] Moreover, Velev *et al.* theoretically predicted the four distinct resistance states in the $SrRuO_3/BaTiO_3/SrRuO_3$ MFTJs,[285] where the spin-polarized conductance G_σ is calculated using the Landauer–Büttiker formula

$$G_\sigma = \frac{e^2}{h}\sum_{k_{\parallel}} T_\sigma(k_{\parallel}, E_{\mathrm{F}}). \tag{28}$$

In eqn (28), $T_\sigma(k_{\parallel}, E_{\mathrm{F}})$ is the transmission coefficient with spin σ ($\sigma = \uparrow, \downarrow$), the transverse Bloch wave vector $\boldsymbol{k}_{\parallel} = (k_x, k_y)$, E_{F} is the Fermi level, e is the electron charge, and h is Planck's constant. TMR and TER ratios are defined as

$$\mathrm{TMR} = \frac{G_{\uparrow\uparrow}-G_{\uparrow\downarrow}}{G_{\uparrow\uparrow}+G_{\uparrow\downarrow}},\ \mathrm{TER} = \frac{G_{\leftarrow}-G_{\rightarrow}}{G_{\leftarrow}+G_{\rightarrow}}, \tag{29}$$

where $G_{\uparrow\uparrow}$ and $G_{\uparrow\downarrow}$ are the total conductance of the PC and APC magnetic configurations, respectively. $G_{\rightarrow}$ and $G_{\leftarrow}$ are the total conductance at the right and left polarization directions of ferroelectric BFO, respectively.[285]

In Fig. 30a, the epitaxial $La_{0.6}Sr_{0.4}MnO_3$/BFO/$La_{0.6}Sr_{0.4}MnO_3$ MFTJs fabricated by magnetron sputtering show strong ferroelectric characteristics and exchange bias.[57] More importantly, in Fig. 30b, the entire *R–H* curve shifts by reversing the ferroelectric polarization, resulting in two (anti) parallel states and four resistance states. Particularly, in FSMA, the magnetic field can induce the martensitic transition, which can generate a large magnetoelectric effect in the FSMA/piezoelectric composites.[153] By considering the controllable magnetoelectric couplings in FSMA, $Ni_{50.3}Mn_{36.9}Sb_{12.8}$ serves as the electrode in the BFO-based MFTJs (Fig. 30c),[152] where the magnetic field induced strain of $Ni_{50.3}Mn_{36.9}Sb_{12.8}$ can be transferred into ferroelectric BFO. Consequently, the ferroelectric polarization of BFO in the $Ni_{50.3}Mn_{36.9}Sb_{12.8}$/BFO/$Ni_{50.3}Mn_{36.9}Sb_{12.8}$ MFTJs is engineered by the transferred strains (Fig. 30c), which can further affect the TER.[152] It is noteworthy that the BFO-based MFTJs integrate the MTJs and FTJs, which provides new insight for developing BFO-based multifunctional spintronic devices. Unfortunately, the achieved TMR and TER of the BFO-based MFTJs are smaller than 20%,[57,152] which needs to be enhanced. Besides, Yin *et al.* demonstrated that an inverse TMR appears in the Fe_4N/T-BFO/Fe_4N MFTJs,[147] which does not obey the Julliere's formula of TMR = $2P_1P_2/(1 + P_1P_2)$.[288] The inverse TMR of the Fe_4N/T-BFO/Fe_4N MFTJs can switch into a positive TMR by an applied bias, which can be ascribed to the spin-polarized transport in MFTJs. Obviously, the spin-polarized ferromagnetic electrodes provide an opportunity for enhancing the novel electronic properties of the BFO-based heterostructures.

Moreover, the TER in the junctions is demonstrated to be associated with the barrier layer thickness and electrode screening length in theory[56,204] and experiments.[289,290] Based on the Wentzel–Kramers–Brillouin model, TER is defined as[56]

$$\mathrm{TER} = \exp\left[\frac{\sqrt{2m}}{\hbar}\frac{\delta\phi}{\sqrt{\phi}}d\right], \delta\phi \approx \frac{edP(\delta_2-\delta_1)}{\varepsilon(\delta_2+\delta_1)}, \tag{30}$$

where m is the electron effective mass, d is the ferroelectric layer thickness, ϕ is the average potential height, $\delta\phi$ is the change of the potential induced by the ferroelectric polarization reversal, P is the ferroelectric polarization, ε is the dielectric permittivity and $\delta_{1,2}$ is the screening length of two electrodes in FTJs. Assuming that the magnitude of ferroelectric polarization is uniform in the ferroelectric layer and does not change with the polarization reversal, TER in formula (30) can be deduced as[290]

$$\mathrm{TER} \approx \exp\left[\frac{\sqrt{2m}}{\hbar\sqrt{\phi}}\frac{eP(\delta_2-\delta_1)}{\varepsilon(\delta_2+\delta_1)}d^2\right]. \tag{31}$$

In eqn (31), TER exponentially depends on the ferroelectric polarization, where a large TER in the junctions can be achieved by enlarging the ferroelectric polarization. Therefore, BFO with an ultrahigh ferroelectric polarization attracts much attention to increase TER. In particular, based on the ferroelectric photovoltaic effect in the BFO-based FTJs,[55] Yin *et al.* have predicted a multiferroic photovoltaic effect in the LSMO/BFO/Fe_4N MFTJs irradiated with linearly or left-hand (right-hand) polarized light,[291] where the magnitude of the induced photocurrent can be tailored by both the ferroelectric polarization of

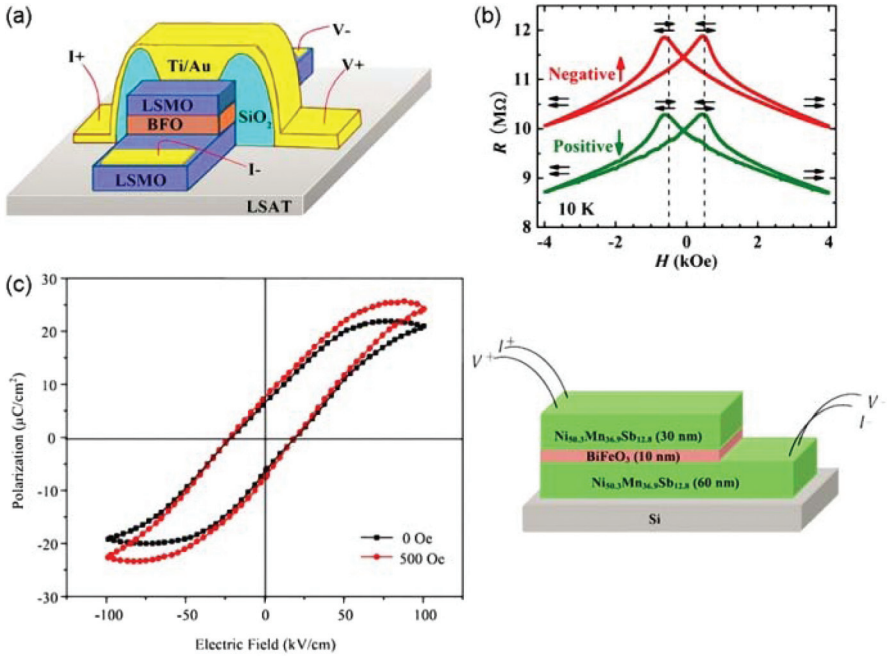

Fig. 30 (a) Schematic diagram of measurements and (b) *R*–*H* curves at the positive (negative) ferroelectric polarization of $La_{0.6}Sr_{0.4}MnO_3$/BFO/$La_{0.6}Sr_{0.4}MnO_3$ MFTJs. Adapted with permission from ref. 57. Copyright 2014, AIP Publishing. (c) Room-temperature ferroelectric hysteresis loop with and without a magnetic field and a schematic diagram of $Ni_{50.3}Mn_{36.9}Sb_{12.8}$/BFO/$Ni_{50.3}Mn_{36.9}Sb_{12.8}$ MFTJs. Adapted with permission from ref. 152. Copyright 2016, AIP Publishing.

the BFO barrier and magnetization configurations of two ferromagnetic electrodes. The direction of the induced photocurrent is only dependent on the polarization direction of ferroelectric BFO in the LSMO/BFO/Fe_4N MFTJs. The multiferroic photovoltaic effects should exist in general MFTJs considering the intrinsic ferroelectric and ferromagnetic characteristics of MFTJs.

D. Emergent characteristics

1. Two-dimensional electron gas. The 2DEG is known as a promising property within nanoscale electronic confinement[157,292,293] for developing advanced nanoelectronic devices,[158,294,295] such as high mobility field-effect transistors. The polar/nonpolar $LaAlO_3/SrTiO_3$ interface is a typical example for inducing the 2DEG, where the polar discontinuity rebuilds the electrostatic potential at the interface.[296] In particular, the ferroelectric/insulator interface can also induce the polar discontinuity, where the reversible ferroelectric polarization can transfer the electrons or holes into the interface to form the 2DEG or two-dimensional hole gas.[293,297,298] It is noteworthy that the 2DEG has been demonstrated in BFO-based heterostructures. In 2011, Zhang *et al.* predicted that the 2DEG appears at the $SrTiO_3$/BFO interface by first-principles calculations.[58] In the $SrTiO_3$/BFO superlattices with two n-type $(BiO)^+/(TiO_2)^0$ interfaces,[58] the region of the 2DEG is symmetric at two interfaces with paraelectric BFO (see the red curve in Fig. 31a). However, when the ferroelectric polarization of BFO points towards the specific interface, the 2DEG only occurs at one interface of the $SrTiO_3$/BFO superlattices with ferroelectric BFO, and the induced 2DEG at the $SrTiO_3$/BFO interface originates from the electronic reconstruction to avoid the polarization catastrophe.[58] Meanwhile, the polarization screen effect results in the ferroelectric polarization tailored 2DEG in the $SrTiO_3$/BFO superlattices.[58]

The 2DEG has already been observed experimentally in the $SrTiO_3$/BFO superlattices.[156] In Fig. 31c, the 2DEG is observed at the $SrTiO_3$/BFO interface by cross-sectional current mapping.[156] Ti cations of $SrTiO_3$ diffuse into Fe sites of BFO, but Fe cations do not diffuse into the $SrTiO_3$ substrate, which has been observed by atom-resolved electron energy loss spectroscopy (Fig. 31d).[156] Meanwhile, diffused Ti exists in a mixed valence state of +3/+4, which is different from the valence state of +4 in Ti cations of $SrTiO_3$, as shown in Fig. 31e.[156] The above results indicate that the electronic reconstruction due to polarization discontinuity and the changed valence state of diffused Ti are crucial to form the 2DEG in the $SrTiO_3$/BFO superlattices. Besides, the 2DEG was also predicted at the interfaces between multiferroic BFO and antiferromagnetic Mott insulator $LaTiO_3$,[59,299,300] where the k_z-independent discrete energy levels (Fig. 31b) confine the electrons at the interfaces to form 2DEG.[59,301]

Particularly, Zhang *et al.* demonstrated the anisotropic polarization-induced conductivity in the BFO/$TbScO_3$ heterostructures with 109° stripe domain walls.[224] At the BFO/$TbScO_3$ interface (Fig. 32), it is conducting along the striped domain, but insulating in the direction perpendicular to the striped domain. Moreover, at the cross-sectional BFO/$TbScO_3$ interface along the striped domain (Fig. 33), the conductivity

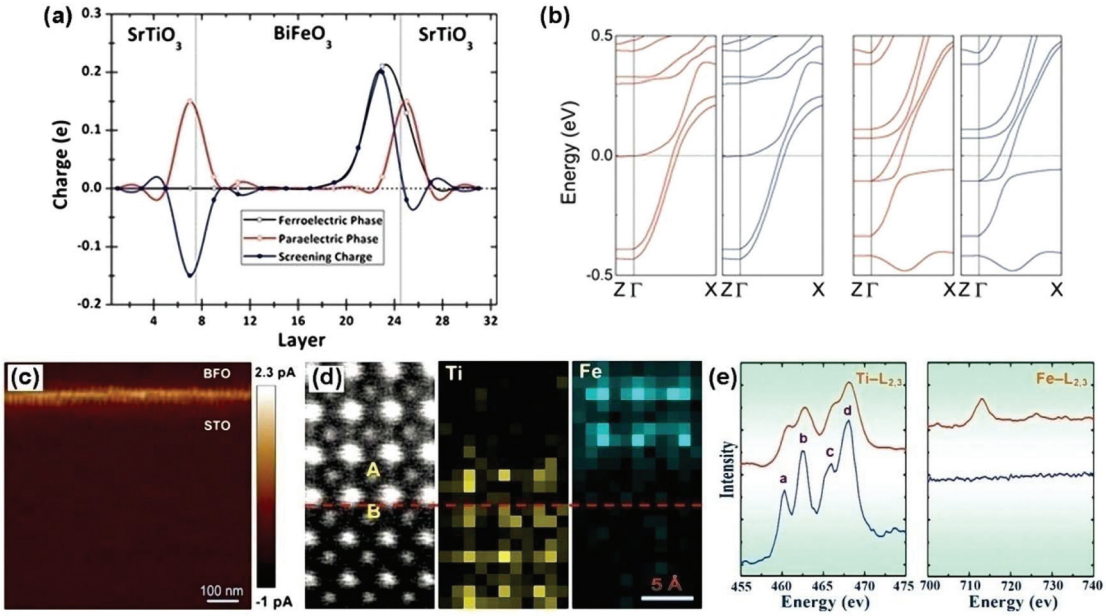

Fig. 31 (a) Calculated distribution of the free charges and screening charges on Fe and Ti atoms per formula across the $SrTiO_3$/BFO superlattices in the paraelectric and ferroelectric states of BFO. The screening charge is the difference of the free charges in the paraelectric and ferroelectric superlattices. Adapted with permission from ref. 58. Copyright 2011, AIP Publishing. (b) Band structure of $LaTiO_3$/BFO superlattices with specific LaO–BiO and TiO_2–BiO structures. Reproduced from ref. 59 with permission from the Royal Society of Chemistry. (c) Nanoscale current mapping of the cross-sectional (100) $SrTiO_3$/BFO interface. (d) Atom-resolved electron energy loss spectroscopy mapping. The interface is indicated by a dashed line. (e) Electron energy loss spectra with Ti–$L_{2,3}$ and Fe–$L_{2,3}$ edges. The red spectrum is recorded from the interfacial Fe site (site A in (c)) and the blue one from the interfacial Ti site (site B in (c)). Adapted with permission from ref. 156. Copyright 2015, AIP Publishing.

changes by switching the ferroelectric polarization in domain stripes of BFO, including the doped electrons or holes at the interfaces. In particular, the conducting channel width in BFO is dominated by the screening length δ of the polarization charge,[224] which can be described using Thomas–Fermi approximation as[302]

$$\delta = \frac{1}{e}\sqrt{\frac{\varepsilon}{\rho_F}}. \quad (32)$$

In eqn (32), ε is the dielectric permittivity of BFO, e is the elementary charge and ρ_F is the density of states at the Fermi level.[224] Zhang *et al.* obtained a theoretical value of $\delta \sim 1$ nm by considering a dielectric permittivity of $\sim 100\varepsilon_0$ in BFO and a ρ_F of ~1 eV per u.c., which is in good agreement with the experimental value of 1.5 nm.[224] Overall, these results of the 2DEG in the BFO-based heterostructures offer a platform for developing the novel BFO-based electronic devices.

2. Valley features: generation and modulation. The valley DOF has been intensively investigated in two-dimensional materials, such as graphene[303] and MoS_2[304–307] with a honeycomb lattice structure (Fig. 34a). Based on the broken inversion symmetry, the valley-dependent optoelectronics[308,309] and spin–valley coupled physics[305,310] have been paid much attention, such as the valley-selective circular dichroism[311] and dichroic spin–valley photocurrent.[312] Novel valley-based phenomena and devices have also been proposed, such as the valley Hall effect,[305,306] valley-polarized quantum anomalous Hall effect,[313] valley diodes[314] and valley valves.[315] Valleytronics will integrate with spintronic[307,316] and optoelectronic devices,[309,311,312] which is beneficial for designing multifunctional electronic devices. In particular, the graphene-like hexagonal lattice structure also exists in (111)-oriented perovskite ABO_3/$AB'O_3$ oxide heterostructures, but its topological[317–322] and valley phenomena are different from two-dimensional materials.[303,307] The ferroelectric Rashba semiconductor[323] and a new ferrovalley material[324,325] with a spontaneous valley polarization have been demonstrated due to the broken inversion symmetry by ferroelectric polarization.

Since BFO has the ferroelectric characteristic and photovoltaic effect, it might exhibit a novel performance in the valley index. Meanwhile, (111)-oriented R-BFO with two atomic layers has a special honeycomb structure with both Fe and surrounding O atoms (Fig. 34a),[2,326,327] where the valley characteristic will be different from those of two-dimensional graphene or transition metal dichalcogenides. Yamauchi *et al.* proposed the valley characteristic in rhombohedral $BiIrO_3$ with a strong SOC due to the heavy metal Ir atom.[328] Moreover, the two-atomic-layer thick $BiIrO_3$ shows strong spin–valley coupling in the $BiAlO_3$/$BiIrO_3$ ferroelectric heterostructures.[328] However, in Fig. 34b, the dispersion of the valence band maximum (VBM) in $BiIrO_3$ is nearly flat in the $BiAlO_3$/$BiIrO_3$ heterostructures, which is disadvantageous to the valleytronic and spintronic devices.[328] In Fig. 34c, the flat dispersion of the VBM in $BiIrO_3$ can be effectively lifted by the proximity effect of antiferro-

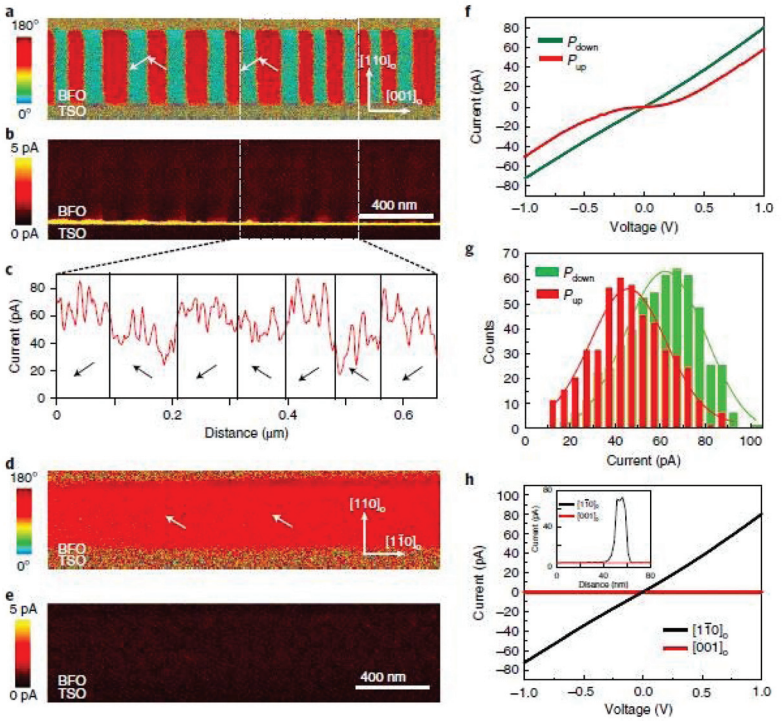

Fig. 32 (a and d) Piezoresponse force microscopy and (b and e) conductive atomic force microscopy images of the cross-sectional BFO film in the BFO/$TbScO_3$ heterostructures with 109° domain arrays. The cross-sectional BFO films in (a and b) and (d and e) are perpendicular and parallel to the 109° stripe domain, respectively. (c) Average current profile of the BFO/$TbScO_3$ interface, corresponding to the dashed-line-marked region in (b). The white arrows in (a) and (d) indicate the three-dimensional polarization vectors of BFO. (f) *I*–*V* curves at the BFO/$TbScO_3$ interface with upward and downward polarizations. The 'P_{up}' symbol indicates the polarization pointing towards the BFO/$TbScO_3$ interface, and the 'P_{down}' symbol shows the polarization pointing away from the interface. (g) Histogram of the current in upward-polarized and downward-polarized BFO shown in (b). (h) *I*–*V* curves of the BFO/$TbScO_3$ interface with the directions perpendicular and parallel to the 109° stripe domain. The inset of (h) shows the current profile of the BFO/$TbScO_3$ interface. Adapted with permission from ref. 224. Copyright 2018, Nature Publishing Group.

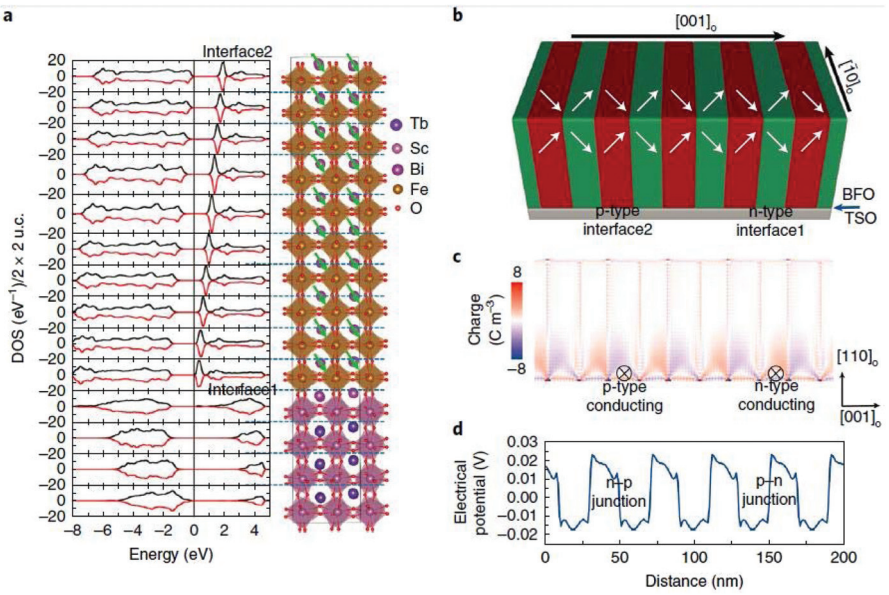

Fig. 33 (a) Layer-resolved density of states in the BFO/$TbScO_3$ superlattices by first-principles calculations. (b) Domain structure of BFO with 109° domain arrays simulated with the phase-field theory. (c) Bound charge distribution of the BFO/$TbScO_3$ interface along the domain stripe. (d) Potential distribution of the BFO/$TbScO_3$ interface perpendicular to the domain stripe. The green arrows in (a) and white arrows in (b) indicate the ferroelectric polarization direction of BFO. Adapted with permission from ref. 224. Copyright 2018, Nature Publishing Group.

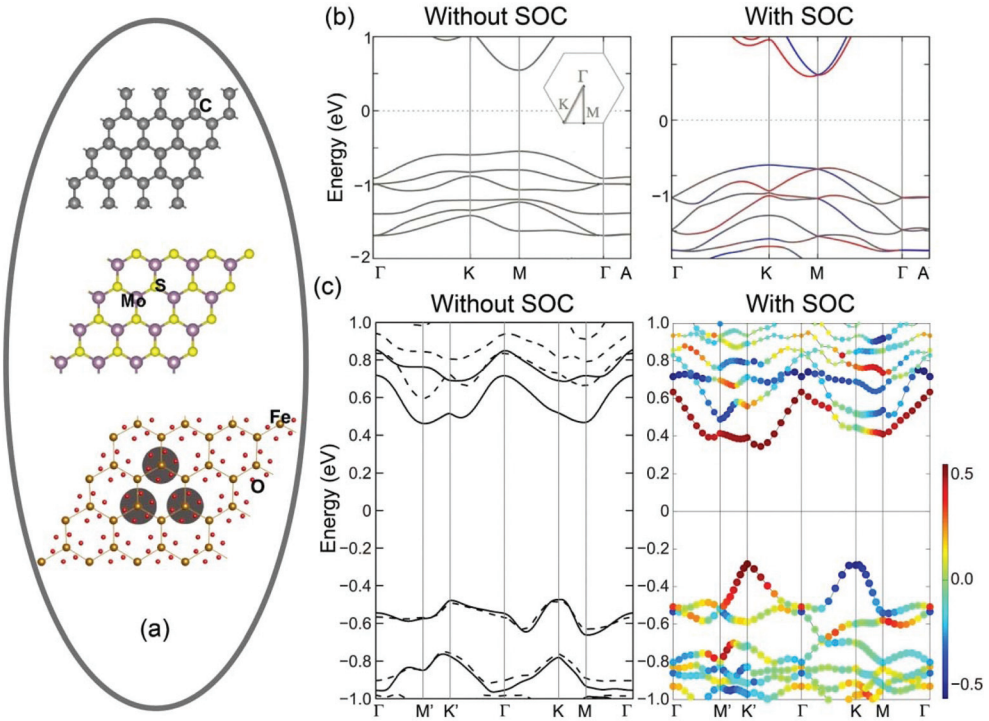

Fig. 34 (a) Top view of graphene, monolayer MoS_2 and bilayered BFO. Adapted with permission from ref. 32. Copyright 2018, American Chemical Society. (b) Band structure of the $BiAlO_3/BiIrO_3$ superlattices, where the s_z polarization is highlighted in blue (up) and red (down) colors. Adapted with permission from ref. 328. Copyright 2015, American Physical Society. (c) Band structure of the BFO/$BiIrO_3$ superlattices with BFO/OIB termination, where the solid and dashed black lines represent the spin-up (spin-down) band without SOC. For the case with SOC in (c), the circle represents $BiIrO_3$, and the spin projection is depicted by the color scale. Adapted with permission from ref. 32. Copyright 2018, American Chemical Society.

magnetic BFO,[32] where a high spin polarization appears in the lifted valley at high symmetric points of K and K′. Particularly, the valley polarization occurs in the $BiIrO_3$/BFO superlattices. In Fig. 34c, the conduction band minimum of $BiIrO_3$ forms a quasi-direct band gap at the K′ point and an indirect band gap at the K point, respectively, which makes the electrons at the K′ point easier to emit than that those at the K point due to the extra momentum transformation.[329] Meanwhile, in Fig. 34c, the electrons at the K′ point would be stimulated from the spin-up to spin-up polarized channels, while electrons at the K point shall be transformed from spin-down to spin-up polarized channels with extra energy consumption.[32] So, the different momentum and spin characteristics at K′ and K points can distinguish the valley at K and K′ points, which generates a valley polarization in $BiIrO_3$ of the BFO/OIB model.[32]

Moreover, $BiIrO_3$ shows a flat dispersion at the valence band maximum in the BFO/BIO model.[32] Hence, the relatively parallel and antiparallel directions of ferroelectric polarization in BFO and $BiIrO_3$ can switch the valley states of the BFO/$BiIrO_3$ superlattices,[32] where the parallel and antiparallel ferroelectric polarizations can induce the flat valley and polarized valley, respectively. Owing to the different coercive fields of BFO and $BiIrO_3$, the ferroelectric states in the BFO/$BiIrO_3$ superlattices can be tailored by an electric field,[61,330,331] which can switch the valley states of the BFO/$BiIrO_3$ superlattices. Besides, the valley states can be modulated in transition-metal dichalcogenide monolayers by the magnetic proximity effect.[332] In the $BiIrO_3$/BFO superlattices (Fig. 35a),[32] the spin polarization in the valley of $BiIrO_3$ is highly dependent on the [100]- and [001]-oriented magnetization of Fe in BFO. Such a phenomenon suggests that the magnetic fields parallel ($M_{\text{in-plane}}$) and perpendicular ($M_{\text{out-of-plane}}$) to the honeycomb plane might produce different spin polarizations in the valley of the BFO/$BiIrO_3$ superlattices. Yin *et al.* proposed a BFO/$BiIrO_3$-based prototype device with multiple resistance states by considering the electric field switched valley polarization and magnetic field tuned spin polarization in the lifted valley (Fig. 35b),[32] which can be used as nonvolatile ferroelectric random access memories[61] and valley filters.[333] The large ferroelectric polarization and high Curie temperature of BFO also favor the nonvolatile ferroelectric modulation in the valley index, which may promote the next-generation valleytronic and ferroelectric devices.

The ultrathin T-BFO films with a thickness of one-unit-cell still show the ferroelectric order,[334] which was directly observed by aberration-corrected scanning transmission electron microscopy. The ferroelectric order of T-BFO under the two-dimensional limit makes BFO promising in novel high-density nonvolatile storage and memories.

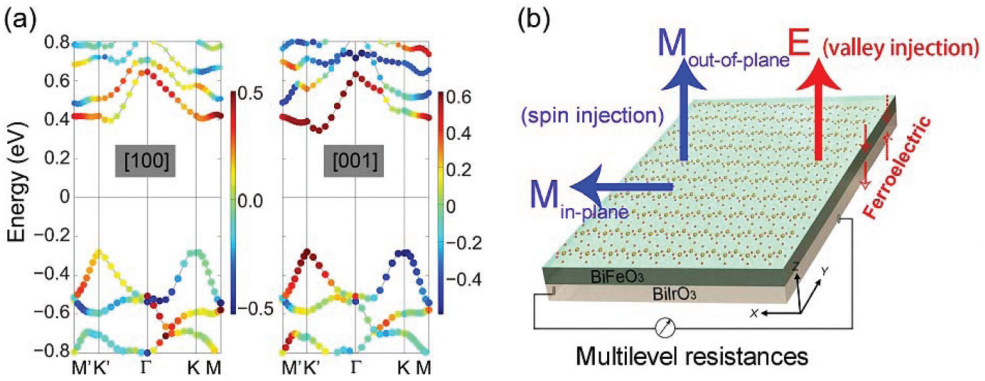

Fig. 35 (a) Band structure of the BFO/OIB model with the [100]- and [001]-oriented Fe spins, respectively. The circle represents $BiIrO_3$, and the spin projection is depicted by the color scale. (b) Diagram of the valley-spin component for the BFO/$BiIrO_3$ superlattices. Adapted with permission from ref. 32. Copyright 2018, American Chemical Society.

IV. Applications

Based on the ferroelectric polarization tailored photovoltaic effect and magnetoelectric coupling of BFO, the BFO-based heterostructures can be used in two aspects: (i) nonvolatile data storage and logic switching with a BFO ferroelectric barrier, and (ii) photoelectrochemical water splitting and photocatalysis with a BFO photoelectrode. The two kinds of applications are discussed respectively in the following subsections.

A. Nonvolatile data storage and logic switching

The BFO/ferromagnet heterostructures show novel electrical and magnetic properties, including the photovoltaic effect, RS and electric field control of magnetism, which have been discussed in section III. These characteristics offer opportunities for writing the magnetic state in BFO-based junctions,[57] spin valves[49,51] and photodetectors.[335] BFO-based nonvolatile ferroelectric random access memories, memristors[55] and synapse-like networks[284] also have been proposed. In particular, Guo *et al.* demonstrated a cross-bar prototype memory with the photovoltaic effect (Fig. 36), where each cell can display the V_{OC} and J_{SC}. The cross-bar structure can read data by itself, which saves the driving force compared to other memory structures.[336] Such a microarray structure is convenient to design data storage. Here, the Au/Cr/T-BFO/LSMO structure is taken as an example to illustrate the mechanism of nonvolatile BFO-based data storage and logic switching.

In Fig. 8f and 37a, the Au/Cr/T-BFO/LSMO microarray in the upward and downward ferroelectric polarizations show distinct J_{SC} and V_{OC}, which can represent the "0" and "1" states, respectively.[132] The writing of "0" and "1" states can be realized by changing the ferroelectric polarized direction of T-BFO, and the reading of "0" and "1" states is accessible by light irradiation. The data storage with electric writing and optical reading modes consumes less energy than the conventional ones. Meanwhile, in Fig. 8f and 37b, the Au/Cr/T-BFO/LSMO microarray[132] shows the distinct states with and without light illumination, which can serve as the reversible light-switching "ON" and "OFF" logic states. Besides, for the nonvolatile memory, the long data retention and excellent anti-fatigue are two essential factors, which have been examined in

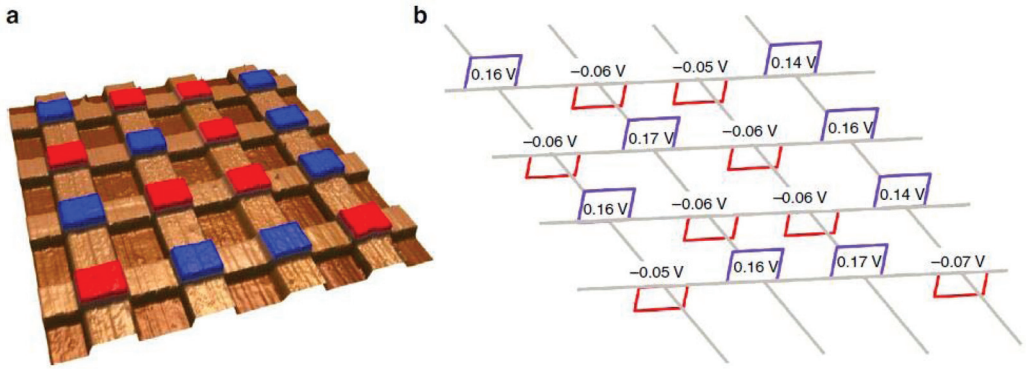

Fig. 36 (a) Topology of the prototype 16-cell Fe/BFO/$La_{0.7}Sr_{0.3}MnO_3$ memory with a cross-bar architecture. The polarization in each cell is presented, where the blue (red) colour indicates upward (downward) polarization. (b) The induced V_{OC} in each cell under the light of 20 mW cm^{-2}. Adapted with permission from ref. 336. Copyright 2013, Nature Publishing Group.

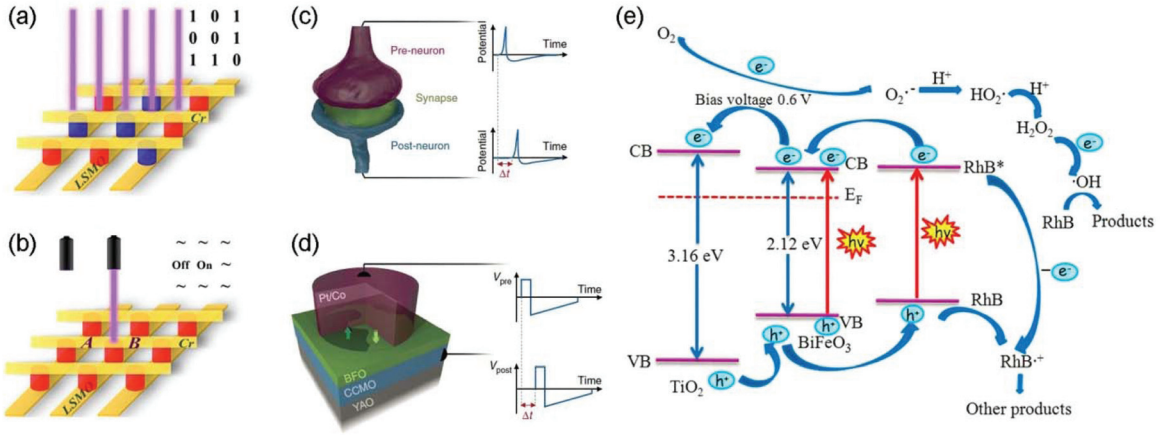

Fig. 37 Designations of (a) data storage and (b) the logic switching microdevice prototype based on the Au/Cr/T-BFO/LSMO microarray. The red and blue colors in (a) and (b) represent the downward and upward ferroelectric polarizations, respectively. Adapted with permission from ref. 132. Copyright 2017, American Chemical Society. (c) Sketch of pre- and post-neurons connected by a synapse. (d) Sketch of the Pt/Co/$BiFeO_3$/(Ca,Ce)MnO_3 ferroelectric memristors. Adapted with permission from ref. 284. Copyright 2017, Nature Publishing Group. (e) Schematic pathways of photoelectrochemical degradation of rhodamine B by the BFO/TiO_2 composite electrode. Adapted with permission from ref. 35. Copyright 2014, American Chemical Society.

the Fe/BFO/$La_{0.7}Sr_{0.3}MnO_3$ heterostructures.[336] As seen in Fig. 38, the V_{OC} and J_{SC} in the Fe/BFO/$La_{0.7}Sr_{0.3}MnO_3$ cells did not deteriorate for four months. Then, the cells after bipolar switching of 10^8 cycles did not show fatigue, which overstepped the rewriting cycle of ~10^5 in the flash memory. The long data retention and excellent anti-fatigue of the Fe/BFO/$La_{0.7}Sr_{0.3}MnO_3$ junctions are beneficial for developing nonvolatile memory.[336]

The memristive behavior of the BFO-based FTJs can be utilized as an electronic synapse due to the sensitive voltage tunable conductance (Fig. 29a).[284] In the Pt/Co/BFO/(Ca,Ce)MnO_3 ferroelectric memristor (Fig. 37d), the applied voltage pulse can engineer the domain population, which further results in resistance changes. In such a memristor, the resistance is dependent on the history of the applied voltage, which emulates the synaptic function with the plasticity (Fig. 37c).

BFO can also be utilized in capacitors,[337] especially the so-called ferroelectric capacitive memory.[338,339] In the BFO/Si_3N_4/p-Si heterostructures, the polarized charge of ferroelectric BFO can stabilize the positive charges of Si_3N_4, which can generate

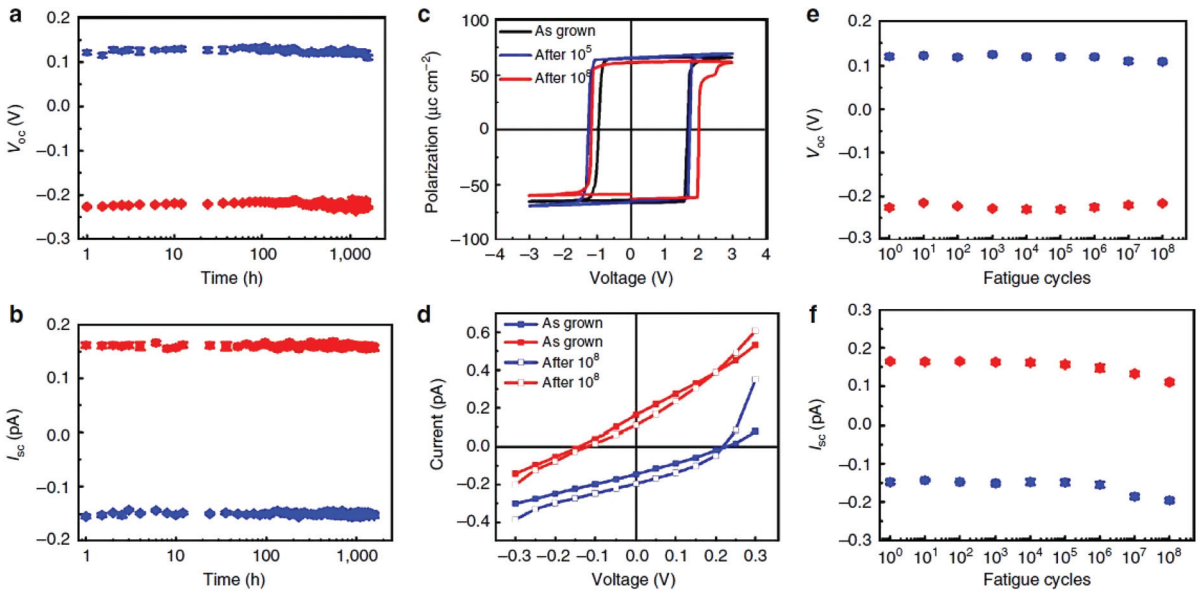

Fig. 38 Retention test of (a) V_{OC} and (b) J_{SC} in the Fe/BFO/$La_{0.7}Sr_{0.3}MnO_3$ heterostructures under a halogen lamp of 20 mW cm^{-2}. (c) *P*–*E* and (d) *I*–*V* curves of the Fe/BFO/$La_{0.7}Sr_{0.3}MnO_3$ heterostructure after repetitive polarization switching by a pulse of ±3 V with 1 ms. The blue and red colors refer to the upward and downward polarizations, respectively. Adapted with permission from ref. 336. Copyright 2013, Nature Publishing Group.

the memcapacitive effect,[339] which is advantageous for the capacitive switching in a pure Si_3N_4/p-Si structure without coated BFO. Meanwhile, the capacitive switching of the BFO/Si_3N_4/p-Si heterostructures can be modulated by the intensity and wavelength of light due to the ferroelectric photovoltaic effect of BFO, which can serve as a photodetector.[339] Besides, except the nonvolatile data storage and synapse-like devices, the BFO-based heterostructures also can be utilized in the ferroelectric-modulated superconducting critical temperature and strong ferroelectric field effect in $YBa_2Cu_3O_{7-\delta}$/BFO heterostructures,[340] and magnetic field modulated surface acoustic wave excitation on BFO.[341] These phenomena make the BFO-based heterostructures attractive for developing multifunctional electronic devices.

B. Photoelectrochemical water splitting and photoelectrocatalysis

BFO with the ferroelectric-modulated photovoltaic effect can serve as the photoelectrode under visible-light illumination. In particular, ferroelectric BFO films can form high-frequency in-plane and out-of-plane electromechanical images under the liquid conditions,[342,343] which expands the applications of ferroelectricity in BFO. Ren *et al.* indicated that the photocurrent and photo-to-current efficiency of BFO can be improved by bringing it in contact with hydrophilic materials, such as RGO (Fig. 6d).[39] Such an RGO/BFO composite electrode can be utilized in photoelectrochemical water splitting, where the light energy can be efficiently converted into chemical and electrical energies.

Particularly, the BFO-based heterostructures can also be used in the photocatalytic process, where BFO is commonly utilized in the form of nanoparticles owing to its high surface area.[344] Generally, visible light sensitive BFO is always interacted with typical semiconductor-based photocatalysts to improve the photocatalytic efficiency under visible light, such as TiO_2 with a band gap of 3.0 eV or 3.2 eV,[345,346] metal-free graphitic C_3N_4 with a band gap of 2.7 eV[347] and magnetic spinel $ZnFe_2O_4$ with a band gap of 1.92 eV.[348] In the C_3N_4/*x*BFO heterostructures, the photocatalytic efficiency is 1.4 times higher than that of pure C_3N_4 by optimizing the composition of BFO at x = 10 wt%, where x indicates the weight ratio of BFO to C_3N_4 and the photocatalytic efficiency is evaluated by degrading rhodamine B in an aqueous solution under visible light irradiation.[347] Moreover, owing to the aligned ferroelectric polarization, the photocatalytic activities of C_3N_4/*x*BFO heterostructures can further increase by 1.3 times *via* mechanical pressing and by 1.8 times *via* electrical poling.[347]

In the TiO_2/BFO heterostructures illuminated with visible light in an energy interval from 2.53 to 2.70 eV, the pattern of reduced silver cations at the TiO_2 surface simulates the domain structure of BFO.[345] However, the silver reduction is insignificant in pure TiO_2. So, the photo-generated electrons are modulated by the dipolar field in ferroelectric domains, which finally pass through TiO_2 and reduce the silver cations at the surface.[345] Moreover, as seen in Fig. 37e, the BFO/TiO_2 composite electrode is utilized to degrade rhodamine B, which can be divided into two pathways.[35] On the one hand, the photo-generated electrons react with chemisorbed O_2, which combines with H^+ in the solution and subsequently forms H_2O_2. The formed H_2O_2 further reacts with the electrons in the counter electrode, which will modulate the degradation and mineralization of the adsorbed molecules near rhodamine B (Fig. 37e). On the other hand, the visible-light irradiation can directly excite the rhodamine B molecules. The photo-excited electrons and holes in rhodamine B interact with the BFO/TiO_2 composite electrodes, as shown in Fig. 37e,[35] which can further modulate the photoelectrocatalytic degradation towards rhodamine B under visible light with improved photo-conversion efficiency (Fig. 11a).

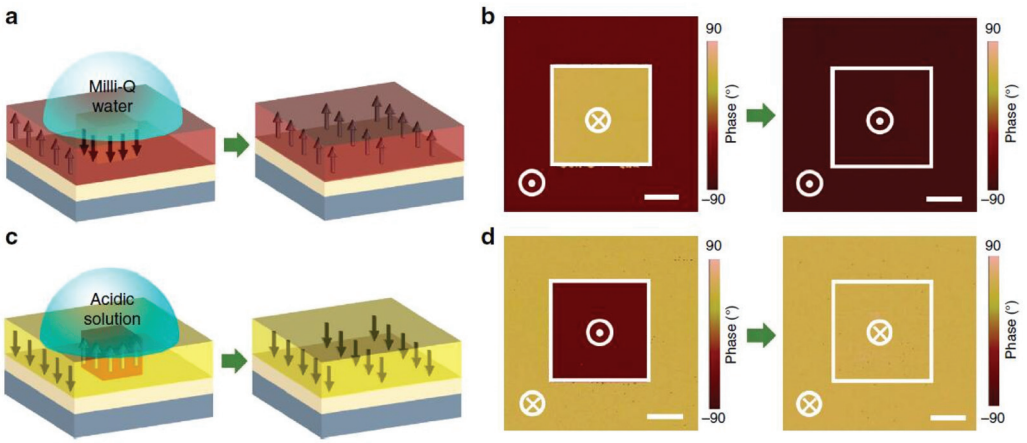

Fig. 39 (a and c) Diagram of modulated ferroelectric polarization switching of BFO on the $SrTiO_3$ substrate with a (La,Sr)MnO_3 buffer layer, where the polarization switches from downward (upward) to upward (downward) when BFO is exposed to Milli-Q water (acidic solution). The arrow indicates the out-of-plane component of ferroelectric polarization. (b and d) Piezoresponse force microscopy images of BFO before and after exposure to the aqueous solution, corresponding to (a) and (c), respectively. The scale bar in (b) and (d) is 2 μm. Adapted with permission from ref. 350. Copyright 2018, Nature Publishing Group.

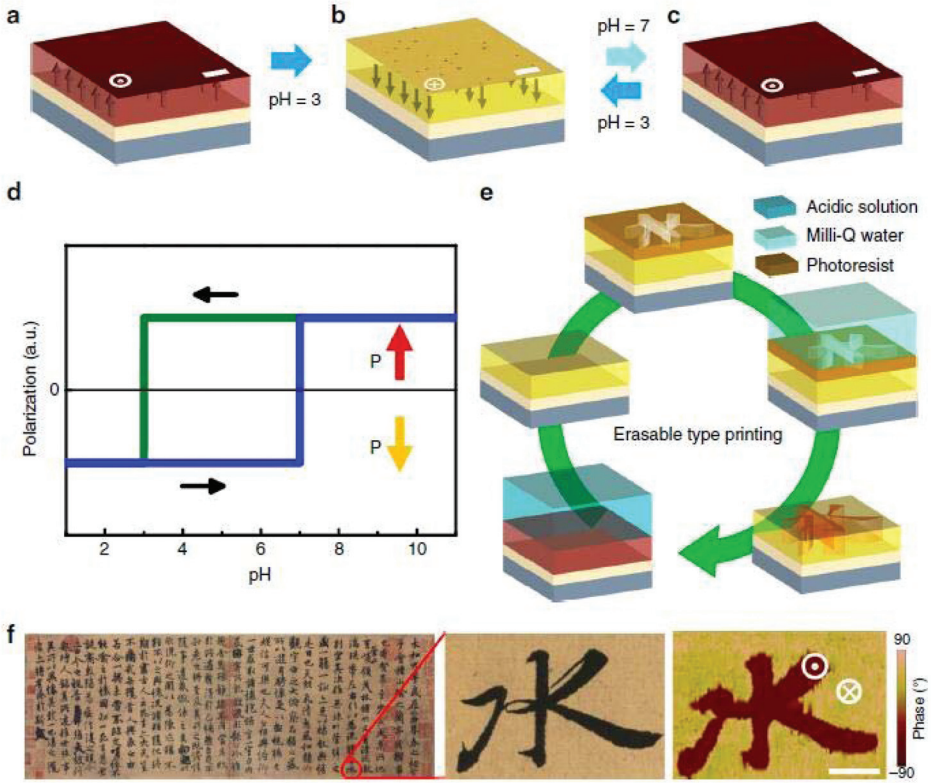

Fig. 40 Piezoresponse force microscopy images of (a) initially upward-polarized BFO, (b) downward-polarized BFO after being exposed to acidic solution and (c) cyclically switchable polarization of BFO after being exposed to Milli-Q water and acidic solution. The scale bar in (a–c) is 2 μm. (d) Out-of-plane component of polarization in initially upward-polarized BFO in aqueous solution with different PH values. (e) Schematics of printing and erasing the ferroelectric polarization of BFO by controlling the PH value of the aqueous solution in contact with the surface of BFO. (f) Piezoresponse force microscopy images of Chinese characteristic water from a calligraphy artwork. The scale bar in (f) is 10 μm. Adapted with permission from ref. 350. Copyright 2018, Nature Publishing Group.

Additionally, BFO itself can serve as the main photocatalyst, and its photocatalystic efficiency can be improved by combining with other materials, such as graphene.[349] Li *et al.* synthesized graphene–BFO nanocomposites by a one-pot hydrothermal method, where the band gap of the nanocomposites can be easily modulated into 1.78–2.24 eV by controlling the concentrated OH group.[349] Overall, the photovoltaic characteristics in the BFO-based composite photoelectrode under visible-light irradiation provide a promising tool to improve the photoelectrochemical water splitting and photoelectrocatalysis.

However, the interaction between BFO and degraded organics is not only revealed by the photovoltaic effect of BFO on organics, but also reflected by the aqueous solution modulation on the ferroelectric polarization of BFO. In the BFO/$(La,Sr)MnO_3/SrTiO_3$ structures, the internal ferroelectric polarization of the BFO layer can be switched using Milli-Q water (PH = 7) and acidic solution (PH = 3), which is in contact with the surface of BFO, as shown in Fig. 39.[350] Moreover, the ferroelectric polarization of BFO can be cyclically switched upward and downward by the aqueous solution at different PH values (Fig. 40d), which enables an erasable type-printing polarization of BFO. As seen in Fig. 40e, the initially upward polarization of BFO turns into downward polarization by the acidic solution. Then, a pattern is coated on the surface of BFO by photoengraving, where the polarization of the patterned BFO region is reversed upward by exposed to Milli-Q water. After removing the photoresist, Chinese characteristic water is successfully printed by the tunable ferroelectric polarization of BFO. Moreover, owing to the reversible PH-tailored polarization switching of BFO, the printed character becomes erasable. The water-modulated ferroelectric polarization of BFO offers opportunities to develop multifunctional catalysis, which also paves a new way to utilize green energy.

V. Conclusion and outlook

This review offers a comprehensive review of BFO-based heterostructures, where the materials, properties and applications are reviewed, respectively. The morphologies of BFO and medium materials in the heterostructures stimulate novel optical, electrical, magnetic and valley characteristics. In particular, these properties are connected with each other, which clarifies the mechanism behind the photovoltaic effect, electric

field control of magnetism, RS and valley characteristics, as shown in Fig. 1. Moreover, the novel physical properties of the BFO-based heterostructures enable two main kinds of applications: one is the nonvolatile data storage and logic switching with a BFO ferroelectric barrier and the other is the photoelectrochemical water splitting and photocatalysis with the BFO photoelectrodes. These glorious properties and applications in BFO-based heterostructures provide a way for developing efficient data storage and integrated multifunctional devices in the future. Nevertheless, the physical properties of the BFO-based heterostructures have not been explored sufficiently, which mainly focus on the domain-, phase transition- and valley-related properties:

(i) The ferroelectric polarization and domain structure of BFO are crucial for the photovoltaic effect and resistance states in related heterostructures and junctions. Different from the ferroelectric polarization induced depolarization field, the ferroelectric domain walls of BFO films have an extra electrostatic potential to separate the photo-generated charge carrier,[187] which can result in an above-bandgap voltage.[60] Moreover, the domain-dependent above-band-gap photovoltaic response of BFO is tunable by an electric field.[191] It is noted that the domain walls become a new index to modulate the photovoltaic effects. However, many special characteristics have been induced in the domain walls of BFO. The charged domain walls have been stimulated by gathering the free charges, which can produce a large conductance[277] and RS.[225] The anisotropic ferroelectric domain walls have been observed in BFO films,[197] where the tail-to-tail domain walls are more conductive than the head-to-head or head-to-tail domain walls. So, we suppose that the engineered charged domain walls and anisotropic domain structure can be used to induce novel photovoltaic effects in the BFO-based heterostructures.

Besides, the ferroelectric topological textures have been demonstrated in epitaxial BFO square nanoplates at a large strain gradient of 10^5 m^{-1}, along with the vortices and antivortices.[351] The net number of vortices in the BFO nanoplates is tunable by selective domain switching.[351] Moreover, the topologically confined ferroelectric domain walls have been demonstrated in self-assembled BFO nanoislands.[277] So, the ferroelectric topological textures and mechanism should be addressed in the self-assembled BFO-based nanostructures. Owing to the advanced fabrication methods, tunable BFO self-assembled nanostructures have been fabricated successfully.[96,101,103]

(ii) The phase transition of BFO is able to affect the ferroelectric polarization and RS of the heterostructures.[61] However, in the BFO/$La_{2/3}Sr_{1/3}MnO_3$ heterostructures,[225] initial R-phase BFO can transform into the T phase (Fig. 26h) at the locally charged domain wall boundaries. So, the phase transition of BFO should be tailored by engineering the charged domain walls, which can affect the RS in the heterostructures.

(iii) Valley-related photovoltaic characteristics of the (111)-oriented bilayered R-BFO-based heterostructures have been investigated by theoretical and experimental means. The fabrication of the (111)-oriented perovskite oxide superlattices has reached the atomic level.[352] The (111)-oriented $Ca_{0.5}Sr_{0.5}IrO_3$/$SrTiO_3$ superlattices have been grown by pulsed laser deposition,[353] and (111)-oriented $(LaNiO_3)_n$/$(LaMnO_3)_m$ superlattices were fabricated by off-axis radiofrequency magnetron sputtering.[354] The $(BFO)_2$/$(SrTiO_3)_4$ superlattices also were successfully fabricated by pulsed laser deposition.[69] These advanced fabrication methods offer opportunities for future experimental work on BFO-based superlattices with novel valley–spin characteristics.

Conflicts of interest

There are no conflicts to declare.

Acknowledgements

This work is supported by the National Natural Science Foundation of China (51871161, 51671142, and U1632152), and the Key Project of the Natural Science Foundation of Tianjin (16JCZDJC37300).

References

1 J. Neaton, C. Ederer, U. Waghmare, N. Spaldin and K. Rabe, *Phys. Rev. B: Condens. Matter Mater. Phys.*, 2005, **71**, 014113.
2 G. Catalan and J. F. Scott, *Adv. Mater.*, 2009, **21**, 2463–2485.
3 Y. H. Hsieh, F. Xue, T. Yang, H. J. Liu, Y. Zhu, Y. C. Chen, Q. Zhan, C. G. Duan, L. Q. Chen, Q. He and Y. H. Chu, *Nat. Commun.*, 2016, **7**, 13199.
4 J. Heron, D. Schlom and R. Ramesh, *Appl. Phys. Rev.*, 2014, **1**, 021303.
5 D. Mazumdar, V. Shelke, M. Iliev, S. Jesse, A. Kumar, S. V. Kalinin, A. P. Baddorf and A. Gupta, *Nano Lett.*, 2010, **10**, 2555–2561.
6 Y. Wu, X. Han and H. Huang, *J. Phys. Chem. C*, 2018, **122**, 6852–6857.
7 J. F. Scott and J. Gardner, *Mater. Today*, 2018, **21**, 553–562.
8 D. I. Khomskii, *J. Magn. Magn. Mater.*, 2006, **306**, 1–8.
9 R. Seshadri and N. A. Hill, *Chem. Mater.*, 2001, **13**, 2892–2899.
10 J. Wang, J. B. Neaton, H. Zheng, V. Nagarajan, S. B. Ogale, B. Liu, D. Viehland, V. Vaithyanathan, D. G. Schlom, U. V. Waghmare, N. A. Spaldin, K. M. Rabe, M. Wuttig and R. Ramesh, *Science*, 2003, **299**, 1719–1722.
11 W. Ratcliff, D. Kan, W. Chen, S. Watson, S. Chi, R. Erwin, G. J. McIntyre, S. C. Capelli and I. Takeuchi, *Adv. Funct. Mater.*, 2011, **21**, 1567–1574.
12 B. Xu, B. Dupé, C. Xu, H. Xiang and L. Bellaiche, *Phys. Rev. B*, 2018, **98**, 184420.
13 I. Sosnowska, T. Peterlin-Neumaier and E. Steichele, *J. Phys. C: Solid State Phys.*, 1982, **15**, 4835–4846.

14 A. Agbelele, D. Sando, C. Toulouse, C. Paillard, R. D. Johnson, R. Ruffer, A. F. Popkov, C. Carretero, P. Rovillain, J. M. Le Breton, B. Dkhil, M. Cazayous, Y. Gallais, M. A. Measson, A. Sacuto, P. Manuel, A. K. Zvezdin, A. Barthelemy, J. Juraszek and M. Bibes, *Adv. Mater.*, 2017, **29**, 1602327.
15 J. Herrero-Albillos, G. Catalan, J. A. Rodriguez-Velamazan, M. Viret, D. Colson and J. F. Scott, *J. Phys.: Condens. Matter*, 2010, **22**, 256001.
16 D. Lebeugle, A. Mougin, M. Viret, D. Colson and L. Ranno, *Phys. Rev. Lett.*, 2009, **103**, 257601.
17 M. K. Singh, R. S. Katiyar and J. F. Scott, *J. Phys.: Condens. Matter*, 2008, **20**, 252203.
18 B. Ruette, S. Zvyagin, A. P. Pyatakov, A. Bush, J. F. Li, V. I. Belotelov, A. K. Zvezdin and D. Viehland, *Phys. Rev. B: Condens. Matter Mater. Phys.*, 2004, **69**, 064114.
19 H. M. Jang, H. Han and J. H. Lee, *Sci. Rep.*, 2018, **8**, 405.
20 C. Lu, W. Hu, Y. Tian and T. Wu, *Appl. Phys. Rev.*, 2015, **2**, 021304.
21 R. Huang, H.-C. Ding, W.-I. Liang, Y.-C. Gao, X.-D. Tang, Q. He, C.-G. Duan, Z. Zhu, J. Chu, C. A. J. Fisher, T. Hirayama, Y. Ikuhara and Y.-H. Chu, *Adv. Funct. Mater.*, 2014, **24**, 793–799.
22 Z. Chen, Z. Luo, C. Huang, Y. Qi, P. Yang, L. You, C. Hu, T. Wu, J. Wang, C. Gao, T. Sritharan and L. Chen, *Adv. Funct. Mater.*, 2011, **21**, 133–138.
23 Z. Cheng and X. Wang, *Phys. Rev. B: Condens. Matter Mater. Phys.*, 2007, **75**, 172406.
24 P. Chen, N. Podraza, X. Xu, A. Melville, E. Vlahos, V. Gopalan, R. Ramesh, D. G. Schlom and J. Musfeldt, *Appl. Phys. Lett.*, 2010, **96**, 131907.
25 R. J. Zeches, M. D. Rossell, J. X. Zhang, A. J. Hatt, Q. He, C. H. Yang, A. Kumar, C. H. Wang, A. Melville, C. Adamo, G. Sheng, Y. H. Chu, J. F. Ihlefeld, R. Erni, C. Ederer, V. Gopalan, L. Q. Chen, D. G. Schlom, N. A. Spaldin, L. W. Martin and R. Ramesh, *Science*, 2009, **326**, 977–980.
26 A. Hatt and N. Spaldin, *Phys. Rev. B: Condens. Matter Mater. Phys.*, 2010, **81**, 054109.
27 L. Martin, S. Crane, Y. Chu, M. Holcomb, M. Gajek, M. Huijben, C. Yang, N. Balke and R. Ramesh, *J. Phys.: Condens. Matter*, 2008, **20**, 434220.
28 D. Ricinschi, K. Y. Yun and M. Okuyama, *J. Phys.: Condens. Matter*, 2006, **18**, L97–L105.
29 A. R. Damodaran, C. W. Liang, Q. He, C. Y. Peng, L. Chang, Y. H. Chu and L. W. Martin, *Adv. Mater.*, 2011, **23**, 3170–3175.
30 P. Yu, J. S. Lee, S. Okamoto, M. D. Rossell, M. Huijben, C. H. Yang, Q. He, J. X. Zhang, S. Y. Yang, M. J. Lee, Q. M. Ramasse, R. Erni, Y. H. Chu, D. A. Arena, C. C. Kao, L. W. Martin and R. Ramesh, *Phys. Rev. Lett.*, 2010, **105**, 027201.
31 H. Y. Hwang, Y. Iwasa, M. Kawasaki, B. Keimer, N. Nagaosa and Y. Tokura, *Nat. Mater.*, 2012, **11**, 103–113.
32 L. Yin, X. Wang and W. Mi, *ACS Appl. Mater. Interfaces*, 2018, **10**, 3822–3829.
33 S. M. Young, F. Zheng and A. M. Rappe, *Phys. Rev. Lett.*, 2012, **109**, 236601.
34 T. Choi, S. Lee, Y. Choi, V. Kiryukhin and S. Cheong, *Science*, 2009, **324**, 63–66.
35 A. Zhu, Q. Zhao, X. Li and Y. Shi, *ACS Appl. Mater. Interfaces*, 2014, **6**, 671–679.
36 S. Chatterjee, A. Bera and A. J. Pal, *ACS Appl. Mater. Interfaces*, 2014, **6**, 20479–20486.
37 W. J. Hu, Z. Wang, W. Yu and T. Wu, *Nat. Commun.*, 2016, **7**, 10808.
38 A. Mukherjee, S. Chakrabarty, N. Kumari, W. N. Su and S. Basu, *ACS Omega*, 2018, **3**, 5946–5957.
39 Y. Ren, F. Nan, L. You, Y. Zhou, Y. Wang, J. Wang, X. Su, M. Shen and L. Fang, *Small*, 2017, **13**, 1603457.
40 B. Xu, D. Wang, H. J. Zhao, J. Íñiguez, X. M. Chen and L. Bellaiche, *Adv. Funct. Mater.*, 2015, **25**, 3626–3633.
41 C. Daumont, J. Wolfman, C. Autret-Lambert, P. Andreazza and B. Negulescu, *Appl. Phys. Lett.*, 2018, **112**, 112401.
42 C. Song, B. Cui, F. Li, X. Zhou and F. Pan, *Prog. Mater. Sci.*, 2017, **87**, 33–82.
43 Y. H. Chu, L. W. Martin, M. B. Holcomb, M. Gajek, S. J. Han, Q. He, N. Balke, C. H. Yang, D. Lee, W. Hu, Q. Zhan, P. L. Yang, A. Fraile-Rodriguez, A. Scholl, S. X. Wang and R. Ramesh, *Nat. Mater.*, 2008, **7**, 478–482.
44 Y. Chu, L. Martin, M. Holcomb and R. Ramesh, *Mater. Today*, 2017, **10**, 16–23.
45 L. Yin, W. Mi and X. Wang, *Phys. Rev. Appl.*, 2016, **6**, 064022.
46 L. Yin, X. Wang and W. Mi, *ACS Appl. Mater. Interfaces*, 2017, **9**, 15887–15892.
47 L. Yin, W. Mi and X. Wang, *Appl. Phys. Lett.*, 2017, **111**, 032404.
48 J.-M. Hu, C.-G. Duan, C.-W. Nan and L.-Q. Chen, *npj Comput. Mater.*, 2017, **3**, 18.
49 J. T. Heron, M. Trassin, K. Ashraf, M. Gajek, Q. He, S. Y. Yang, D. E. Nikonov, Y. H. Chu, S. Salahuddin and R. Ramesh, *Phys. Rev. Lett.*, 2011, **107**, 217202.
50 L. You, C. Lu, P. Yang, G. Han, T. Wu, U. Luders, W. Prellier, K. Yao, L. Chen and J. Wang, *Adv. Mater.*, 2010, **22**, 4964–4968.
51 T. Gao, X. Zhang, W. Ratcliff, S. Maruyama, M. Murakami, A. Varatharajan, Z. Yamani, P. Chen, K. Wang, H. Zhang, R. Shull, L. A. Bendersky, J. Unguris, R. Ramesh and I. Takeuchi, *Nano Lett.*, 2017, **17**, 2825–2832.
52 P. B. Meisenheimer, S. Novakov, N. M. Vu and J. T. Heron, *J. Appl. Phys.*, 2018, **123**, 240901.
53 B. Sun, Y. Liu, W. Zhao and P. Chen, *RSC Adv.*, 2015, **5**, 13513–13518.
54 J. Luo, S. Lin, Y. Zheng and B. Wang, *Appl. Phys. Lett.*, 2012, **101**, 062902.
55 H. Yamada, V. Garcia, S. Fusil, S. Boyn, M. Marinova, A. Gloter, S. Xavier, J. Grollier, E. Jacquet, C. Carretero, C. Deranlot, M. Bibes and A. Barthelemy, *ACS Nano*, 2013, **7**, 5385–5390.
56 J. P. Velev, J. D. Burton, M. Y. Zhuravlev and E. Y. Tsymbal, *npj Comput. Mater.*, 2016, **2**, 16009.

57 Y. Liu, Y. Yin, S. Dong, S. Yang, T. Jiang and X. Li, *Appl. Phys. Lett.*, 2014, **104**, 043507.
58 Z. Zhang, P. Wu, L. Chen and J. Wang, *Appl. Phys. Lett.*, 2011, **99**, 062902.
59 L. Yin, W. Mi and X. Wang, *J. Mater. Chem. C*, 2015, **3**, 11066–11075.
60 H. Mai, T. Lu, Q. Li, Z. Liu, Y. Li, F. Kremer, L. Li, R. L. Withers, H. Wen and Y. Liu, *ACS Appl. Mater. Interfaces*, 2018, **10**, 12781–12789.
61 C. Chiu, C. Huang, Y. Hsieh, J. Chen, C. Chang, Y. Chu and W. Wu, *Nano Energy*, 2017, **34**, 103–110.
62 T. Zhao, A. Scholl, F. Zavaliche, K. Lee, M. Barry, A. Doran, M. P. Cruz, Y. H. Chu, C. Ederer, N. A. Spaldin, R. R. Das, D. M. Kim, S. H. Baek, C. B. Eom and R. Ramesh, *Nat. Mater.*, 2006, **5**, 823–829.
63 J. Wang, A. Scholl, H. Zheng, S. B. Ogale, D. Viehland, D. G. Schlom, N. A. Spaldin, K. M. Rabe, M. Wuttig, L. Mohaddes, J. B. Neaton, U. Waghmare, T. Zhao and R. Ramesh, *Science*, 2005, **307**, 1203b.
64 J. X. Zhang, Q. He, M. Trassin, W. Luo, D. Yi, M. D. Rossell, P. Yu, L. You, C. H. Wang, C. Y. Kuo, J. T. Heron, Z. Hu, R. J. Zeches, H. J. Lin, A. Tanaka, C. T. Chen, L. H. Tjeng, Y. H. Chu and R. Ramesh, *Phys. Rev. Lett.*, 2011, **107**, 147602.
65 J.-Q. Dai, T.-F. Cao and X.-W. Wang, *J. Phys. Chem. C*, 2018, **122**, 17250–17260.
66 B. C. Huang, P. Yu, Y. H. Chu, C. S. Chang, R. Ramesh, R. E. Dunin-Borkowski, P. Ebert and Y. P. Chiu, *ACS Nano*, 2018, **12**, 1089–1095.
67 P. Yu, W. Luo, D. Yi, J. Zhang, M. Rossell, C. Yang, L. You, G. Singh-Bhalla, S. Yang, Q. He, Q. Ramassed, R. Erni, L. Martin, Y. Chu, S. Pantelides, S. Pennycook and R. Ramesh, *Proc. Natl. Acad. Sci. U. S. A.*, 2012, **109**, 9710–9715.
68 Y. M. Kim, A. Kumar, A. Hatt, A. N. Morozovska, A. Tselev, M. D. Biegalski, I. Ivanov, E. A. Eliseev, S. J. Pennycook, J. M. Rondinelli, S. V. Kalinin and A. Y. Borisevich, *Adv. Mater.*, 2013, **25**, 2497–2504.
69 E. Bruyer, A. Sayede, A. Ferri, R. Desfeux, R. Mangalam, R. Ranjith and W. Prellier, *Appl. Phys. Lett.*, 2015, **107**, 042904.
70 T. Amrillah, Y. Bitla, K. Shin, T. Yang, Y. H. Hsieh, Y. Y. Chiou, H. J. Liu, T. H. Do, D. Su, Y. C. Chen, S. U. Jen, L. Q. Chen, K. H. Kim, J. Y. Juang and Y. H. Chu, *ACS Nano*, 2017, **11**, 6122–6130.
71 M. Guo, G. Tan, W. Yang, L. Lv, M. Xue, Y. Liu, H. Ren and A. Xia, *Mater. Lett.*, 2018, **228**, 13–16.
72 A. R. Akbashev, G. Chen and J. E. Spanier, *Nano Lett.*, 2014, **14**, 44–49.
73 S. Ikeda, J. Hayakawa, Y. Lee, F. Matsukura, Y. Ohno and T. Hanyu, *IEEE Trans. Electron Devices*, 2007, **54**, 991–1002.
74 W. G. Wang, M. Li, S. Hageman and C. L. Chien, *Nat. Mater.*, 2011, **11**, 64–68.
75 G. Yu, P. Upadhyaya, Y. Fan, J. G. Alzate, W. Jiang, K. L. Wong, S. Takei, S. A. Bender, L. T. Chang, Y. Jiang, M. Lang, J. Tang, Y. Wang, Y. Tserkovnyak, P. K. Amiri and K. L. Wang, *Nat. Nanotechnol.*, 2014, **9**, 548–554.
76 G. Catalan, J. Seidel, R. Ramesh and J. Scott, *Rev. Mod. Phys.*, 2012, **84**, 119–156.
77 Y. Kim, A. Kumar, A. Tselev, I. I. Kravchenko, H. Han, I. Vrejoiu, W. Lee, D. Hesse, M. Alexe, S. V. Kalinin and S. Jesse, *ACS Nano*, 2011, **5**, 9104–9112.
78 M. F. Chisholm, W. Luo, M. P. Oxley, S. T. Pantelides and H. N. Lee, *Phys. Rev. Lett.*, 2010, **105**, 197602.
79 C. Lichtensteiger, J. M. Triscone, J. Junquera and P. Ghosez, *Phys. Rev. Lett.*, 2005, **94**, 047603.
80 M. Trieloff, E. K. Jessberger, I. Herrwerth, J. Hopp, C. Fieni, M. Ghelis, M. Bourot-Denise and P. Pellas, *Nature*, 2003, **422**, 502–506.
81 M. Marinova, J. E. Rault, A. Gloter, S. Nemsak, G. K. Palsson, J. P. Rueff, C. S. Fadley, C. Carretero, H. Yamada, K. March, V. Garcia, S. Fusil, A. Barthelemy, O. Stephan, C. Colliex and M. Bibes, *Nano Lett.*, 2015, **15**, 2533–2541.
82 Y. Liu, Y. L. Zhu, Y. L. Tang, Y. J. Wang, Y. X. Jiang, Y. B. Xu, B. Zhang and X. L. Ma, *Nano Lett.*, 2017, **17**, 3619–3628.
83 J. Zhuang, A. A. Bokov, N. Zhang, J. Zhang, J. Zhao, S. Yang, W. Ren and Z.-G. Ye, *Cryst. Growth Des.*, 2018, **18**, 4503–4510.
84 B. Carcan, H. Bouyanfif, M. El Marssi, F. Le Marrec, L. Dupont, C. Davoisne, J. Wolfman and D. C. Arnold, *J. Appl. Phys.*, 2018, **124**, 044105.
85 D. Duraisamy and G. N. Venkatesan, *Appl. Phys. Lett.*, 2018, **112**, 052903.
86 Z. Fan, K. Yao and J. Wang, *Appl. Phys. Lett.*, 2014, **105**, 162903.
87 R. Katiyar, P. Misra, F. Mendoza, G. Morell and R. Katiyar, *Appl. Phys. Lett.*, 2014, **105**, 142902.
88 Y. Zang, D. Xie, X. Wu, Y. Chen, Y. Lin, M. Li, H. Tian, X. Li, Z. Li, H. Zhu, T. Ren and D. Plant, *Appl. Phys. Lett.*, 2011, **99**, 132904.
89 M. Bagherzadeh and R. Kaveh, *J. Photochem. Photobiol., A*, 2018, **359**, 11–22.
90 S. Goswami, D. Bhattacharya, C. K. Ghosh, B. Ghosh, S. D. Kaushik, V. Siruguri and P. S. R. Krishna, *Sci. Rep.*, 2018, **8**, 3728.
91 A. Sarkar, G. Khan, A. Chaudhuri, A. Das and K. Mandal, *Appl. Phys. Lett.*, 2016, **108**, 033112.
92 A. N. Morozovska, E. A. Eliseev, M. D. Glinchuk, O. M. Fesenko, V. V. Shvartsman, V. Gopalan, M. V. Silibin and D. V. Karpinsky, *Phys. Rev. B*, 2018, **97**, 134115.
93 P. Chen, X. Xu, C. Koenigsmann, A. C. Santulli, S. S. Wong and J. L. Musfeldt, *Nano Lett.*, 2010, **10**, 4526–4532.
94 F. Huang, X. Xu, X. Lu, M. Zhou, H. Sang and J. Zhu, *Sci. Rep.*, 2018, **8**, 2311.
95 H. K. Choi, N. M. Aimon, D. H. Kim, X. Y. Sun, J. Gwyther, I. Manners and C. A. Ross, *ACS Nano*, 2014, **8**, 9248–9254.
96 R. Comes, H. Liu, M. Khokhlov, R. Kasica, J. Lu and S. A. Wolf, *Nano Lett.*, 2012, **12**, 2367–2373.

97 A. Imai, X. Cheng, H. L. Xin, E. A. Eliseev, A. N. Morozovska, S. V. Kalinin, R. Takahashi, M. Lippmaa, Y. Matsumoto and V. Nagarajan, *ACS Nano*, 2013, **7**, 11079–11086.
98 Y.-H. Hsieh, E. Strelcov, J.-M. Liou, C.-Y. Shen, Y.-C. Chen, S. V. Kalinin and Y.-H. Chu, *ACS Nano*, 2013, **7**, 8627–8633.
99 E. Strelcov, A. Belianinov, Y.-H. Hsieh, S. Jesse, A. P. Baddorf, Y.-H. Chu and S. V. Kalinin, *ACS Nano*, 2014, **8**, 6449–6457.
100 F. Zavaliche, H. Zheng, L. Mohaddes-Ardabili, S. Y. Yang, Q. Zhan, P. Shafer, E. Reilly, R. Chopdekar, Y. Jia, P. Wright, D. G. Schlom, Y. Suzuki and R. Ramesh, *Nano Lett.*, 2005, **5**, 1793–1796.
101 H. Zheng, F. Straub, Q. Zhan, P. L. Yang, W. K. Hsieh, F. Zavaliche, Y. H. Chu, U. Dahmen and R. Ramesh, *Adv. Mater.*, 2006, **18**, 2747–2752.
102 S. Hong, T. Choi, J. H. Jeon, Y. Kim, H. Lee, H. Y. Joo, I. Hwang, J. S. Kim, S. O. Kang, S. V. Kalinin and B. H. Park, *Adv. Mater.*, 2013, **25**, 2339–2343.
103 S. M. Stratulat, X. Lu, A. Morelli, D. Hesse, W. Erfurth and M. Alexe, *Nano Lett.*, 2013, **13**, 3884–3889.
104 G. Tian, F. Zhang, J. Yao, H. Fan, P. Li, Z. Li, X. Song, X. Zhang, M. Qin, M. Zeng, Z. Zhang, J. Yao, X. Gao and J. Liu, *ACS Nano*, 2016, **10**, 1025–1032.
105 S. Ojha, W. C. Nunes, N. M. Aimon and C. A. Ross, *ACS Nano*, 2016, **10**, 7657–7664.
106 M. A. K. Budi, E. B. Glass, N. G. Rudawski and J. S. Andrew, *J. Mater. Chem. C*, 2017, **5**, 8586–8592.
107 Y. H. Hsieh, J. M. Liou, B. C. Huang, C. W. Liang, Q. He, Q. Zhan, Y. P. Chiu, Y. C. Chen and Y. H. Chu, *Adv. Mater.*, 2012, **24**, 4564–4568.
108 D. H. Kim, N. M. Aimon, X. Y. Sun, L. Kornblum, F. J. Walker, C. H. Ahn and C. A. Ross, *Adv. Funct. Mater.*, 2014, **24**, 5889–5896.
109 H. D. Song, Y. F. Wu, X. Yang, Z. Ren, X. Ke, M. Kurttepeli, G. V. Tendeloo, D. Liu, H. C. Wu, B. Yan, X. Wu, C. G. Duan, G. Han, Z. M. Liao and D. Yu, *Nano Lett.*, 2018, **18**, 2435–2441.
110 D. Moitra, C. Anand, B. K. Ghosh, M. Chandel and N. N. Ghosh, *ACS Appl. Energy Mater.*, 2018, **1**, 464–474.
111 M. Campanini, R. Erni, C. H. Yang, R. Ramesh and M. D. Rossell, *Nano Lett.*, 2018, **18**, 717–724.
112 S. Gupta, M. Tomar and V. Gupta, *J. Appl. Phys.*, 2014, **115**, 014102.
113 Y.-H. Lee, J.-M. Wu and C.-H. Lai, *Appl. Phys. Lett.*, 2006, **88**, 042903.
114 B. Yu, M. Li, Z. Hu, L. Pei, D. Guo, X. Zhao and S. Dong, *Appl. Phys. Lett.*, 2008, **93**, 182909.
115 P. Kharel, S. Talebi, B. Ramachandran, A. Dixit, V. M. Naik, M. B. Sahana, C. Sudakar, R. Naik, M. S. Rao and G. Lawes, *J. Phys.: Condens. Matter*, 2009, **21**, 036001.
116 Y. Wang and C.-W. Nan, *Appl. Phys. Lett.*, 2006, **89**, 052903.
117 M. Guo, G. Tan, Y. Zheng, W. Liu, H. Ren and A. Xia, *J. Appl. Phys.*, 2017, **121**, 175303.
118 W. M. Lee, J. H. Sung, K. Chu, X. Moya, D. Lee, C. J. Kim, N. D. Mathur, S. W. Cheong, C. H. Yang and M. H. Jo, *Adv. Mater.*, 2012, **24**, OP49–OP53.
119 J. Gebhardt and A. M. Rappe, *Phys. Rev. B*, 2018, **98**, 125202.
120 B. Kundys, *Appl. Phys. Rev.*, 2015, **2**, 011301.
121 L. Zhang, J. Chen, J. Cao, D. Hea and X. Xing, *J. Mater. Chem. C*, 2015, **3**, 4706–4712.
122 S. Gupta, R. Medwal, T. Limbu, R. Katiyar, S. Pavunny, M. Tomar, G. Morell, V. Gupta and R. Katiyar, *Appl. Phys. Lett.*, 2015, **107**, 062902.
123 R. Nechache, C. Harnagea, S. Li, L. Cardenas, W. Huang, J. Chakrabartty and F. Rosei, *Nat. Photonics*, 2014, **9**, 61–67.
124 G. Lotey and N. Verma, *Chem. Phys. Lett.*, 2013, **574**, 71–77.
125 A. Tsurumaki, H. Yamada and A. Sawa, *Adv. Funct. Mater.*, 2012, **22**, 1040–1047.
126 L. Li, Y. Zhang, L. Xie, J. R. Jokisaari, C. Beekman, J. C. Yang, Y. H. Chu, H. M. Christen and X. Pan, *Nano Lett.*, 2017, **17**, 3556–3562.
127 B. Gao, L. Lin, C. Chen, L. Wei, J. Wang, B. Xu, C. Li, J. Bian, S. Dong, J. Du and Q. Xu, *Phys. Rev. Mater.*, 2018, **2**, 084401.
128 L. Wang, H. Ma, L. Chang, C. Ma, G. Yuan, J. Wang and T. Wu, *Small*, 2017, **13**, 1602355.
129 M. Li, F. Zhuge, X. Zhu, K. Yin, J. Wang, Y. Liu, C. He, B. Chen and R. W. Li, *Nanotechnology*, 2010, **21**, 425202.
130 Y. Lin, Z. Yan, X. Lu, Z. Lu, M. Zeng, Y. Chen, X. Gao, J. Wan, J. Dai and J. Liu, *Appl. Phys. Lett.*, 2014, **104**, 143503.
131 T. You, X. Ou, G. Niu, F. Barwolf, G. Li, N. Du, D. Burger, I. Skorupa, Q. Jia, W. Yu, X. Wang, O. G. Schmidt and H. Schmidt, *Sci. Rep.*, 2015, **5**, 18623.
132 Z. Lu, P. Li, J. G. Wan, Z. Huang, G. Tian, D. Pan, Z. Fan, X. Gao and J. M. Liu, *ACS Appl. Mater. Interfaces*, 2017, **9**, 27284–27289.
133 F. Fan, M. Duan, B. Luo and C. Chen, *Chin. J. Phys.*, 2018, **56**, 1903–1908.
134 H. Zhang, S. Cheng, B. Li, X. Cheng and Q. Cheng, *Sep. Purif. Technol.*, 2018, **202**, 242–247.
135 C. Zhao, C. Zhou and C. Chen, *Physica B*, 2017, **521**, 376–380.
136 N. Feng, W. Mi, X. Wang, Y. Cheng and U. Schwingenschlogl, *ACS Appl. Mater. Interfaces*, 2015, **7**, 10612–10616.
137 L. Yin, Q. Zhang, W. Mi and X. Wang, *J. Appl. Phys.*, 2016, **120**, 165303.
138 A. Lahmar, *J. Magn. Magn. Mater.*, 2017, **439**, 30–37.
139 C. A. Vaz, J. Hoffman, C. H. Ahn and R. Ramesh, *Adv. Mater.*, 2010, **22**, 2900–2918.
140 C. Wang, L. Zhou, Q. Fu, Y. Tian, S. Wang, H. Gou, J. Ai, L. Zhang and F. Xue, *J. Magn. Magn. Mater.*, 2018, **449**, 372–377.
141 C. Chen, L. Guo, C. Li, B. Gao, R. Zheng, J. Wang, Q. Li, J. Du and Q. Xu, *J. Magn. Magn. Mater.*, 2018, **464**, 156–160.

142 H. Bea, M. Bibes, F. Ott, B. Dupe, X. H. Zhu, S. Petit, S. Fusil, C. Deranlot, K. Bouzehouane and A. Barthelemy, *Phys. Rev. Lett.*, 2008, **100**, 017204.
143 J. D. Shen, W. B. Yang, A. Kumar, H. H. Zhao, Y. J. Lai, L. S. Feng, Q. Y. Xu, Y. Q. Zhang, J. Du and Q. Li, *J. Magn. Magn. Mater.*, 2018, **451**, 734–736.
144 A. Aftabi and M. M. Tehranchi, *J. Alloys Compd.*, 2018, **766**, 1054–1060.
145 S. Kokado, N. Fujima, K. Harigaya, H. Shimizu and A. Sakuma, *Phys. Rev. B: Condens. Matter Mater. Phys.*, 2006, **73**, 172410.
146 K. Sunaga, M. Tsunoda, K. Komagaki, Y. Uehara and M. Takahashi, *J. Appl. Phys.*, 2007, **102**, 013917.
147 L. Yin, X. Wang and W. Mi, *J. Appl. Phys.*, 2018, **123**, 033905.
148 Y. Huang, S. Li, Z. Tian, W. Liang, J. Wang, X. Li, X. Cheng, J. He and J. Liu, *J. Alloys Compd.*, 2018, **762**, 438–443.
149 S. Kuila, S. Tiwary, M. R. Sahoo, A. Barik and P. N. Vishwakarma, *J. Appl. Phys.*, 2018, **124**, 154104.
150 F. Zavaliche, T. Zhao, H. Zheng, F. Straub, M. Cruz, P. Yang, D. Hao and R. Ramesh, *Nano Lett.*, 2007, **7**, 1586–1590.
151 Z. Wang, Y. Yang, R. Viswan, J. Li and D. Viehland, *Appl. Phys. Lett.*, 2011, **99**, 043110.
152 R. Barman and D. Kaur, *Appl. Phys. Lett.*, 2016, **108**, 092404.
153 S. Chen, D. Wang, Z. Han, C. Zhang, Y. Du and Z. Huang, *Appl. Phys. Lett.*, 2009, **95**, 022501.
154 Q. Zhang, L. You, X. Shen, C. Wan, Z. Yuan, X. Zhang, L. Huang, W. Kong, H. Wu, R. Yu, J. Wang and X. Han, *Adv. Mater.*, 2015, **27**, 6934–6938.
155 P. P. Biswas, C. Thirmal, S. Pal and P. Murugavel, *J. Appl. Phys.*, 2018, **123**, 024101.
156 C. Chen, S. Lv, J. Li, Z. Wang, X. Liang, Y. Li, D. Viehland, K. Nakajima and Y. Ikuhara, *Appl. Phys. Lett.*, 2015, **107**, 031601.
157 C. Cen, S. Thiel, J. Mannhart and J. Levy, *Science*, 2009, **323**, 1026–1030.
158 Y. Z. Chen, F. Trier, T. Wijnands, R. J. Green, N. Gauquelin, R. Egoavil, D. V. Christensen, G. Koster, M. Huijben, N. Bovet, S. Macke, F. He, R. Sutarto, N. H. Andersen, J. A. Sulpizio, M. Honig, G. E. Prawiroatmodjo, T. S. Jespersen, S. Linderoth, S. Ilani, J. Verbeeck, G. Van Tendeloo, G. Rijnders, G. A. Sawatzky and N. Pryds, *Nat. Mater.*, 2015, **14**, 801–807.
159 S. Sharma, M. Tomar, A. Kumar, N. K. Puri and V. Gupta, *RSC Adv.*, 2016, **6**, 59150–59154.
160 S. Sharma, M. Tomar, A. Kumar, N. Puri and V. Gupta, *J. Appl. Phys.*, 2015, **118**, 074103.
161 Y. Hou, R. Han, W. Li, L. Luo and W. Fei, *Phys. Chem. Chem. Phys.*, 2018, **20**, 21917–21924.
162 J. K. Jochum, M. Lorenz, H. P. Gunnlaugsson, C. Patzig, T. Hoche, M. Grundmann, A. Vantomme, K. Temst, M. J. Van Bael and V. Lazenka, *Nanoscale*, 2018, **10**, 5574–5580.
163 T.-J. Park, G. C. Papaefthymiou, A. J. Viescas, Y. Lee, H. Zhou and S. S. Wong, *Phys. Rev. B: Condens. Matter Mater. Phys.*, 2010, **82**, 024431.
164 W. M. Zhu, H. Y. Guo and Z. G. Ye, *Phys. Rev. B: Condens. Matter Mater. Phys.*, 2008, **78**, 014401.
165 N. Wang, J. Cheng, A. Pyatakov, A. K. Zvezdin, J. F. Li, L. E. Cross and D. Viehland, *Phys. Rev. B: Condens. Matter Mater. Phys.*, 2005, **72**, 104434.
166 B. Chen, J. Shi, X. Zheng, Y. Zhou, K. Zhu and S. Priya, *J. Mater. Chem. A*, 2015, **3**, 7699–7705.
167 Y. Liu, S. Wang, Z. Chen and L. Xiao, *Sci. China Mater.*, 2016, **59**, 851–866.
168 P. Lopez-Varo, L. Bertoluzzi, J. Bisquert, M. Alexe, M. Coll, J. Huang, J. A. Jimenez-Tejada, T. Kirchartz, R. Nechache, F. Rosei and Y. Yuan, *Phys. Rep.*, 2016, **653**, 1–40.
169 S. Y. Yang, L. W. Martin, S. J. Byrnes, T. E. Conry, S. R. Basu, D. Paran, L. Reichertz, J. Ihlefeld, C. Adamo, A. Melville, Y. H. Chu, C. H. Yang, J. L. Musfeldt, D. G. Schlom, J. W. Ager and R. Ramesh, *Appl. Phys. Lett.*, 2009, **95**, 062909.
170 C. Paillard, X. Bai, I. C. Infante, M. Guennou, G. Geneste, M. Alexe, J. Kreisel and B. Dkhil, *Adv. Mater.*, 2016, **28**, 5153–5168.
171 F. Yan, G. Chen, L. Lu and J. E. Spanier, *ACS Nano*, 2012, **6**, 2353–2360.
172 F. Gao, Y. Yuan, K. Wang, X. Chen, F. Chen, J. Liu and F. Ren, *Appl. Phys. Lett.*, 2006, **89**, 102506.
173 C. Himcinschi, A. Bhatnagar, A. Talkenberger, M. Barchuk, D. R. T. Zahn, D. Rafaja, J. Kortus and M. Alexe, *Appl. Phys. Lett.*, 2015, **106**, 012908.
174 W. Ji, K. Yao and Y. C. Liang, *Adv. Mater.*, 2010, **22**, 1763–1766.
175 H. T. Yi, T. Choi, S. G. Choi, Y. S. Oh and S. W. Cheong, *Adv. Mater.*, 2011, **23**, 3403–3407.
176 D. Li, D. Zheng, C. Jin, W. Zheng and H. Bai, *ACS Appl. Mater. Interfaces*, 2018, **10**, 19836–19843.
177 V. M. Fridkin, *Crystallogr. Rep.*, 2001, **46**, 654–658.
178 L. Pintilie, I. Vrejoiu, G. Le Rhun and M. Alexe, *J. Appl. Phys.*, 2007, **101**, 064109.
179 Y. Yuan, Z. Xiao, B. Yang and J. Huang, *J. Mater. Chem. A*, 2014, **2**, 6027–6041.
180 J. Chakrabartty, R. Nechache, S. Li, M. Nicklaus, A. Ruediger, F. Rosei and D. D. Viehland, *J. Am. Ceram. Soc.*, 2014, **97**, 1837–1840.
181 B. Chen, M. Li, Y. Liu, Z. Zuo, F. Zhuge, Q. F. Zhan and R. W. Li, *Nanotechnology*, 2011, **22**, 195201.
182 D. J. Kim, J. Y. Jo, Y. S. Kim, Y. J. Chang, J. S. Lee, J. G. Yoon, T. K. Song and T. W. Noh, *Phys. Rev. Lett.*, 2005, **95**, 237602.
183 S. Zhang, H. Y. Xiao, S. M. Peng, G. X. Yang, Z. J. Liu, X. T. Zu, S. Li, D. J. Singh, L. W. Martin and L. Qiao, *Phys. Rev. Appl.*, 2018, **10**, 044004.
184 L. Qiao, S. Zhang, H. Y. Xiao, D. J. Singh, K. H. L. Zhang, Z. J. Liu, X. T. Zu and S. Li, *J. Mater. Chem. C*, 2018, **6**, 1239–1247.
185 C. Nie, S. Zhao, Y. Bai and Q. Lu, *Ceram. Int.*, 2016, **42**, 14036–14040.

186 X. Liu, F. Zhang, P. Long, T. Lu, H. Zeng, Y. Liu, R. L. Withers, Y. Li and Z. Yi, *Adv. Mater.*, 2018, **30**, 1801619.
187 S. Y. Yang, J. Seidel, S. J. Byrnes, P. Shafer, C. H. Yang, M. D. Rossell, P. Yu, Y. H. Chu, J. F. Scott, J. W. Ager 3rd, L. W. Martin and R. Ramesh, *Nat. Nanotechnol.*, 2010, **5**, 143–147.
188 D. Lee, S. H. Baek, T. H. Kim, J. G. Yoon, C. M. Folkman, C. B. Eom and T. W. Noh, *Phys. Rev. B: Condens. Matter Mater. Phys.*, 2011, **84**, 125305.
189 R. Guo, L. You, L. Chen, D. Wu and J. Wang, *Appl. Phys. Lett.*, 2011, **99**, 122902.
190 J. Seidel, D. Fu, S. Y. Yang, E. Alarcon-Llado, J. Wu, R. Ramesh and J. W. Ager, *Phys. Rev. Lett.*, 2011, **107**, 126805.
191 A. Bhatnagar, A. R. Chaudhuri, Y. H. Kim, D. Hesse and M. Alexe, *Nat. Commun.*, 2013, **4**, 3835.
192 P. Maksymovych, J. Seidel, Y. H. Chu, P. Wu, A. P. Baddorf, L. Q. Chen, S. V. Kalinin and R. Ramesh, *Nano Lett.*, 2011, **11**, 1906–1912.
193 A. Bhatnagar, Y. H. Kim, D. Hesse and M. Alexe, *Nano Lett.*, 2014, **14**, 5224–5228.
194 H. Zhu, Y. Yang, X. Meng, A. Jiang, Z. Bai, X. Zheng, L. Jin, C. Wang and S. Feng, *Appl. Phys. Lett.*, 2018, **112**, 182904.
195 D. Meier, J. Seidel, A. Cano, K. Delaney, Y. Kumagai, M. Mostovoy, N. A. Spaldin, R. Ramesh and M. Fiebig, *Nat. Mater.*, 2012, **11**, 284–288.
196 W. Wu, Y. Horibe, N. Lee, S. W. Cheong and J. R. Guest, *Phys. Rev. Lett.*, 2012, **108**, 077203.
197 Y. Jin, S. Xiao, J.-C. Yang, J. Zhang, X. Lu, Y.-H. Chu, S. W. Cheong, J. Li, Y. Kan, C. Yue, Y. Li, C. Ju, F. Huang and J. Zhu, *Appl. Phys. Lett.*, 2018, **113**, 082904.
198 J. H. Lee, I. Fina, X. Marti, Y. H. Kim, D. Hesse and M. Alexe, *Adv. Mater.*, 2014, **26**, 7078–7082.
199 M. M. Yang and M. Alexe, *Adv. Mater.*, 2018, **30**, e1704908.
200 Y. Li, C. Adamo, C. E. Rowland, R. D. Schaller, D. G. Schlom and D. A. Walko, *APL Mater.*, 2018, **6**, 084905.
201 S. Li, Y. Lin, B. Zhang, Y. Wang and C. Nan, *J. Phys. Chem. C*, 2010, **114**, 2903–2908.
202 Y. Li and D. J. Singh, *Phys. Rev. Mater.*, 2017, **1**, 075402.
203 W. Dong, Y. Guo, B. Guo, H. Li, H. Liu and T. W. Joel, *ACS Appl. Mater. Interfaces*, 2013, **5**, 6925–6929.
204 A. Gruverman, D. Wu, H. Lu, Y. Wang, H. W. Jang, C. M. Folkman, M. Y. Zhuravlev, D. Felker, M. Rzchowski, C. Eom and E. Y. Tsymbal, *Nano Lett.*, 2009, **9**, 3539–3543.
205 W. J. Hu, T. R. Paudel, S. Lopatin, Z. Wang, H. Ma, K. Wu, A. Bera, G. Yuan, A. Gruverman, E. Y. Tsymbal and T. Wu, *Adv. Funct. Mater.*, 2018, **28**, 1704337.
206 B. Kundys, M. Viret, D. Colson and D. O. Kundys, *Nat. Mater.*, 2010, **9**, 803.
207 T. Li, A. Lipatov, H. Lu, H. Lee, J. W. Lee, E. Torun, L. Wirtz, C. B. Eom, J. Iniguez, A. Sinitskii and A. Gruverman, *Nat. Commun.*, 2018, **9**, 3344.
208 J. M. Hu, L. Q. Chen and C. W. Nan, *Adv. Mater.*, 2016, **28**, 15–39.
209 S. S. Rao, J. T. Prater, F. Wu, C. T. Shelton, J. P. Maria and J. Narayan, *Nano Lett.*, 2013, **13**, 5814–5821.
210 S. M. Wu, S. A. Cybart, P. Yu, M. D. Rossell, J. X. Zhang, R. Ramesh and R. C. Dynes, *Nat. Mater.*, 2010, **9**, 756–761.
211 J. Allibe, S. Fusil, K. Bouzehouane, C. Daumont, D. Sando, E. Jacquet, C. Deranlot, M. Bibes and A. Barthelemy, *Nano Lett.*, 2012, **12**, 1141–1145.
212 L. W. Martin, Y.-H. Chu, M. B. Holcomb, M. Huijben, P. Yu, S.-J. Han, D. Lee, S. X. Wang and R. Ramesh, *Nano Lett.*, 2008, **8**, 2050–2055.
213 M. Huijben, P. Yu, L. W. Martin, H. J. Molegraaf, Y. H. Chu, M. B. Holcomb, N. Balke, G. Rijnders and R. Ramesh, *Adv. Mater.*, 2013, **25**, 4739–4745.
214 G. De Luca, P. Schoenherr, J. Mendil, D. Meier, M. Fiebig and M. Trassin, *Phys. Rev. Appl.*, 2018, **10**, 054030.
215 G. Wang, Z. Chen, H. He, D. Meng, H. Yang, X. Mao, Q. Pan, B. Chu, M. Zuo, Z. Sun, R. Peng, Z. Fu, X. Zhai and Y. Lu, *Chem. Mater.*, 2018, **30**, 6156–6163.
216 J. Yao, X. Song, X. Gao, G. Tian, P. Li, H. Fan, Z. Huang, W. Yang, D. Chen, Z. Fan, M. Zeng and J. M. Liu, *ACS Nano*, 2018, **12**, 6767–6776.
217 H. Saito, J. Chen and S. Ishio, *J. Magn. Magn. Mater.*, 1999, **191**, 153–161.
218 L.-Q. Chen, *J. Am. Ceram. Soc.*, 2008, **91**, 1835–1844.
219 Y. Gu, M. Li, A. N. Morozovska, Y. Wang, E. A. Eliseev, V. Gopalan and L.-Q. Chen, *Phys. Rev. B: Condens. Matter Mater. Phys.*, 2014, **89**, 174111.
220 J.-J. Wang, Y. Wang, J. F. Ihlefeld, P. E. Hopkins and L.-Q. Chen, *Acta Mater.*, 2016, **111**, 220–231.
221 J. X. Zhang, D. G. Schlom, L. Q. Chen and C. B. Eom, *Appl. Phys. Lett.*, 2009, **95**, 122904.
222 M. J. Highland, T. T. Fister, D. D. Fong, P. H. Fuoss, C. Thompson, J. A. Eastman, S. K. Streiffer and G. B. Stephenson, *Phys. Rev. Lett.*, 2011, **107**, 187602.
223 I. S. Vorotiahin, E. A. Eliseev, Q. Li, S. V. Kalinin, Y. A. Genenko and A. N. Morozovska, *Acta Mater.*, 2017, **137**, 85–92.
224 Y. Zhang, H. Lu, L. Xie, X. Yan, T. R. Paudel, J. Kim, X. Cheng, H. Wang, C. Heikes, L. Li, M. Xu, D. G. Schlom, L. Q. Chen, R. Wu, E. Y. Tsymbal, A. Gruverman and X. Pan, *Nat. Nanotechnol.*, 2018, **13**, 1132–1136.
225 L. Li, J. Britson, J. R. Jokisaari, Y. Zhang, C. Adamo, A. Melville, D. G. Schlom, L. Q. Chen and X. Pan, *Adv. Mater.*, 2016, **28**, 6574–6580.
226 S. M. Park, B. Wang, S. Das, S. C. Chae, J. S. Chung, J. G. Yoon, L. Q. Chen, S. M. Yang and T. W. Noh, *Nat. Nanotechnol.*, 2018, **13**, 366–370.
227 L. Yin, Q. Zhang, D. Li, W. Mi and X. Wang, *J. Phys. Chem. C*, 2016, **120**, 15342–15348.
228 E.-J. Guo, M. A. Roldan, X. Sang, S. Okamoto, T. Charlton, H. Ambaye, H. N. Lee and M. R. Fitzsimmons, *Phys. Rev. Mater.*, 2018, **2**, 114404.
229 C. G. Duan, S. S. Jaswal and E. Y. Tsymbal, *Phys. Rev. Lett.*, 2006, **97**, 047201.
230 L. Pan, Q. Yuan, Z. Liao, L. Qin, J. Bi, D. Gao, J. Wu, H. Wu and Z.-G. Ye, *J. Alloys Compd.*, 2018, **762**, 184–189.

231 Y. Wang, T. Harumoto, J. Wang, E. Suzuki, K. Nakada, Y. Nakamura, S. Nakagawa and J. Shi, *J. Magn. Magn. Mater.*, 2018, **453**, 206–210.
232 M. Gao, R. Viswan, X. Tang, C. M. Leung, J. Li and D. Viehland, *Sci. Rep.*, 2018, **8**, 323.
233 J. Jeong, Y. Ferrante, S. V. Faleev, M. G. Samant, C. Felser and S. S. Parkin, *Nat. Commun.*, 2016, **7**, 10276.
234 P. F. Liu, J. Miao, Z. D. Xu, G. Jakob, Q. Liu, Z. Y. Ren, K. K. Meng, Y. Wu, J. K. Chen, X. G. Xu and Y. Jiang, *Appl. Phys. Lett.*, 2018, **113**, 062401.
235 A. Hallal, H. X. Yang, B. Dieny and M. Chshiev, *Phys. Rev. B: Condens. Matter Mater. Phys.*, 2013, **88**, 184423.
236 D. Li, C. Barreteau, M. R. Castell, F. Silly and A. Smogunov, *Phys. Rev. B: Condens. Matter Mater. Phys.*, 2014, **90**, 205409.
237 H. X. Yang, M. Chshiev, B. Dieny, J. H. Lee, A. Manchon and K. H. Shin, *Phys. Rev. B: Condens. Matter Mater. Phys.*, 2011, **84**, 054401.
238 C. G. Duan, J. P. Velev, R. F. Sabirianov, Z. Zhu, J. Chu, S. S. Jaswal and E. Y. Tsymbal, *Phys. Rev. Lett.*, 2008, **101**, 137201.
239 W. Mi, Z. Guo, X. Feng and H. Bai, *Acta Mater.*, 2013, **61**, 6387–6395.
240 P. V. Ong, N. Kioussis, P. K. Amiri, J. G. Alzate, K. L. Wang, G. P. Carman, J. Hu and R. Wu, *Phys. Rev. B: Condens. Matter Mater. Phys.*, 2014, **89**, 094422.
241 D.-S. Wang, R. Wu and A. J. Freeman, *Phys. Rev. B: Condens. Matter Mater. Phys.*, 1993, **47**, 14932–14947.
242 J. Zhang, P. V. Lukashev, S. S. Jaswal and E. Y. Tsymbal, *Phys. Rev. B*, 2017, **96**, 014435.
243 C. R. Winkler, M. L. Jablonski, K. Ashraf, A. R. Damodaran, K. Jambunathan, J. L. Hart, J. G. Wen, D. J. Miller, L. W. Martin, S. Salahuddin and M. L. Taheri, *Nano Lett.*, 2014, **14**, 3617–3622.
244 C. T. Nelson, B. Winchester, Y. Zhang, S. J. Kim, A. Melville, C. Adamo, C. M. Folkman, S. H. Baek, C. B. Eom, D. G. Schlom, L. Q. Chen and X. Pan, *Nano Lett.*, 2011, **11**, 828–834.
245 D. Chen, Z. Chen, Q. He, J. D. Clarkson, C. R. Serrao, A. K. Yadav, M. E. Nowakowski, Z. Fan, L. You, X. Gao, D. Zeng, L. Chen, A. Y. Borisevich, S. Salahuddin, J. M. Liu and J. Bokor, *Nano Lett.*, 2017, **17**, 486–493.
246 Z. Chen, J. Liu, Y. Qi, D. Chen, S. L. Hsu, A. R. Damodaran, X. He, A. T. N'Diaye, A. Rockett and L. W. Martin, *Nano Lett.*, 2015, **15**, 6506–6513.
247 Y. Yun, N. Ramakrishnegowda, D.-S. Park and A. Bhatnagar, *Appl. Phys. Lett.*, 2018, **113**, 042901.
248 C. J. Roh, J. H. Lee, K.-E. Kim, C.-H. Yang and J. S. Lee, *Appl. Phys. Lett.*, 2018, **113**, 052904.
249 X. Zou, L. You, W. Chen, H. Ding, D. Wu, T. Wu, L. Chen and J. Wang, *ACS Nano*, 2012, **6**, 8997–9004.
250 Y. H. Chu, Q. Zhan, L. W. Martin, M. P. Cruz, P. L. Yang, G. W. Pabst, F. Zavaliche, S. Y. Yang, J. X. Zhang, L. Q. Chen, D. G. Schlom, I. N. Lin, T. B. Wu and R. Ramesh, *Adv. Mater.*, 2006, **18**, 2307–2311.
251 H. W. Jang, D. Ortiz, S.-H. Baek, C. M. Folkman, R. R. Das, P. Shafer, Y. Chen, C. T. Nelson, X. Pan, R. Ramesh and C.-B. Eom, *Adv. Mater.*, 2009, **21**, 817–823.
252 A. Alsubaie, P. Sharma, J. H. Lee, J. Y. Kim, C. H. Yang and J. Seidel, *ACS Appl. Mater. Interfaces*, 2018, **10**, 11768–11775.
253 L. You, Z. Chen, X. Zou, H. Ding, W. Chen, L. Chen, G. Yuan and J. Wang, *ACS Nano*, 2012, **6**, 5388–5394.
254 Z. Chen, Z. Chen, C. Y. Kuo, Y. Tang, L. R. Dedon, Q. Li, L. Zhang, C. Klewe, Y. L. Huang, B. Prasad, A. Farhan, M. Yang, J. D. Clarkson, S. Das, S. Manipatruni, A. Tanaka, P. Shafer, E. Arenholz, A. Scholl, Y. H. Chu, Z. Q. Qiu, Z. Hu, L. H. Tjeng, R. Ramesh, L. W. Wang and L. W. Martin, *Nat. Commun.*, 2018, **9**, 3764.
255 S. Bordacs, D. G. Farkas, J. S. White, R. Cubitt, L. DeBeer-Schmitt, T. Ito and I. Kezsmarki, *Phys. Rev. Lett.*, 2018, **120**, 147203.
256 R. S. Fishman, *Phys. Rev. B*, 2018, **97**, 014405.
257 B. Narayan, J. S. Malhotra, R. Pandey, K. Yaddanapudi, P. Nukala, B. Dkhil, A. Senyshyn and R. Ranjan, *Nat. Mater.*, 2018, **17**, 427–431.
258 C. Ju, J. C. Yang, C. Luo, P. Shafer, H. J. Liu, Y. L. Huang, H. H. Kuo, F. Xue, C. W. Luo, Q. He, P. Yu, E. Arenholz, L. Q. Chen, J. Zhu, X. Lu and Y. H. Chu, *Adv. Mater.*, 2016, **28**, 876–883.
259 G. Catalan, A. Lubk, A. H. Vlooswijk, E. Snoeck, C. Magen, A. Janssens, G. Rispens, G. Rijnders, D. H. Blank and B. Noheda, *Nat. Mater.*, 2011, **10**, 963–967.
260 H. Lu, C.-W. Bark, D. Esque de los Ojos, J. Alcala, C. B. Eom, G. Catalan and A. Gruverman, *Science*, 2012, **336**, 59–61.
261 Y. L. Tang, Y. L. Zhu, Y. Liu, Y. J. Wang and X. L. Ma, *Nat. Commun.*, 2017, **8**, 15994.
262 S. Ju, T. Cai, G. Guo and Z. Li, *J. Appl. Phys.*, 2008, **104**, 053904.
263 X. Shen, K. Yin, Y. S. Puzyrev, Y. Liu, L. Sun, R.-W. Li and S. T. Pantelides, *Adv. Electron. Mater.*, 2015, **1**, 1500019.
264 N. Du, N. Manjunath, Y. Li, S. Menzel, E. Linn, R. Waser, T. You, D. Bürger, I. Skorupa, D. Walczyk, C. Walczyk, O. G. Schmidt and H. Schmidt, *Phys. Rev. Appl.*, 2018, **10**, 054025.
265 J. Ho Sung, W.-M. Lee, J. Hong Lee, K. Chu, D. Lee, X. Moya, N. D. Mathur, C.-H. Yang, J.-H. Park and M.-H. Jo, *NPG Asia Mater.*, 2013, **5**, e38.
266 D. Liang, X. Li, J. Wang, L. Wu and P. Chen, *Solid-State Electron.*, 2018, **145**, 46–48.
267 L. Wei, B. Sun, W. Zhao, H. Li and P. Chen, *Appl. Surf. Sci.*, 2017, **393**, 325–329.
268 D. Li, D. Zheng, C. Jin, P. Li, X. Liu, W. Zheng and H. Bai, *Adv. Electron. Mater.*, 2018, **4**, 1800171.
269 B. Xu, G. Wang, Y. Zhou, Q. Li and Q. Xu, *Appl. Phys. Lett.*, 2018, **113**, 133901.
270 A. Rana, H. Lu, K. Bogle, Q. Zhang, R. Vasudevan, V. Thakare, A. Gruverman, S. Ogale and N. Valanoor, *Adv. Funct. Mater.*, 2014, **24**, 3962–3969.

271 Y. Cao, Q. Li, M. Huijben, R. K. Vasudevan, S. V. Kalinin and P. Maksymovych, *Phys. Rev. Mater.*, 2018, **2**, 094401.
272 S. Körbel, J. Hlinka and S. Sanvito, *Phys. Rev. B*, 2018, **98**, 100104(R).
273 J. Guyonnet, I. Gaponenko, S. Gariglio and P. Paruch, *Adv. Mater.*, 2011, **23**, 5377–5382.
274 J. Seidel, L. W. Martin, Q. He, Q. Zhan, Y. H. Chu, A. Rother, M. E. Hawkridge, P. Maksymovych, P. Yu, M. Gajek, N. Balke, S. V. Kalinin, S. Gemming, F. Wang, G. Catalan, J. F. Scott, N. A. Spaldin, J. Orenstein and R. Ramesh, *Nat. Mater.*, 2009, **8**, 229–234.
275 S. Farokhipoor and B. Noheda, *Phys. Rev. Lett.*, 2011, **107**, 127601.
276 J. Seidel, P. Maksymovych, Y. Batra, A. Katan, S. Y. Yang, Q. He, A. P. Baddorf, S. V. Kalinin, C. H. Yang, J. C. Yang, Y. H. Chu, E. K. Salje, H. Wormeester, M. Salmeron and R. Ramesh, *Phys. Rev. Lett.*, 2010, **105**, 197603.
277 J. Ma, J. Ma, Q. Zhang, R. Peng, J. Wang, C. Liu, M. Wang, N. Li, M. Chen, X. Cheng, P. Gao, L. Gu, L. Q. Chen, P. Yu, J. Zhang and C. W. Nan, *Nat. Nanotechnol.*, 2018, **13**, 947–952.
278 C. Beekman, W. Siemons, T. Z. Ward, M. Chi, J. Howe, M. D. Biegalski, N. Balke, P. Maksymovych, A. K. Farrar, J. B. Romero, P. Gao, X. Q. Pan, D. A. Tenne and H. M. Christen, *Adv. Mater.*, 2013, **25**, 5561–5567.
279 Y. C. Chen, Q. He, F. N. Chu, Y. C. Huang, J. W. Chen, W. I. Liang, R. K. Vasudevan, V. Nagarajan, E. Arenholz, S. V. Kalinin and Y. H. Chu, *Adv. Mater.*, 2012, **24**, 3070–3075.
280 C. M. Fernández-Posada, A. Castro, J.-M. Kiat, F. Porcher, O. Peña, R. Jiménez, M. Algueró and H. Amorín, *Adv. Funct. Mater.*, 2018, **28**, 1802338.
281 D. S. Rana, I. Kawayama, K. Mavani, K. Takahashi, H. Murakami and M. Tonouchi, *Adv. Mater.*, 2009, **21**, 2881–2885.
282 Z. Hu, Q. Li, M. Li, Q. Wang, Y. Zhu, X. Liu, X. Zhao, Y. Liu and S. Dong, *Appl. Phys. Lett.*, 2013, **102**, 102901.
283 T. You, Y. Shuai, W. Luo, N. Du, D. Bürger, I. Skorupa, R. Hübner, S. Henker, C. Mayr, R. Schüffny, T. Mikolajick, O. G. Schmidt and H. Schmidt, *Adv. Funct. Mater.*, 2014, **24**, 3357–3365.
284 S. Boyn, J. Grollier, G. Lecerf, B. Xu, N. Locatelli, S. Fusil, S. Girod, C. Carretero, K. Garcia, S. Xavier, J. Tomas, L. Bellaiche, M. Bibes, A. Barthelemy, S. Saighi and V. Garcia, *Nat. Commun.*, 2017, **8**, 14736.
285 J. Velev, C. Duan, J. Burton, A. Smogunov, M. Niranjan, E. Tosatti, S. S. Jaswal and E. Y. Tsymbal, *Nano Lett.*, 2009, **9**, 427–432.
286 V. Garcia, M. Bibes, L. Bocher, S. Valencia, F. Kronast, A. Crassous, X. Moya, S. Enouz-Vedrenne, A. Gloter, D. Imhoff, C. Deranlot, N. D. Mathur, S. Fusil, K. Bouzehouane and A. Barthelemy, *Science*, 2010, **327**, 1106–1110.
287 D. Pantel, S. Goetze, D. Hesse and M. Alexe, *Nat. Mater.*, 2012, **11**, 289–293.
288 M. Julliere, *Phys. Lett.*, 1975, **54**, 225–226.
289 V. Garcia, S. Fusil, K. Bouzehouane, S. Enouz-Vedrenne, N. D. Mathur, A. Barthelemy and M. Bibes, *Nature*, 2009, **460**, 81–84.
290 A. Sokolov, O. Bak, H. Lu, S. Li, E. Y. Tsymbal and A. Gruverman, *Nanotechnology*, 2015, **26**, 305202.
291 L. Yin, X. Wang and W. Mi, *ACS Appl. Mater. Interfaces*, 2018, **11**, 1057–1064.
292 J. Sołtys, M. Ptasinska, J. Piechota and S. Krukowski, *J. Cryst. Growth*, 2014, **401**, 30–32.
293 P. Aguado-Puente, N. C. Bristowe, B. Yin, R. Shirasawa, P. Ghosez, P. B. Littlewood and E. Artacho, *Phys. Rev. B: Condens. Matter Mater. Phys.*, 2015, **92**, 035438.
294 F. Cossu, J. Jilili and U. Schwingenschlögl, *Adv. Mater. Interfaces*, 2014, **1**, 1400057.
295 X. Xiang, L. Qiao, H. Y. Xiao, F. Gao, X. T. Zu, S. Li and W. L. Zhou, *Sci. Rep.*, 2014, **4**, 5477.
296 A. Ohtomo and H. Y. Hwang, *Nature*, 2004, **427**, 423–426.
297 M. S. J. Marshall, A. Malashevich, A. S. Disa, M.-G. Han, H. Chen, Y. Zhu, S. Ismail-Beigi, F. J. Walker and C. H. Ahn, *Phys. Rev. Appl.*, 2014, **2**, 051001.
298 K. D. Fredrickson and A. A. Demkov, *Phys. Rev. B: Condens. Matter Mater. Phys.*, 2015, **91**, 115126.
299 J. E. Kleibeuker, Z. Zhong, H. Nishikawa, J. Gabel, A. Muller, F. Pfaff, M. Sing, K. Held, R. Claessen, G. Koster and G. Rijnders, *Phys. Rev. Lett.*, 2014, **113**, 237402.
300 A. S. Disa, D. P. Kumah, A. Malashevich, H. Chen, D. A. Arena, E. D. Specht, S. Ismail-Beigi, F. J. Walker and C. H. Ahn, *Phys. Rev. Lett.*, 2015, **114**, 026801.
301 J. H. You and J. H. Lee, *Phys. Rev. B: Condens. Matter Mater. Phys.*, 2013, **88**, 155111.
302 Y. Wang, X. Liu, J. D. Burton, S. S. Jaswal and E. Y. Tsymbal, *Phys. Rev. Lett.*, 2012, **109**, 247601.
303 D. Xiao, W. Yao and Q. Niu, *Phys. Rev. Lett.*, 2007, **99**, 236809.
304 K. Hao, J. F. Specht, P. Nagler, L. Xu, K. Tran, A. Singh, C. K. Dass, C. Schuller, T. Korn, M. Richter, A. Knorr, X. Li and G. Moody, *Nat. Commun.*, 2017, **8**, 15552.
305 D. Xiao, G. B. Liu, W. Feng, X. Xu and W. Yao, *Phys. Rev. Lett.*, 2012, **108**, 196802.
306 K. F. Mak, K. L. McGill, J. Park and P. L. McEuen, *Science*, 2014, **344**, 1489–1492.
307 W. Feng, Y. Yao, W. Zhu, J. Zhou, W. Yao and D. Xiao, *Phys. Rev. B: Condens. Matter Mater. Phys.*, 2012, **86**, 165108.
308 W. T. Hsu, Y. L. Chen, C. H. Chen, P. S. Liu, T. H. Hou, L. J. Li and W. H. Chang, *Nat. Commun.*, 2015, **6**, 8963.
309 W. Yao, D. Xiao and Q. Niu, *Phys. Rev. B: Condens. Matter Mater. Phys.*, 2008, **77**, 235406.
310 Z. Gong, G. B. Liu, H. Yu, D. Xiao, X. Cui, X. Xu and W. Yao, *Nat. Commun.*, 2013, **4**, 2053.
311 T. Cao, G. Wang, W. Han, H. Ye, C. Zhu, J. Shi, Q. Niu, P. Tan, E. Wang, B. Liu and J. Feng, *Nat. Commun.*, 2012, **3**, 887.
312 M. Eginligil, B. Cao, Z. Wang, X. Shen, C. Cong, J. Shang, C. Soci and T. Yu, *Nat. Commun.*, 2015, **6**, 7636.
313 J. Zhou, Q. Sun and P. Jena, *Phys. Rev. Lett.*, 2017, **119**, 046403.

314 J. W. Chen, S. T. Lo, S. C. Ho, S. S. Wong, T. H. Vu, X. Q. Zhang, Y. D. Liu, Y. Y. Chiou, Y. X. Chen, J. C. Yang, Y. C. Chen, Y. H. Chu, Y. H. Lee, C. J. Chung, T. M. Chen, C. H. Chen and C. L. Wu, *Nat. Commun.*, 2018, **9**, 3143.
315 A. Rycerz, J. Tworzydlo and C. Beenakker, *Nat. Phys.*, 2007, **3**, 172–175.
316 H. Lu, W. Shan, W. Yao, Q. Niu and S. Shen, *Phys. Rev. B: Condens. Matter Mater. Phys.*, 2010, **81**, 115407.
317 D. Doennig, W. E. Pickett and R. Pentcheva, *Phys. Rev. B: Condens. Matter Mater. Phys.*, 2014, **89**, 121110(R).
318 S. Okamoto, W. Zhu, Y. Nomura, R. Arita, D. Xiao and N. Nagaosa, *Phys. Rev. B: Condens. Matter Mater. Phys.*, 2014, **89**, 195121.
319 D. Doennig, S. Baidya, W. E. Pickett and R. Pentcheva, *Phys. Rev. B*, 2016, **93**, 165145.
320 D. Doennig, W. E. Pickett and R. Pentcheva, *Phys. Rev. Lett.*, 2013, **111**, 126804.
321 Y. Weng, X. Huang, Y. Yao and S. Dong, *Phys. Rev. B: Condens. Matter Mater. Phys.*, 2015, **92**, 195114.
322 H. Tahini, F. Cossu, N. Singh, S. Smith and U. Schwingenschlögl, *Phys. Rev. B*, 2016, **93**, 035117.
323 S. Picozzi, *Front. Phys.*, 2014, **2**, 10.
324 K. Yamauchi, P. Barone and S. Picozzi, *Phys. Rev. B*, 2017, **95**, 035146.
325 W. Y. Tong, S. J. Gong, X. Wan and C. G. Duan, *Nat. Commun.*, 2016, **7**, 13612.
326 Y. Weng, L. Lin, E. Dagotto and S. Dong, *Phys. Rev. Lett.*, 2016, **117**, 037601.
327 S. G. Choi, H. T. Yi, S. W. Cheong, J. N. Hilfiker, R. France and A. G. Norman, *Phys. Rev. B: Condens. Matter Mater. Phys.*, 2011, **83**, 100101(R).
328 K. Yamauchi, P. Barone, T. Shishidou, T. Oguchi and S. Picozzi, *Phys. Rev. Lett.*, 2015, **115**, 037602.
329 J. Weber and M. Alonso, *Phys. Rev. B: Condens. Matter Mater. Phys.*, 1989, **40**, 5683–5693.
330 S. Fabiano, X. Crispin and M. Berggren, *ACS Appl. Mater. Interfaces*, 2014, **6**, 438–442.
331 Q. Lin, D. Wang, Z. Chen, W. Liu, S. Lim and S. Li, *ACS Appl. Mater. Interfaces*, 2015, **7**, 26301–26306.
332 J. Qi, X. Li, Q. Niu and J. Feng, *Phys. Rev. B: Condens. Matter Mater. Phys.*, 2015, **92**, 121403(R).
333 Q. Zhang, S. A. Yang, W. Mi, Y. Cheng and U. Schwingenschlogl, *Adv. Mater.*, 2016, **28**, 959–966.
334 H. Wang, Z. R. Liu, H. Y. Yoong, T. R. Paudel, J. X. Xiao, R. Guo, W. N. Lin, P. Yang, J. Wang, G. M. Chow, T. Venkatesan, E. Y. Tsymbal, H. Tian and J. S. Chen, *Nat. Commun.*, 2018, **9**, 3319.
335 J. Qi, N. Ma, X. Ma, R. Adelung and Y. Yang, *ACS Appl. Mater. Interfaces*, 2018, **10**, 13712–13719.
336 R. Guo, L. You, Y. Zhou, Z. S. Lim, X. Zou, L. Chen, R. Ramesh and J. Wang, *Nat. Commun.*, 2013, **4**, 1990.
337 J. T. Liang, J. M. Song, X. H. Dai, Y. S. Zhang, X. F. Liu, X. B. Li, J. Zhang, X. D. Meng, L. Zhao and B. T. Liu, *Mater. Lett.*, 2018, **229**, 312–315.
338 A. Q. Jiang, C. Wang, K. J. Jin, X. B. Liu, J. F. Scott, C. S. Hwang, T. A. Tang, H. B. Lu and G. Z. Yang, *Adv. Mater.*, 2011, **23**, 1277–1281.
339 T. You, L. P. Selvaraj, H. Zeng, W. Luo, N. Du, D. Bürger, I. Skorupa, S. Prucnal, A. Lawerenz, T. Mikolajick, O. G. Schmidt and H. Schmidt, *Adv. Electron. Mater.*, 2016, **2**, 1500352.
340 L. Bégon-Lours, V. Rouco, Q. Qiao, A. Sander, M. A. Roldán, R. Bernard, J. Trastoy, A. Crassous, E. Jacquet, K. Bouzehouane, M. Bibes, J. Santamaría, A. Barthélémy, M. Varela and J. E. Villegas, *Phys. Rev. Mater.*, 2018, **2**, 084405.
341 Y. Ishii, R. Sasaki, Y. Nii, T. Ito and Y. Onose, *Phys. Rev. Appl.*, 2018, **9**, 034034.
342 N. Balke, S. Jesse, Y.-H. Chu and S. V. Kalinin, *ACS Nano*, 2012, **6**, 5559–5565.
343 N. Balke, A. Tselev, T. M. Arruda, S. Jesse, Y.-H. Chu and S. V. Kalinin, *ACS Nano*, 2012, **6**, 10139–10146.
344 F. Gao, X. Y. Chen, K. B. Yin, S. Dong, Z. F. Ren, F. Yuan, T. Yu, Z. G. Zou and J. M. Liu, *Adv. Mater.*, 2007, **19**, 2889–2892.
345 Y. Zhang, A. M. Schultz, P. A. Salvador and G. S. Rohrer, *J. Mater. Chem.*, 2011, **21**, 4168–4174.
346 Y. C. Yang, Y. Liu, J. H. Wei, C. X. Pan, R. Xiong and J. Shi, *RSC Adv.*, 2014, **4**, 31941–31947.
347 X. Z. Deng, C. Song, Y. L. Tong, G. Yuan, F. Gao, D. Q. Liu and S. T. Zhang, *Phys. Chem. Chem. Phys.*, 2018, **20**, 3648–3657.
348 B. Safizade, S. M. Masoudpanah, M. Hasheminiasari and A. Ghasemi, *RSC Adv.*, 2018, **8**, 6988–6995.
349 Z. Li, Y. Shen, Y. Guan, Y. Hu, Y. Lin and C.-W. Nan, *J. Mater. Chem. A*, 2014, **2**, 1967–1973.
350 Y. Tian, L. Wei, Q. Zhang, H. Huang, Y. Zhang, H. Zhou, F. Ma, L. Gu, S. Meng, L. Q. Chen, C. W. Nan and J. Zhang, *Nat. Commun.*, 2018, **9**, 3809.
351 K.-E. Kim, S. Jeong, K. Chu, J. H. Lee, G.-Y. Kim, F. Xue, T. Y. Koo, L.-Q. Chen, S.-Y. Choi, R. Ramesh and C.-H. Yang, *Nat. Commun.*, 2018, **9**, 403.
352 J. Belhadi, S. Yousfi, H. Bouyanfif and M. El Marssi, *J. Appl. Phys.*, 2018, **123**, 154103.
353 D. Hirai, J. Matsuno and H. Takagi, *APL Mater.*, 2015, **3**, 041508.
354 M. Gibert, P. Zubko, R. Scherwitzl, J. Iniguez and J. M. Triscone, *Nat. Mater.*, 2012, **11**, 195–198.